Università degli Studi di Pisa

PhD school Galileo Galilei

The Mu2e crystal calorimeter and improvements in the $\mu^-\mathrm{N} \rightarrow e^-\mathrm{N}$ search sensitivity

PhD thesis

Supervisors
Prof. Franco Cervelli,
University and INFN of Pisa
Dr. Pavel Murat,
Fermilab

Candidate
Gianantonio Pezzullo
University of Pisa

Academic period 2012/2015

“Nulla dies sine linea”
(Plinio il Vecchio, Naturalis historia)

Contents

1 LFV and Standard Model **6**
- 1.1 Theoretical introduction . . . 6
- 1.2 Search for CLFV . . . 9
- 1.3 CLFV in μ decays . . . 10
  - 1.3.1 Experimental search for $\mu^+ \to e^+\gamma$ process . . . 10
  - 1.3.2 Experimental search for $\mu^\pm \to e^\pm e^- e^+$ . . . 11
- 1.4 Experimental searches for $\mu^-\mathrm{N} \to e^-\mathrm{N}$ . . . 11
  - 1.4.1 Background sources . . . 12
  - 1.4.2 $\mu^-\mathrm{N} \to e^-\mathrm{N}$ experimental limits . . . 13

2 The Mu2e experiment **15**
- 2.1 Mu2e overview . . . 15
- 2.2 Muons for Mu2e . . . 17
  - 2.2.1 Requirements . . . 17
  - 2.2.2 Proton beam . . . 17
  - 2.2.3 Muon beamline . . . 19
  - 2.2.4 Mu2e coordinates system . . . 23
- 2.3 Mu2e stopping target . . . 23
  - 2.3.1 Muon stopping targets . . . 23
- 2.4 Mu2e detector . . . 26
  - 2.4.1 Tracker . . . 27
  - 2.4.2 Calorimeter . . . 29
  - 2.4.3 Cosmic Ray Veto . . . 30

3 The calorimeter **32**
- 3.1 Requirements . . . 32
- 3.2 Design . . . 33

3.3 Crystal choice . . . 33
3.4 Photosensor choice . . . 37
3.5 Radiation hardness . . . 38
3.5.1 Dose . . . 38
3.5.2 Neutron flux . . . 39
3.6 Calibration system . . . 42
3.7 Simulation of the calorimeter performance . . . 45
3.7.1 Cluster reconstruction . . . 45
3.7.2 Energy resolution . . . 45
3.7.3 Coordinate resolution . . . 46
3.7.4 Time resolution . . . 47
3.7.5 Calorimeter trigger . . . 47

4 Calorimeter prototype test **50**
4.1 Experimental setup . . . 50
4.2 Charge and time reconstruction . . . 54
4.3 Analysis selection . . . 63
4.4 Calibration . . . 65
4.5 Measurement of the time resolution . . . 70
4.5.1 Beam incidence at 0 deg . . . 70
4.5.2 Beam incidence at 50 deg . . . 74
4.5.3 Cosmic rays . . . 81
4.5.4 Time resolution without using time walk corrections . . . 85
4.6 Measurement of the energy resolution . . . 87
4.6.1 Beam incidence at 0 deg . . . 87
4.6.2 Beam incidence at 50 deg . . . 89

5 Calorimeter driven pattern recognition **91**
5.1 Algorithm description . . . 92
5.1.1 Straw hits pre-selection . . . 93
5.1.2 Helix search . . . 96
5.2 Pattern recognition efficiency . . . 101

6 Improvements in the track reconstruction **106**
6.1 Improvement in the momentum resolution . . . 108
6.2 Efficiency improvement using the calorimeter . . . 113

7 Particle identification and expected sensitivity **116**

7.1 Calorimeter-based particle identification 116
7.1.1 Cosmic muons rejection 117
7.1.2 $\bar{p}$ induced background rejection 122
7.2 Mu2e sensitivity estimation 126
7.2.1 Input for the sensitivity calculation 126
7.2.2 Results for 90% CL upper limit 128

8 Conclusions **130**

Introduction

The Mu2e experiment will search for Charged Lepton Flavor Violation (CLFV) looking at the conversion of a muon into an electron in the field of an aluminum nucleus. About $7 \cdot 10^{17}$ muons, provided by a dedicated muon beam line in construction at the Fermi National Accelarator Laboratory (Fermilab), will be stopped in 3 years in the Aluminum target. The corresponding single event sensitivity will be $2.5 \cdot 10^{-17}$[1].

The Standard Model of particle physics, even extendend to include the finite neutrino masses, predicts the ratio $R_{\mu e}$ between muon conversions and muon nuclear captures to be $\sim 10^{-52}$ [2]. Several extensions of the Standard Model predict $R_{\mu e}$ to be in the range of $10^{-14} - 10^{-18}$ [3]. The current best experimental limit, set by the SINDRUM II experiment is $7 \cdot 10^{-13}$ @ 90% CL [4]. The Mu2e experiment plans to improve this experimental limit by four order of magnitude to test many of the possible extensions of the Standard Model. To reach this ambitious goal, the Mu2e experiment is expected to use an intense pulsed muon beam, and rely on a detector system composed of a straw tube tracker and a calorimeter made of pure CsI crystals.

The calorimeter plays a central role in the Mu2e measurement, providing particle identification capabilities that are necessary for rejecting two of the most dangerous background sources that can mimic the $\mu^- N \rightarrow e^- N$ conversion electron: cosmic muons and $\bar{p}$ induced background.

The calorimeter information allows also to improve the tracking performance. Thanks to a calorimeter-seeded track finder algorithm, it is possible to increase the track reconstruction efficiency, and make it more robust with respect to the occupancy level.

Expected performances of the calorimeter have been studied in a beam test at the Beam Test Facility in Frascati (Rome, Italy). A reduced scale calorimeter prototype has been exposed to an electron beam, with energy varying from 80 to 140 MeV, for measuring the timing resolution and validate the Monte Carlo prediction. A timing resolution $\sigma_t < 200$ ps @ 100 MeV has been obtained.

Combination of the background rejection performance, and the improvements in the track reconstruction, have then been combined in the calculation of the expected Mu2e sensitivity.

Chapter 1

LFV and Standard Model

1.1 Theoretical introduction

In the Standard Model (SM) version where only one Higgs doublet is included and massless neutrinos are assumed, lepton flavor conservation is an automatic consequence of gauge invariance and the renormalizability of the SM Lagrangian [5–7]. However measurements of the neutrino mixing parameters during the last decades [8] showed that lepton flavor is not conserved. Including finite neutrino mass terms in the SM Lagrangian CLFV is also predicted. CLFV transitions are suppressed by sums over $\left(\Delta m^2_{ij}/M^2_W\right)^2$, where Δm^2_{ij} is mass-squared difference between the neutrino mass eigenstates i, j and M_W is the W boson mass [2]. Because the neutrino mass difference is very small ($\Delta m^2_{ij} \leq 10^{-3}\text{eV}^2$ [8]) with respect to the W boson mass, the expected branching ratios reach unmeasurable values, below 10^{-50} [2, 9]. As a consequence, an observation of CLFV process would represent a clear evidence of new physics beyond the SM. In the last decades LFV processes were studied within the supersymmetric extensions of the SM (SUSY) [2, 3] and in particular within the supersymmetric grand unified theories (SUSY GUT) [10, 11]. In SUSY models there is a new source of flavor mixing in the mass matrices of SUSY partners for leptons and quarks, called sleptons and squarks respectively. Flavor mixing in the slepton mass matrix would induce LFV processes for charged leptons. In the SUSY GUT scenario, the flavor mixing in the slepton sector is naturally induced at the GUT scale because leptons and quarks belong to the same GUT multiplet [3].

Process	Upper limit	References
$\mu^+ \to e^+\gamma$	$< 5.7 \times 10^{-13}$	[12]
$\mu^\pm \to e^\pm e^- e^+$	$< 1.0 \times 10^{-12}$	[13]
$\mu^-\mathrm{Ti} \to e^-\mathrm{Ti}$	$< 1.7 \times 10^{-12}$	[14]
$\mu^-\mathrm{Au} \to e^-\mathrm{Au}$	$< 7 \times 10^{-13}$	[4]
$\mu^+ e^- \to \mu^- e^+$	$< 3.0 \times 10^{-13}$	[14]
$\tau \to e\gamma$	$< 3.3 \times 10^{-8}$	[15]
$\tau^- \to \mu\gamma$	$< 4.4 \times 10^{-8}$	[15]
$\tau^- \to e^- e^+ e^-$	$< 2.7 \times 10^{-8}$	[16]
$\tau^- \to \mu^-\mu^+\mu^-$	$< 2.1 \times 10^{-8}$	[16]
$\tau^- \to e^-\mu^+\mu^-$	$< 2.7 \times 10^{-8}$	[16]
$\tau^- \to \mu^- e^+ e^-$	$< 1.8 \times 10^{-8}$	[16]
$\tau^- \to e^+\mu^-\mu^-$	$< 1.7 \times 10^{-8}$	[16]
$\tau^- \to \mu^+ e^- e^-$	$< 1.5 \times 10^{-8}$	[16]
$\pi^0 \to \mu e$	$< 8.6 \times 10^{-9}$	[17]
$\mathrm{K}^0_\mathrm{L} \to \mu e$	$< 4.7 \times 10^{-12}$	[18]
$\mathrm{K}^+ \to \pi^+\mu^+ e^-$	$< 2.1 \times 10^{-10}$	[19]
$\mathrm{K}^0_\mathrm{L} \to \pi^0\mu^+ e^-$	$< 4.4 \times 10^{-10}$	[20]
$\mathrm{Z}^0 \to \mu e$	$< 1.7 \times 10^{-6}$	[21]
$\mathrm{Z}^0 \to \tau e$	$< 9.8 \times 10^{-6}$	[21]
$\mathrm{Z}^0 \to \tau\mu$	$< 1.2 \times 10^{-6}$	[22]

Table 1.1: Sample of various CLFV processes. Data from current experimental bounds.

In general, CLFV can be studied via a large variety of processes:

- muon decays, such as $\mu^+ \to e^+\gamma$, $\mu^\pm \to e^\pm e^- e^+$, and muon conversion;
- tau decays: $\tau^\pm \to \mu^\pm\gamma$, $\tau^\pm \to \mu^\pm\mu^+\mu^-$, ecc;
- meson decays: $\pi^0 \to \mu e$, $\mathrm{K}^0_\mathrm{L} \to \mu e$, $\mathrm{K}^+ \to \pi^+\mu^+ e^-$, ecc;
- Z^0 decays, such as $\mathrm{Z}^0 \to \mu e$, ecc.

Table 1.1 shows the current upper limits on the branching ratios of various CLFV processes. The muon processes have been intensely studied in the CLFV for several reasons:

- low energy muon beams can be produced at high-intensity proton accelera-

tor facilities.

- final state of processes in the muon sector can be precisely measured.

Search for CLFV with muons has been pursued looking for muon decays ($\mu^+ \to e^+\gamma$ and $\mu^\pm \to e^\pm e^- e^+$), and muon coherent conversion ($\mu^-\mathrm{N} \to e^-\mathrm{N}$).

A model-independent approach represents a convenient way to illustrate differences among these channels. CLFV can be introduced in the SM by adding CLF-violating terms to the SM Lagrangian [23]:

$$L_{CLFV} = \frac{m_\mu}{(\kappa+1)\Lambda^2}\bar{\mu}_R\sigma_{\mu\nu}e_L F^{\mu\nu} + \text{h.c.} + \frac{\kappa}{(\kappa+1)\Lambda^2}\bar{\mu}_L\gamma_\mu e_L\,(\bar{e}\gamma^\mu e) + \text{h.c.} \qquad (1.1)$$

where Λ is the mass scale of the new physics and κ is a dimensionless parameter. These tow terms in Equation 1.1 correspond to "dipole" and "contact" interactions terms, respectively, where m_μ is the muon mass, $F^{\mu\nu}$ is the electromagnetic field tensor, and R and L represent the chirality of the fermion fields. Figures 1.1 show

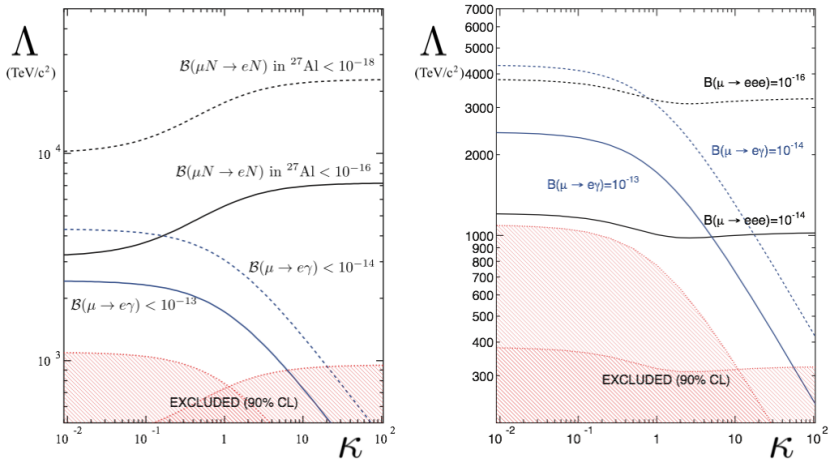

Figure 1.1: Λ versus κ sensitivity plots using: $\mu^-\mathrm{N} \to e^-\mathrm{N}$ and $\mu^+ \to e^+\gamma$ (left) and $\mu^\pm \to e^\pm e^- e^+$ and $\mu^+ \to e^+\gamma$ branching ratios. Red filled areas represent the region already excluded @ 90 CL.

the Λ versus κ sensitivity plots for the CLFV muon channels. These plots also show that:

- $\mu^-\mathrm{N} \to e^-\mathrm{N}$ search can explore the phase space region where the contact term is dominant and $\mu^+ \to e^+\gamma$ decay is further suppressed;

- The CLFV searches shown here are able to explore new physics mass scales significantly beyond the direct reach at the LHC energies.

Even if LHC discovers new physics in the second run, precise measurements of CLFV processes can help discriminate among several theoretical models [9].

1.2 Search for CLFV

The search for CLFV in the muon sector was pioneered by Hinks and Pontecorvo in 1947, with the first search of $\mu^+ \to e^+\gamma$ using cosmic-ray muons. Soon afterwards, the search for muon conversion $\mu^-\mathrm{N} \to e^-\mathrm{N}$ was also carried out by Lagarrigue and Peyrou in 1952. After 1955 a new era for the CLFV began thanks to the upcoming accelerator based experiments. Figure 1.2 shows the history of the limits on the branching ratio of muon decays and muon conversion: the figure also shows the goals of upcoming experiments [9].

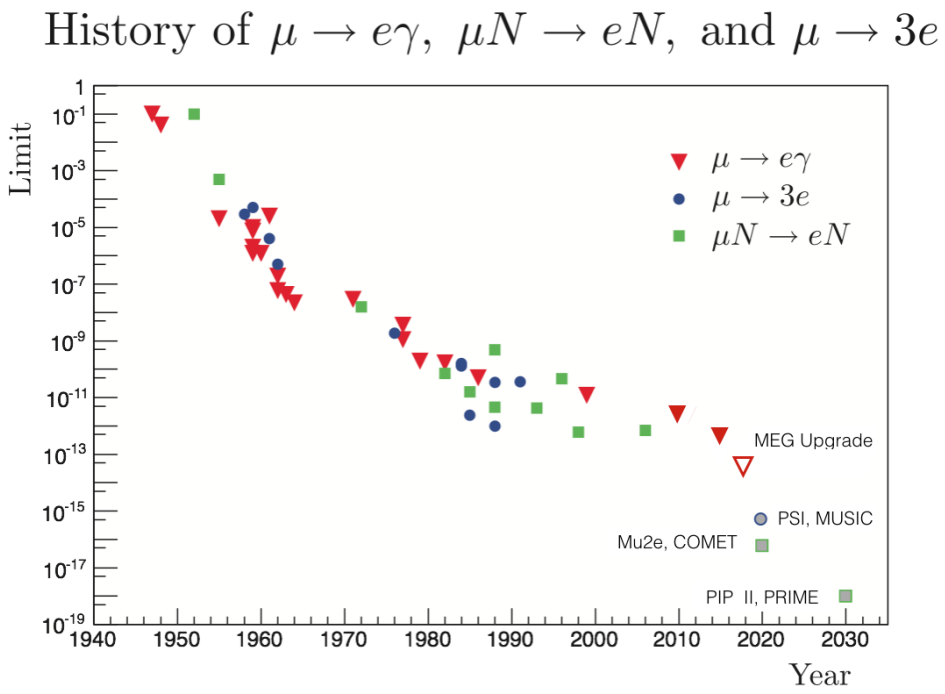

Figure 1.2: History of CLFV upper limits @ 90% CL for muon processes.

The sensitivity on the CLFV search has been increased by many order of magnitude over the years, and in the next decade new limits will emerge from several experiments under construction or upgrade.

1.3 CLFV in μ decays

Experimentally, the search of CLFV using rare muon decays presents pros and cons. One advantage comes from the fact that these processes are charge symmetric, so using either μ^+ or μ^- has no theoretical disadvantage. However the use of positive muons reduces significantly the background sources thanks to the absence of capture processes. Nuclear captures are usually noisy for the detectors because they produce charged and neutral secondaries: p, n and γ.

On the other hand, channels involving μ^+ decays ($\mu^+ \to e^+\gamma$,$\mu^\pm \to e^\pm e^- e^+$) suffer for accidental background caused by the coincidence of two separate processes that can mimic the signal. This kind of background limits the beam intensity of the experiment.

1.3.1 Experimental search for $\mu^+ \to e^+\gamma$ process

$\mu^+ \to e^+\gamma$ process is a two-body decay, so the positron and the photon are emitted back to back in the rest frame of the decaying muon. Neglecting the tiny positron mass, each product carries an energy equal to half the muon mass (52.8 MeV). Variation in the expected energy spectrum can occur in case of muon decays in flight, where a boost needs to be taken into account for re-evaluating both the energy spectra and the emission distributions. Boost related problems are avoided if low energy muons are stopped in a target. The largest background in $\mu^+ \to e^+\gamma$ search is an accidental coincidence of a positron from the standard Michel decay of muons, $\mu \to e\nu\bar{\nu}$, and a relatively high energy photon from radiative muon decay, $\mu \to e\nu\bar{\nu}\gamma$. Because the accidental background increases quadratically with the muon rate, a continuous muon beam with a low instantaneous rate is preferable for the $\mu^+ \to e^+\gamma$ search.

The current best limit on $\mu^+ \to e^+\gamma$ branching ratio is $\mathrm{B}(\mu^+ \to e^+\gamma) < 5.7 \times 10^{-13}$ @ 90% C.L. [12], obtained by the MEG experiment in 2013. An upgrade of the

detector system is underway for improving the detector performance. The goal is to improve sensitivity by another order of magnitude [24].

1.3.2 Experimental search for $\mu^{\pm} \rightarrow e^{\pm}e^{-}e^{+}$

The search for the $\mu^{\pm} \rightarrow e^{\pm}e^{-}e^{+}$ decay requires a detector system characterized by a large acceptance for low momenta electrons and positrons, and the consequent capability to tolerate the positron flux from the Michel muon decay. The main source of background is represented by accidental coincidences of positrons from the Michael decay with e^{-} e^{+} pairs either from gamma ray conversions, or from Bhabha scattering of Michael positrons with atomic electrons.

The present upper limit on $\mu^{\pm} \rightarrow e^{\pm}e^{-}e^{+}$ branching ratio is $B(\mu^{\pm} \rightarrow e^{\pm}e^{-}e^{+}) < 1 \times 10^{-12}$ @ 90% C.L. [13]. It was obtained by the SINDRUM experiment at PSI in 1988. A new experiment, named Mu3e, has been proposed at PSI for lowering the sensitivity down to the level of about 10^{-16} [25].

1.4 Experimental searches for $\mu^{-}\mathrm{N} \rightarrow e^{-}\mathrm{N}$

When negative muons are stopped in a target ("stopping target") they are quickly captured by the atoms ($\sim 10^{-10}$ s) and cascade down to 1S orbital. Then muons can undergo the following processes:

- decay in orbit (DIO) $\mu^{-} \rightarrow e^{-}\nu_{\mu}\bar{\nu}_{e}$;
- weak capture $\mu^{-}\mathrm{p} \rightarrow \nu_{\mu}\mathrm{n}$;
- coherent flavor changing conversion $\mu^{-}\mathrm{N} \rightarrow e^{-}\mathrm{N}$.

The muon conversion represents a powerful channel to search for CLFV, because it is characterized by a distinctive signal consisting in a mono-energetic electron with energy $\mathrm{E_{ce}}$:

$$\mathrm{E}_{ce} \;=\; \mathrm{m}_{\mu} - \mathrm{E}_{b} - \frac{\mathrm{E}_{\mu}^{2}}{2\mathrm{m}_{\mathrm{N}}}$$

where m_{μ} is the muon mass at rest, $\mathrm{E}_{b} \sim \mathrm{Z}^{2}\alpha^{2}\mathrm{m}_{\mu}/2$ is the muonic atom binding energy for a nucleus with atomic number Z, E_{μ} is the nuclear recoil energy, E_{μ} =

$m_\mu - \mathrm{E}_b$, and $\mathrm{m_N}$ is the atomic mass [2]. In case of Al, which is the major candidate for upcoming experiments, E_{ce} = 104.973 MeV [26].

In muon conversion experiments the quantity:

$$\mathrm{R}_{\mu e} = \frac{\Gamma(\mu^- + \mathrm{N} \rightarrow e^- + \mathrm{N})}{\Gamma(\mu^- + \mathrm{N} \rightarrow \text{all captures})}$$

is measured. The normalization to captures offers a calculation advantage since many details of the nuclear wavefunction cancel in the ratio [26].

The coherent conversion leaves the nucleus intact, and there is only one detectable particle in the final state. The resulting electron energy stands out from the background (this will be more clear in the next paragraph), hence muon-electron conversion does not suffer from accidental background, and extremely high rates can be used.

1.4.1 Background sources

μ^- stopped in the stopping target can undergo a nuclear capture [27]. Particles generated in the muon capture (n, p and γ) may reach the detector system, and create extra activity which can either obscure a conversion electron (CE) track or create spurious hits. As a result, some specific shielding is required to reduce this background. Additional shielding is required against cosmic rays, which can interact in the apparatus, producing electrons with an energy mimicking a CE.

Electrons from the high momentum tail of the muon DIO represent the largest background source for the $\mu^-\mathrm{N} \rightarrow e^-\mathrm{N}$ search. Figure 1.3 shows the energy spectrum of DIO electrons [28]. The main features of the DIO energy spectrum can be summarized as follows:

- the endpoint of the spectrum corresponds to the energy of the electrons from $\mu^-\mathrm{N} \rightarrow e^-\mathrm{N}$ conversion (CE);
- the overall spectrum is falling as $(E_{ce} - E_e)^5$, where E_{CE} is the CE energy, and E_e is the DIO energy;
- about 10^{-17} of the spectrum is within the last MeV from the endpoint.

Therefore, to reach a sensitivity at the level $O(10^{-17})$ the detector resolution is crucial.

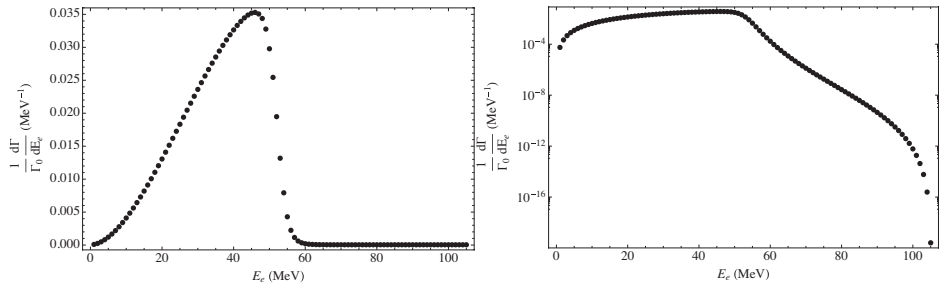

Figure 1.3: DIO electron energy spectrum on linear (left) and log (right) scale, for muons bounded in Al nuclei.

Another relevant background comes from the radiative pion capture (RPC) process $\pi^-\mathrm{N} \to \gamma\mathrm{N}^*$, followed by the electron-positron pair conversion of the γ. Another source of background are pions; muon beam is generated from low energy protons (below 10 GeV of energy) interacting with a (production) target, so producing charged pions that then decay in a transport line. Unfortunately not all pions decay in the transport line, and, consequently, the muon beam is contaminated by pion. This source of background is reduced thanks to the difference between the pion and the bound muon life times. The pion has a $\tau <$ few tens of ns, while the bound muon has a mean lifetime of the order of several hundreds of ns (depending on the Z of the material [27]). Therefore using a pulsed beam structure, it is possible to define a live-gate delayed with respect to the beam arrival, and to reduce the $\pi^-\mathrm{N} \to \gamma\mathrm{N}^*$ contribution to the desired level.

Other beam-related sources of background are: remnant electrons in the beam that scatter in the stopping target, muon decays in flight, and antiprotons annihilating in or near the stopping target.

1.4.2 $\mu^-\mathrm{N} \to e^-\mathrm{N}$ experimental limits

The current upper limits on the $\mu^-\mathrm{N} \to e^-\mathrm{N}$ have been set by the SINDRUM II experiment for Au and Ti nuclei: $\mathrm{B}(\mu^-\mathrm{N} \to e^-\mathrm{N}$ on Au$) < 7 \times 10^{-13}$ @ 90% C.L. [4] and $\mathrm{B}(\mu^-\mathrm{N} \to e^-\mathrm{N}$ on Ti$) < 1.7 \times 10^{-12}$ @ 90% C.L. [29].

Three $\mu^-\mathrm{N} \to e^-\mathrm{N}$ conversion experiments with significantly higher design sensitivity are currently under construction: DeeMe and COMET at J-PARC in Japan and Mu2e at Fermilab in the USA.

The first operating experiment will be DeeMe [30] at the Material and Life Science Experimental Facility, which is going to start data taking at the end of 2015. The expected single event sensitivity is 2×10^{-14}, which represents a factor ~ 10 of improvement on the current limit from SINDRUM II [4].

The other experiment at J-PARC will be COMET [31]. It has been designed to run in two phases with different detectors and geometries. The expected single event sensitivity in the end of the phase-I is 10^{-15} [32], a factor 100 better than the current limit. The phase-II run will start in 2020 and aims a single event sensitivity of 3×10^{-17} [32]. Mu2e is expected to start tacking data in 2020, and it has been designed to reach a similar event sensitivity of 2.5×10^{-17}.

COMET (phase-II) and Mu2e share the following concepts:

- the use of pulsed proton beam to reduce the contribution from RPC background;
- curved transport solenoid systems for the muon beam to keep the detector region free from neutral particles coming from the production target, and also to facilitate the charge selection;
- a detector solenoid housing the muon stopping target and/or the detector system.

Chapter 2

The Mu2e experiment

2.1 Mu2e overview

The Mu2e experiment at Fermilab intends to search for $\mu \rightarrow e$ conversion in the field of an Al nucleus, aiming to measure the conversion rate relative to the total muon capture rate:

$$R_{\mu e} = \frac{\Gamma\left(\mu^- + \ N(A, Z) \rightarrow e^- + \ N(A, Z)\right)}{\Gamma\left(\mu^- + \ N(A, Z) \rightarrow \text{all captures}\right)}$$

Mu2e had its genesis back in the 80s, behind the Iron Curtain. In a way, Mu2e was born in the Soviet Union. In 1989, the Soviet Journal of Nuclear Physics published a letter to the editor from physicists Vladimir Lobashev and Rashid Djilkibaev, where they proposed an experiment that would perform the most thorough search yet for muon-to-electron flavor violation. In 1992, they proposed the MELC experiment at the Moscow Meson Factory [33], but then, due to the political and economic crisis, in 1995 the experiment shut down. The same overall scheme was subsequently adopted in the Brookhaven National Laboratory MECO proposal in 1997 [34]. The Mu2e experimental apparatus includes three main superconducting solenoid systems:

- **Production solenoid (PS)**, where an 8 GeV pulsed proton beam strikes a tungsten target, producing mostly pions;

- **Transport solenoid (TS)**, allowing to select low momenta negative pions coming from the production solenoid and letting them to decay into muons before they reach the detector region;
- **Detector solenoid (DS)**, housing the Al muon stopping target and the detector system.

Downstream to the proton beam pipe, outside the PS, an extinction monitor is used to measure the number of protons in between two subsequent proton pulses. The DS is surrounded by a cosmic ray veto system, which covers the DS from three sides (the ground is not covered) and extends up to the midpoint of the TS. Outside the DS, a stopping target monitor is used to measure the total number of muon captures. Figure 2.1 shows the Mu2e experimental apparatus.

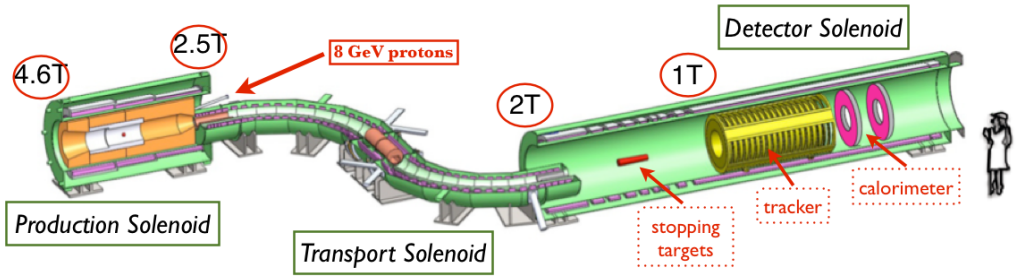

Figure 2.1: Mu2e apparatus.

To reach the projected single event sensitivity $R_{\mathrm{SES}} = 2.5 \cdot 10^{-17}$ [1] the experiment needs:

- a low energy pulsed muon beam;
- a detector system capable to reconstruct the electron from $\mu^- \mathrm{N} \rightarrow e^- \mathrm{N}$ (CE), and to reject the competing backgrounds.

2.2 Muons for Mu2e

2.2.1 Requirements

Usually low energy muon beams are generated by protons interacting with a target. A magnetic system collects muons and pions directly produced, which in turn decay into muons. In the Mu2e experiment the key features of the muon beam production are:

- intensity and time structure of the proton beam;
- muon beam transport efficiency;
- purity of the muon beam.

2.2.2 Proton beam

The Fermilab accelerator complex stages the protons spills for Mu2e as follow:

1. booster protons batches, each containing 4×10^{12} protons with a kinetic energy of 8 GeV, are extracted into the MI-8 beamline and injected into the Recycler Ring;
2. a new bunch formation is performed using a RF manipulation sequence;
3. bunches are synchronously transferred to the Delivery Ring;
4. a resonant extraction system injects $\sim 3 \times 10^7$ protons into the Mu2e beam line each 1.7 μs (revolution period in the Delivery Ring).

Figure 2.2 shows the Fermilab accelerator complex. An important parameter used to estimate the quality of the proton beam is the relative number of protons in between two subsequent pulses (out-of-time), defined as the "extinction factor". These protons are a potential source of RPC, which is not suppressed by a delayed "live gate". An high frequency AC dipole is used to suppress protons between successive batches, providing an extinction factor of about 10^{-10} [1]. An extinction monitor system, located above the production target (see Figure 2.3), is used to measure the number of scattered protons as a function of time, so to provide a direct measurement of the residual beam between the batches. Figure 2.4 shows the extinction monitor system. It is composed of:

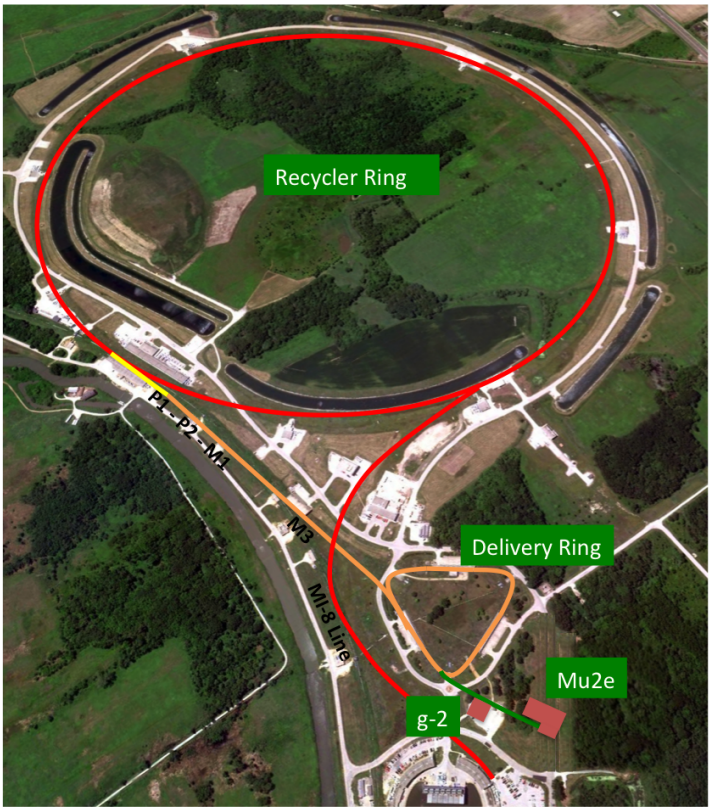

Figure 2.2: Accelerator complex providing the proton beam to Mu2e.

- a filter magnet, which selects particles with an average momentum of 4.2 GeV/c;
- two collimators, placed in front of the filter magnet;
- a spectrometer magnet, placed in between two series of Si pixel detectors to allow momentum measurement;
- scintillating counters to trigger the Si readout in case of out-of-time particles and time stamp them;
- a sampling calorimeter to identify muons.

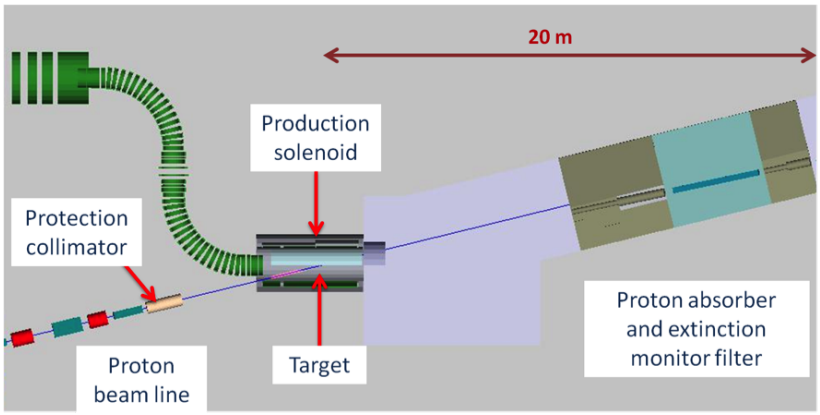

Figure 2.3: Location of the extinction monitor system (left).

2.2.3 Muon beamline

The Mu2e solenoid system has been designed to:

- capture pions from the proton-target interaction;
- create the secondary muon beam;
- transport the muon beam;
- remove positive particle and other possible source of background from the muon beam;
- provide a uniform field in the detector region.

Production solenoid

The production solenoid is a high field superconducting magnet with a graded field varying from 4.6 to 2.5 Tesla. The solenoid is approximately 4 m long and has an inner bore diameter of about 1.5 m evacuated to 10^{-5} Torr. A shield structure made of bronze is placed in between the inner bore and the PS coil to limit the radiation damage.

The 8 GeV proton beam enters in the middle of the PS (see Figure 2.5) and strikes a radiatively cooled Tungsten target, producing mostly pions. The axially graded magnetic field reflects the charged particles toward the low B-field region where

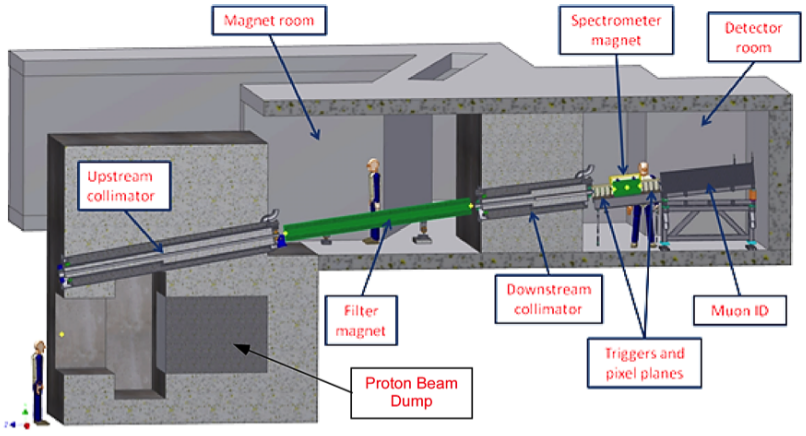

Figure 2.4: Extinction monitor apparatus.

the PS is linked to the transport solenoid (TS). The graded axial magnetic field creates a so-called "magnetic bottle"; charged particles emitted in the opposite side with respect to the TS entrance are reflected in the opposite direction. This capture scheme represents an innovative technology; according to many simulation studies, the capture efficiency is expected to be of about 1000 times larger than in conventional muon facilities [35].

Transport solenoid

The S-shaped transport solenoid consists of several straight and toroidal sections. Installed inside the TS, collimators and absorbers provide efficient selection of low energy negative muons before they reach the DS. Figure 2.6 shows the five main TS components:

- TS1 links the PS to the TS. TS1 houses a collimator that selects particles with momentum lower than 100 MeV/c;
- TS2: a quarter of toroid, avoiding neutral particle from the PS to propagate into the DS;
- TS3: a straight solenoid containing two collimators, for filtering particles based on sign and momentum, separated by a berillium window, needed for stopping antiprotons produced in the PS;

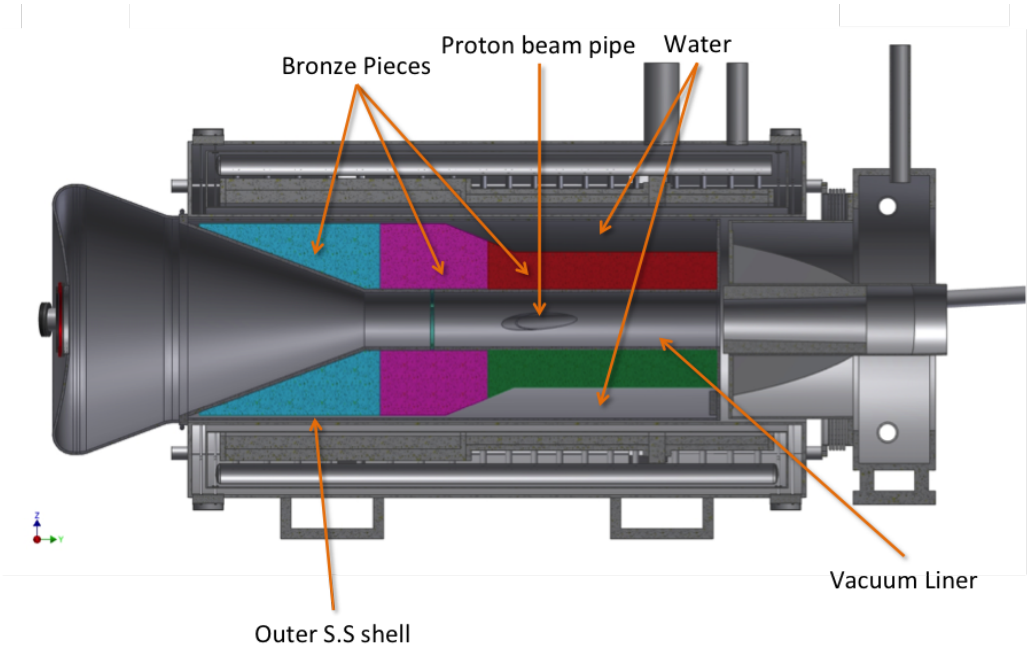

Figure 2.5: Production solenoid view.

- TS4: another quarter of toroid, similar to the TS2, which does not allow neutral particles from the beam interactions in the TS3 to reach the DS;
- TS5: interfacing the beam line with the DS. It is equipped with a collimator for momentum selection.

To minimize the transport of particles that spend a long time in the magnetic system, the B field in the straight sections has a negative gradient along their main axis. That allows to accelerate particles from the PS region thorough the DS [1].

Detector solenoid

The DS is $\sim$ 11 m long and houses the muon stopping target, the tracker, and the calorimeter. The inner bore is evacuated to 10^{-4} Torr in order to limit interactions of muons with gas atoms [1]. The DS is subdivided in two regions:

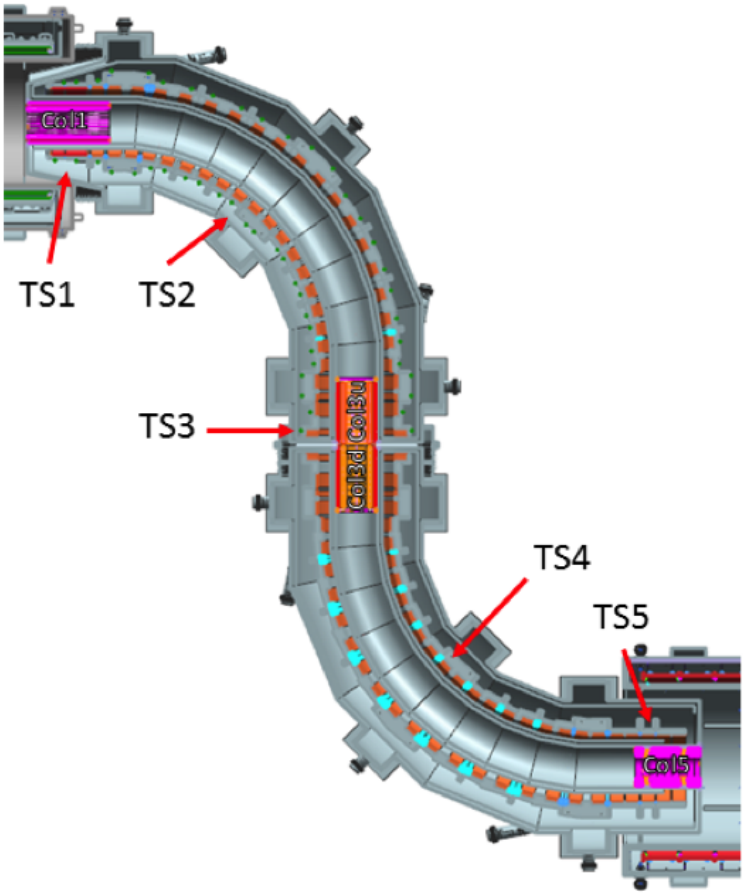

Figure 2.6: Transport solenoid view.

1. an upstream side closer to the TS housing the stopping target, with a graded magnetic field ranging from 2 to 1 Tesla;
2. a downstream part, with an uniform 1 Tesla field, housing the detector system.

Figure 2.7 shows a section view of the DS. The graded field efficiently reflects conversion electrons emitted in the opposite side of the detector system.

The muon stopping target are surrounded by the neutron absorber that reduces the neutron flux, resulting from muon capture events. Neutrons are potentially

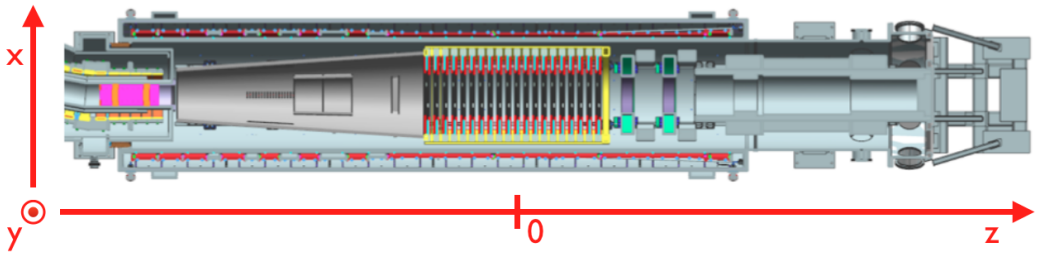

Figure 2.7: Detector solenoid view. Red lines illustrate the coordinate system: Z-axis parallel to the DS axis with the origin in the middle of the tracker, Y-axis normal to the plane where all three main solenoids lay, and .

dangerous, as they increase the cosmic ray veto hit rate, which could result in an increased detector dead time. In between the stopping target and the detector system a proton absorber is placed to reduce the amount of protons reaching the detectors. Protons are originated from muon nuclear captures and have energies up to few tens of MeV [27]; they are highly ionizing and can be a source of aging for the detectors.

2.2.4 Mu2e coordinates system

The coordinate system is right-handed, and is defined as illustrated in Figure 2.7. The Z-axis is parallel to the DS axis and is positively oriented moving from the stopping target to the detector region, with the origin in the middle of the tracker. The Y-axis is normal to the plane where all the three solenoids lay, and is positively oriented in the opposite direction of the ground. Then the X-axis is defined by the vector product of the other two axis: $\vec{x} = \vec{y} \times \vec{z}$.

2.3 Mu2e stopping target

2.3.1 Muon stopping targets

Mu2e requires a significant number of negatively charged muons to be stopped in a target. This must be massive enough to stop significant fraction of the muon

beam, but not so massive to minimize the loss energy of the conversion electrons crossing part of it.

Aluminum is the selected material for the stopping target because the mean lifetime of a muon in an Al nucleus is 864 ns, which is of about one half the proton bunch spacing. This allows to define a selection window sufficiently far (hundreds of ns) from the beam arrival time, for rejecting part of the RPC induced background, while retaining a signal acceptance of about 70%.

The final design of the stopping target has been chosen to optimize the sensitivity of the experiment [1]: it consists of 17 Al foils of 200 μm thickness, with radii

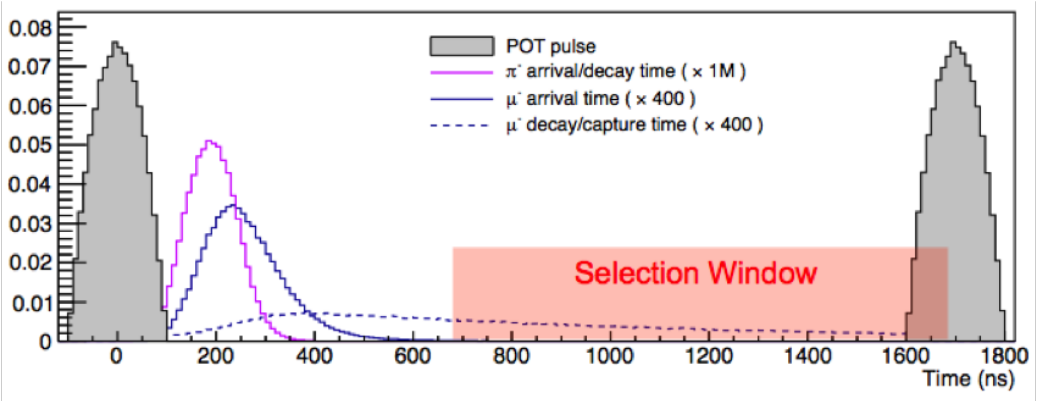

Figure 2.8: The Mu2e spill cycle for the proton on target pulse (POT) and the delayed selection window that allows an effective elimination of the background from RPC.

ranging from 83 to 65 mm. Figure 2.9 shows a picture of the stopping target with its support structure. Figure 2.10 shows the resulting momentum distributions for muons delivered to the Al foils and stopped in the foils.

Stopping target monitor

The Mu2e stopping target monitor has been designed to measure the total number of stopped muons with a relative accuracy of 10% [1], by counting the X-ray emission of the muonic atoms. The highest X-ray yield is due to the 2p→1s radiative transition, corresponding to the arrival of a muon into the ground state. Other lines are also available with significant yields: like the 3p→1s and the 4p→1s

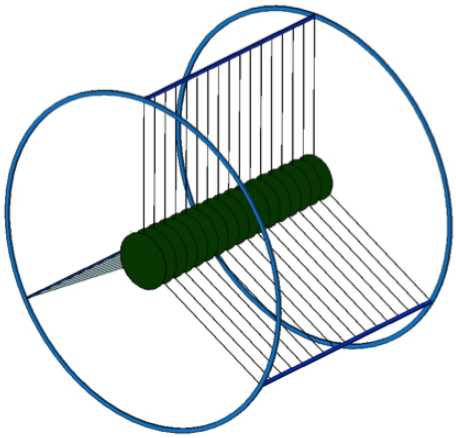

Figure 2.9: Muon stopping target composed of 17 Al foils and its mechanical structure.

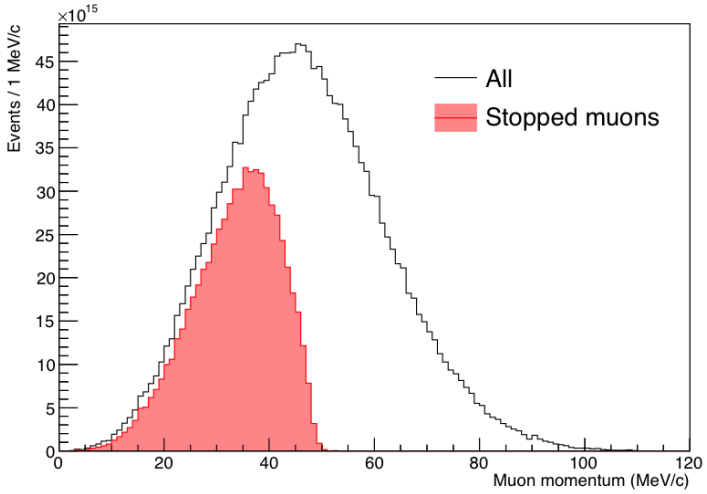

Figure 2.10: Momentum distribution of muons delivered to the stopping target as well as the distribution of muons that stop in the Al foils.

transitions. Moreover, muons that stop in non Al atoms, impurities of the Al foils, can be identified from their typical X-ray emission [1]. To perform the X-rays detection with sufficient accuracy to distinguish and identify all the contributes, use of solid-state Ge detector is a forced choice. Figure 2.11 shows the typical energy spectrum of the muonic X-rays measured with a Ge detector [1]. The Ge

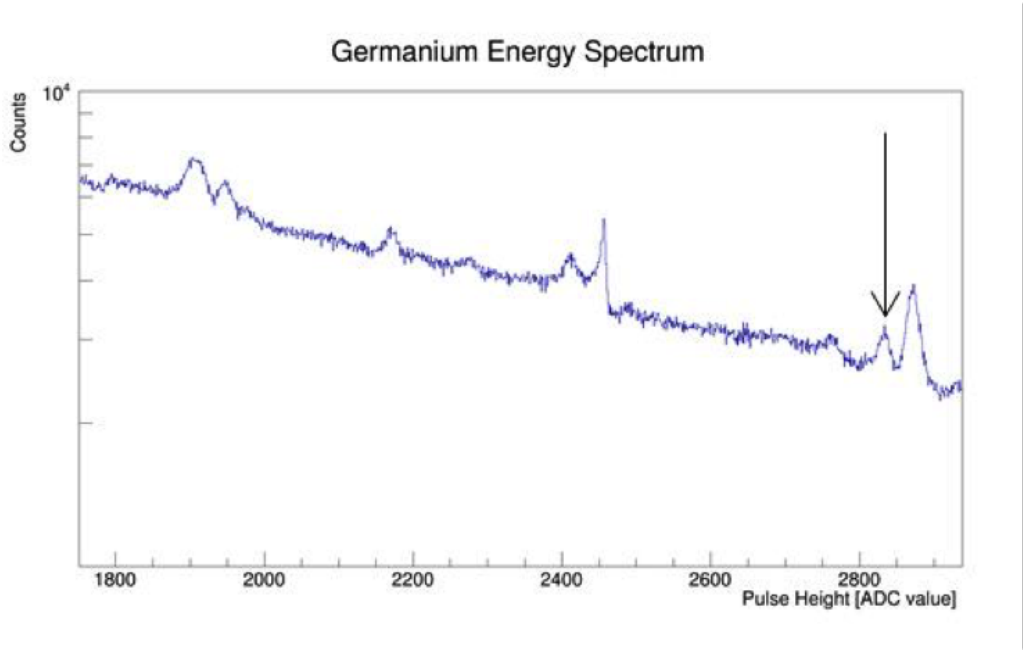

Figure 2.11: Preliminary germanium spectrum from the AlCap experiment at PSI [36]. Muonic aluminum X-ray at 347 keV is clearly visible.

detector is housed in a concrete box, placed downstream to the outer part of the DS to minimize the background fluxes.

2.4 Mu2e detector

The Mu2e detector consists of a low-mass straw tube tracker and a crystal electromagnetic calorimeter. The information from the two detectors is used to perform the CE track reconstruction, and to reject most of the background. A cosmic ray veto system is also present to veto atmospheric muons that can interact in the DS, generating fake CE candidates.

2.4.1 Tracker

The Mu2e Tracker consists of straw tubes aligned transversely to the axis of the DS. The basic detector element is a 25 μm sense wire inside a 5 mm diameter tube made of 15 μm thick metalized Mylar. The tracker consists of about 22,000 straws grouped into 20 measurement stations, which are distributed over a length of $\sim$ 3 m (see Figure 2.12). The assembling element is the panel, which consists

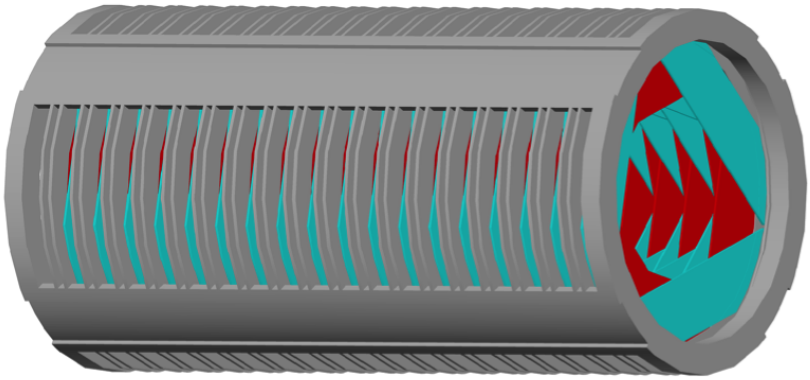

Figure 2.12: The Mu2e straw tube tracker. The straws are oriented transverse to the solenoid axis.

of two layers of straws, as shown in Figure 2.13, to provide mechanical rigidity, and to solve the "left-right" ambiguity. A 1.25 mm gap is maintained between straws to allow for manufacturing tolerance and diameter expansion due to gas pressure. The straws are designed to withstand changes in differential pressure ranging from 0 to 1 atmosphere for operation in vacuum. The straws are supported at their ends by a ring at large radius, outside of the active detector region. Six

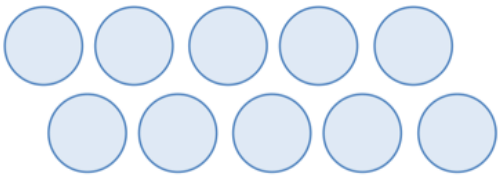

Figure 2.13: A section of a two-layer tracker straw plane. The two layers improve efficiency and help resolve the left-right ambiguity.

panels, rotated by 60 deg, define a plane and, finally, two rotated planes form a station. Figure 2.14 explains a hierarchy of a tracking station assembly.

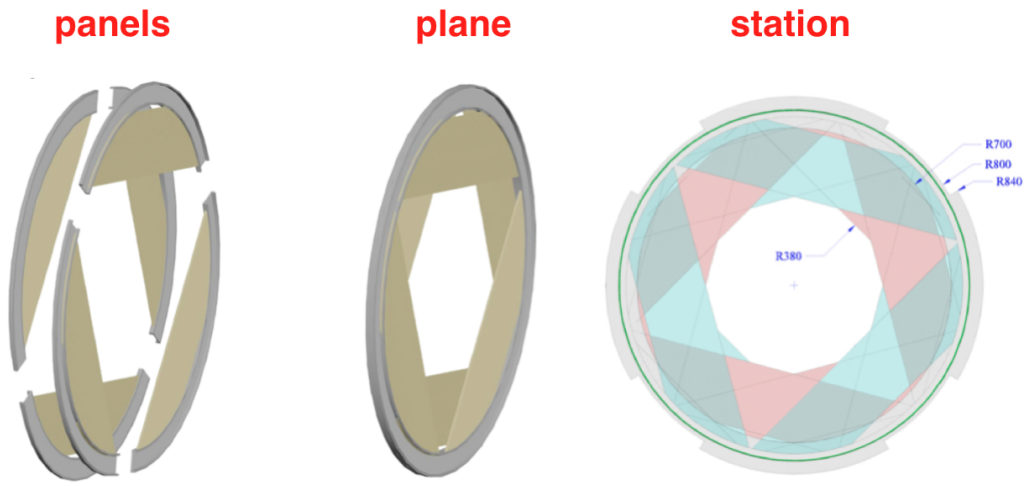

Figure 2.14: Hierarchy of a single tracker station.

Each straw is instrumented at both ends with preamps, and the amplified signals are sent to TDCs and ADCs. TDCs measure the drift time, while ADCs allow dE/dx measurement used to separate electrons from highly ionizing protons. To minimize the amount of feed-throughs, in the vacuum region signal digitization is performed near the tracker, and transmitted though optical fibers. A liquid cooling system is required to maintain an appropriate operating temperature of the electronics in vacuum.

Only a small fraction of the DIO electrons fall into the tracker acceptance. The inner radius of the tracker planes is such that only electrons with energies greater than about 53 MeV fall into the tracker volume (see Figure 2.15): lower energy electrons curl in the solenoidal field and pass unobstructed through the hole in the center of the tracker. Because most of the electrons have energy smaller than 60 MeV, a large fraction of them (97%) do not reach the tracker.

The momentum resolution is pivotal for eliminating the background, and it is required to be better than few hundreds of keV/c [1].

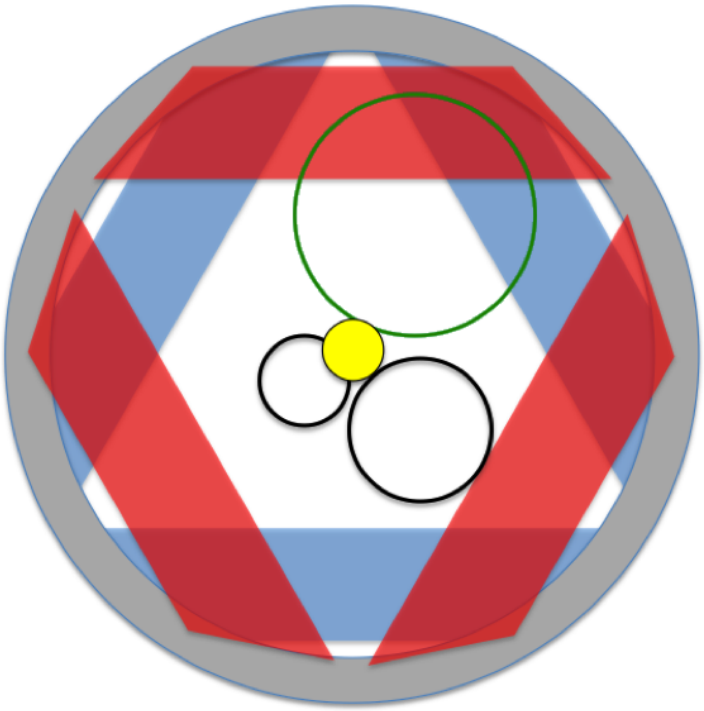

Figure 2.15: Cross sectional view of the Mu2e tracker with the trajectories of a 105 MeV conversion electron (top) and a 53 MeV Michel electron (lower right) superimposed. The disk in the center is the stopping target. Electrons with energies smaller than 53 MeV (lower left), representing most of the rate from muon decays-in-orbit, miss the tracker entirely.

2.4.2 Calorimeter

The crystal calorimeter provides energy, position, and time information. Calorimeter information allows to improve track reconstruction, and to provide a particle identification tool. The calorimeter may also be used to trigger high energy electron candidates, reducing the throughput of the data acquisition system. A more detailed decription of the Calorimeter, and its expected performance, is given in the next chapter.

2.4.3 Cosmic Ray Veto

Cosmic-ray hitting the muon stopping target or other materials in the detector region can produce particles mimicking CE events. Passive shielding (overburden above and on the sides of the detector enclosure, and the neutron shield surrounding the TS and DS), eliminates background sources other than penetrating muons. On each side, the cosmic ray veto system (CRV) consists of four layers of extruded scintillator bars with embedded wavelength shifting fibers that are read out with Silicon photomultipliers (SiPMs). The CRV surrounds the DS on 3 sides (Figure 2.16) and extends up to the midpoint of the TS. The Veto signal is produced by the coincidence of adjacent counters in different layers. In the region of the muon stopping target the Cosmic Ray Veto is 99.99% efficient.

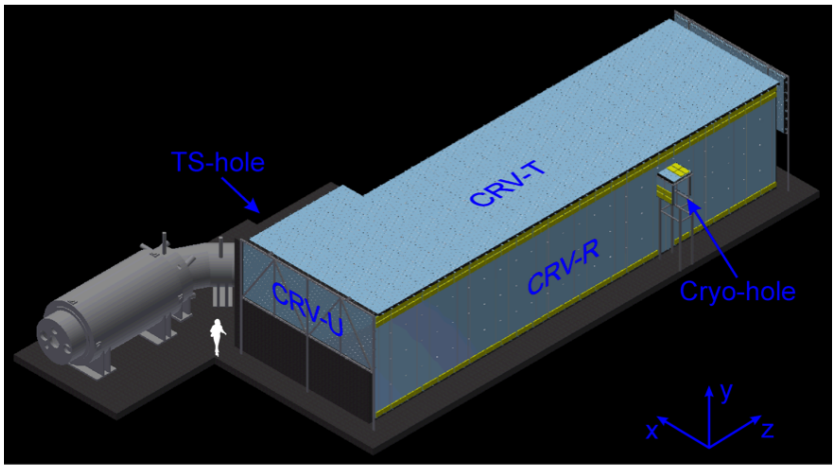

Figure 2.16: View of the Cosmic Ray Veto.

Approximately one conversion-like event per day from cosmic-ray muons is expected: the cosmic ray veto is expected to reduce that rate to 0.10 events during the entire running period. The passive shielding, between the CRV and the DS, has been designed in order to minimize the CRV dead time, generated by the intense neutron flux, coming primarily from the muon stopping target. Most of the neutrons have kinetic energies below 10 MeV, with the most probable energy at 1 MeV. Recent studies [1] show that the rate in the counters comes primarily from gammas that are produced from neutron capture on hydrogen. Passive shielding outside the TS and DS moderates and capture most of the neutrons. The magni-

tude and pattern of energy deposition in multiple layers of scintillator is expected to be different for neutrons and muons, and therefore false veto signals from neutrons can be redued to an aceptable level.

Chapter 3

The calorimeter

3.1 Requirements

The Mu2e calorimeter has been designed to satisfy the following requirements [1]:

- energy resolution $\simeq O(5\%)$ @ 100 MeV;
- time resolution better than 500 ps @ 100 MeV;
- shower apex spatial resolution $\simeq$ 1 cm @ 100 MeV;
- radiation hardness for an expected dose of about 10 krad/year and a neutron flux of about 10^{10} neutrons 1 MeV-equivalent/cm^2/year;
- efficiency in vacuum (10^{-4} Tor) and in magnetic field (1 Tesla);

The calorimeter is able to provide:

- seeding of the pattern recognition in the track reconstruction;
- particle identification capabilities;
- an independent trigger to measure and monitor the track reconstruction efficiency.

The first two points are extensively discussed in chapters 5 and 7. The calorimeter-based trigger is presented in chapter 3.7.

3.2 Design

The calorimeter consists of two disks whose dimensions were optimized to maximize the acceptance for CEs. Figure 3.1 shows the two identical disks with an inner (outer) radius of 35.1 (66) cm and a relative distance of 75 cm, corresponding to $\sim \frac{1}{2}$ pitch of the helical CE trajectory. Each disk is composed of ~ 930 square scintillating crystals $20 \times 3.3 \times 3.3$ cm^3.

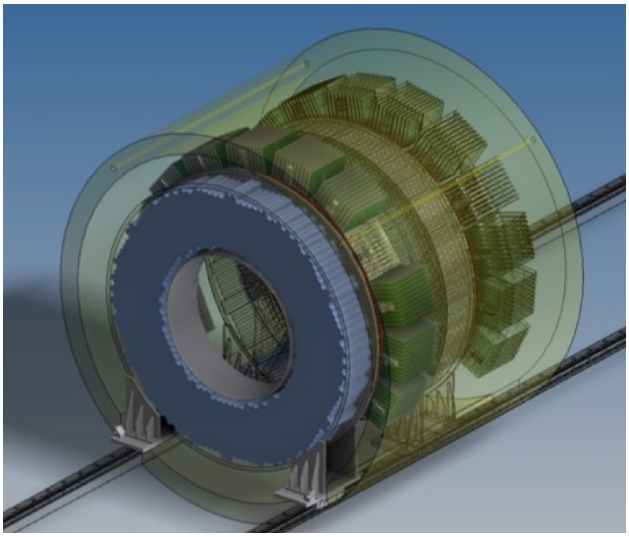

Figure 3.1: Calorimeter design.

3.3 Crystal choice

In the Conceptual Design Report [37] the calorimeter baseline choice was based on LYSO crystals. Since then, an extensive R&D program has been carried out to study this option [38, 39]. Unfortunately, the large increase in price of Lu_2O_3 salt over the past years made the cost of a LYSO calorimeter unaffordable. Table 3.1 compares properties of LYSO with those of two crystals taken into consideration, i.e. BaF_2 and undoped CsI. Both crystals very similar properties in terms of light yiels and radiation length. BaF_2 needs to be coupled with a photosensor able to

Crystal	**BaF_2**	**LYSO**	**CsI**
Density [g/cm^3]	4.89	7.28	4.51
Radiation length [cm] X_0	2.03	1.14	1.86
Molière radius [cm] R_m	3.10	2.07	3.57
Interaction length [cm]	30.7	20.9	39.3
dE/dx [MeV/cm]	6.5	10.0	5.56
Refractive Index at λ_{max}	1.50	1.82	1.95
Peak luminescence [nm]	220, 300	402	310
Decay time τ [ns]	0.9, 650	40	16
Light yield (compared to NaI(TI)) [%]	4.1, 3.6	85	3.6
Light yield variation with temperature [$\%/^\circ C$]	0.1, -1.9	-0.2	-1.4
Hygroscopicity	Slight	None	Slight

Table 3.1: Properties of the studied crystals.

suppress the slow component of the emission spectrum. Absence of a "solar-blind" photosensor made this option unaffordable. So CsI has been selcted has the final choice.

Undoped CsI has an emission spectrum [40] (Figure 3.2) characterized by: a fast emission peak at 315 nm with a time structure composed of two decay components at 16 and 35 ns, and a slow emission with a decay time of $\sim 1\mu$s that produces a continuous emission spectrum in the wavelength region of 380-600 nm. It has been reported [41] that the intensity of the slow emission can be reduced via thermal annealing.

To study the optical properties of CsI, samples 23 $\times$ 2.9 $\times$ 2.9, or 30 $\times$ 5 $\times$ 5 cm^3, from different vendors have been tested [1] using a UV-sensitive photomultiplier tube (PMT) R2059 [42]. Figure 3.3 shows on the left side the weighted longitudinal transmittance (EWLT) of the CsI, defined as

$$\text{EWLT} = \frac{\int \text{LT}(\lambda)\text{Em}(\lambda)d\lambda}{\int \text{Em}(\lambda)d\lambda}$$

where LT(λ) is the light transmittance and Em(λ) is the emission spectrum. The corresponding EWLT at the emission peak is below 50%. The light output (LO), defined as the number of photoelectrons produced per MeV deposited in the crystal, and the longitudinal response uniformity (LRU) measurements were carried

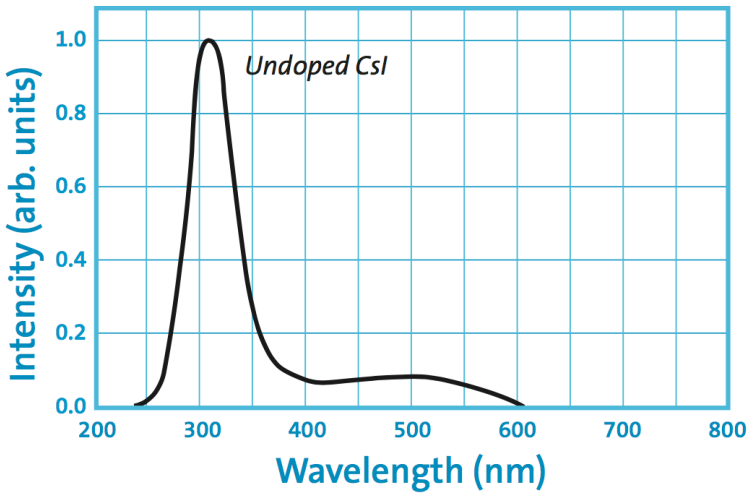

Figure 3.2: Undoped CsI emission spectrum.

out by illuminating crystals along the axis with a ^{22}Na source. One of the 511 keV annihilation photons was used as a tag to clean the spectrum. Figure 3.3 shows on

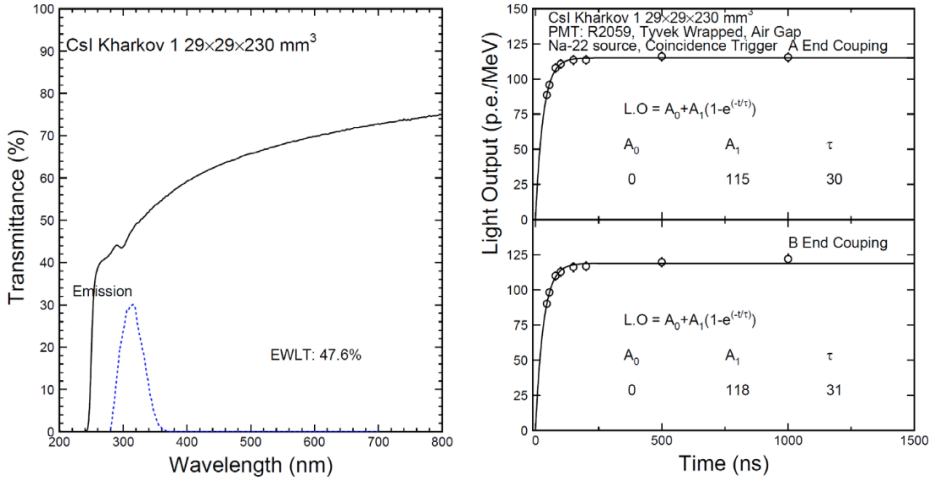

Figure 3.3: CsI EWLT (left) and LO (right).

the right the LO as a function of the ADC integration time (the crystal was read from both ends). The dependence of the response on the integration time is well

described by the function:

$$LO(t) = A_0 + A_1(1 - \exp(-t/\tau)) \ ,$$

where A_0 and A_1 are the LO of the slow and fast component respectively, and τ is the decay time of the fast component. Fit results show that the slow component is negligible. The LRU has been studied by measuring the LO along the axis: the

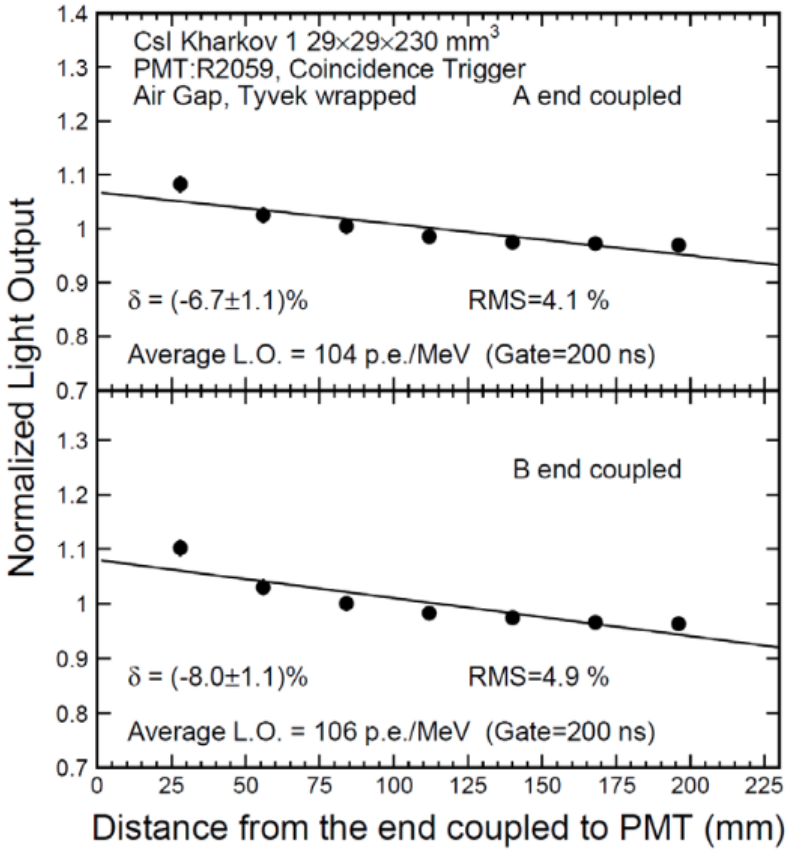

Figure 3.4: CsI LRU measured from both ends.

corresponding data (Figure 3.4) were well fit to a line. CsI shows a LO increment of about 7% toward the side closer to the readout.

3.4 Photosensor choice

For the CsI crystals, the proposed photosensor is a TSV-SPL MPPC from Hamamatsu [43]. Blue markers in Figure 3.5 show its photo-detection efficiency (PDE) compared to other similar devices [43, 44]. In the UV range 250-350 nm, where the CsI emission spectrum peaks, the PDE of this UV-enhanced MPPC ranges between 30 – 40%, which is a factor of about 6 better than a standard MPPC from Hamamatsu [44]. Signals from the anodes of the MPPC are serialized, and the

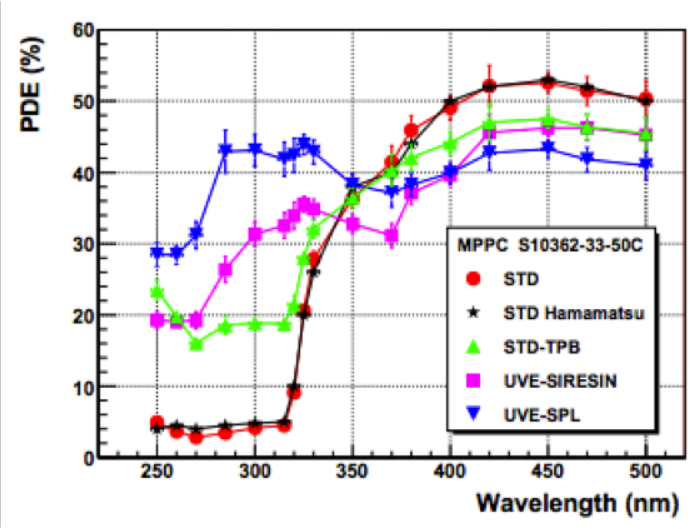

Figure 3.5: PDE versus wavelength for several model of MPPC.

resulting signal is passed to a custom board that performs the shaping and the amplification of the signal. Data are then digitized and serialized with the 12 bit, 250 MHZ waveform digitizer custom-boards [1]. All boards are linked in a daisy chain via optical fibers to send the data to data-acquisition servers located outside the Detector Solenoid.

3.5 Radiation hardness

Charged particles, photons, and neutrons affects crystals and of the readout electronics performance. Scintillating crystals change their properties due to absorbed dose through the formation of color centers, which affect light transmittance and, potentially, the LRU. A detailed simulation of the expected background has been performed, including all expected radiation sources:

- the contribution from the beam flash;
- DIO electrons;
- neutrons, protons and photons produced in the stopping target via nuclear capture;
- particles produced by muons stopped outside the Al stopping target (OOT).

3.5.1 Dose

The expected dose by the calorimeter disks is 20 krad/year in the inner rings (radius smaller than 38 cm) and about 3 krad/year in the outer one. The distribution of the crystal dose as a function of the radius is shown in Figure 3.6; the dose is dominated by the contribution of the beam flash, with a smaller component from DIO for the inner crystal rings. Other sources are almost negligible. Under ir-

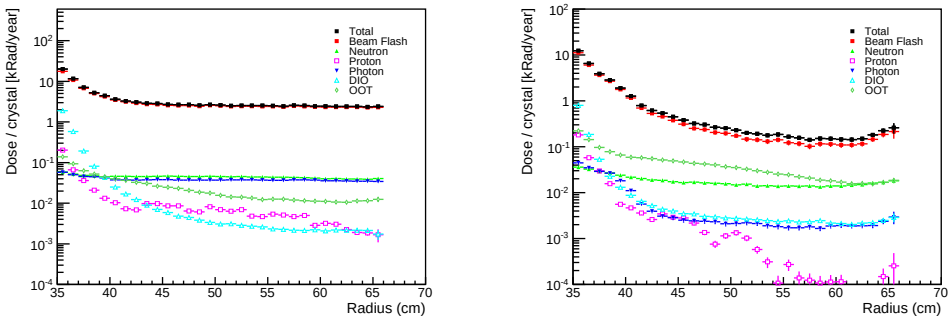

Figure 3.6: Dose in the front (left) and back (right) disk as a function of the radial distance from the DS axis.

radiation, the scintillating properties of CsI degrade. Figure 3.7 shows how the

EWLT and the LO vary for CsI as a function of the integrated dose. Up to 10

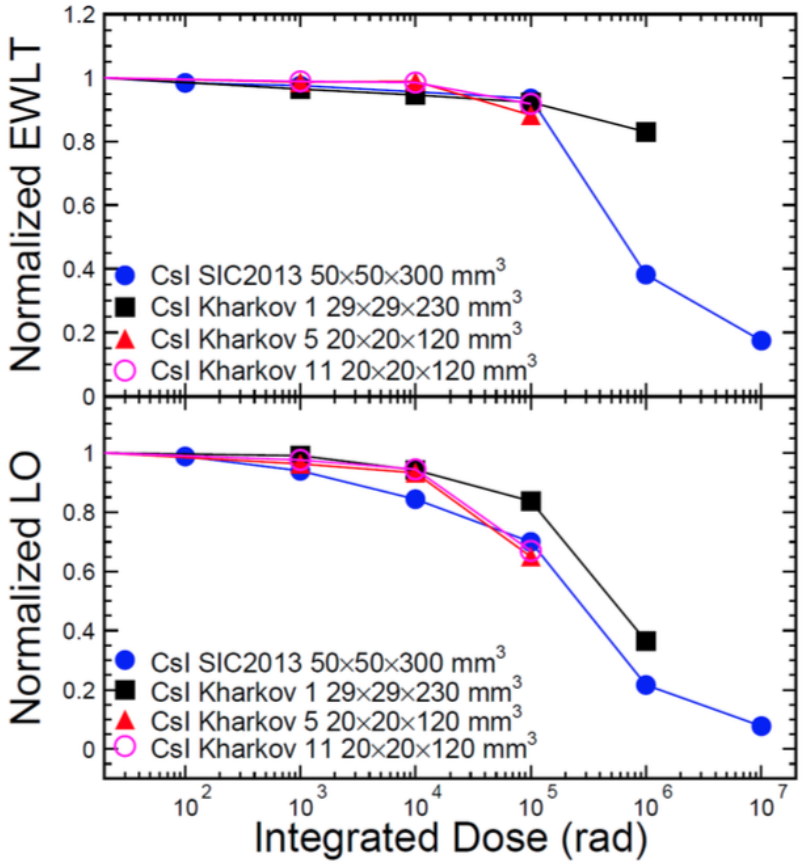

Figure 3.7: EWLT and LO as a function of the irradiated dose for undoped CsI.

krad, which is the dose/year expected in the inner most rings of the calorimeter (Radius < 38 cm), undoped CsI shows a drop of few percentages in the LO and the EWLT.

3.5.2 Neutron flux

In neutron interactions, the energy is primarily deposited by non-ionizing processes, resulting in displacement damage from atoms displaced from their position in the lattice structure. For neutron energies between 50 keV and 14 MeV, the

neutron-matter interaction mainly proceeds through neutron-neutron elastic scattering (n,n), or inelastic neutron-neutron scattering (n,n'), neutron-proton (n, p) and neutron-alpha (n,α) interactions. About half of the neutron energy is transferred to the nucleus (detailed calculations are given in Ref. [45]). The displacement damage induced by neutrons in Si based devices is usually normalized to the damage induced by 1 MeV neutrons, referred to as "1 MeV equivalent damage" [46]. Figure 3.8 shows the equivalent damage induced by neutron interactions as a function of their kinetic energy. The neutron flux at the front face of

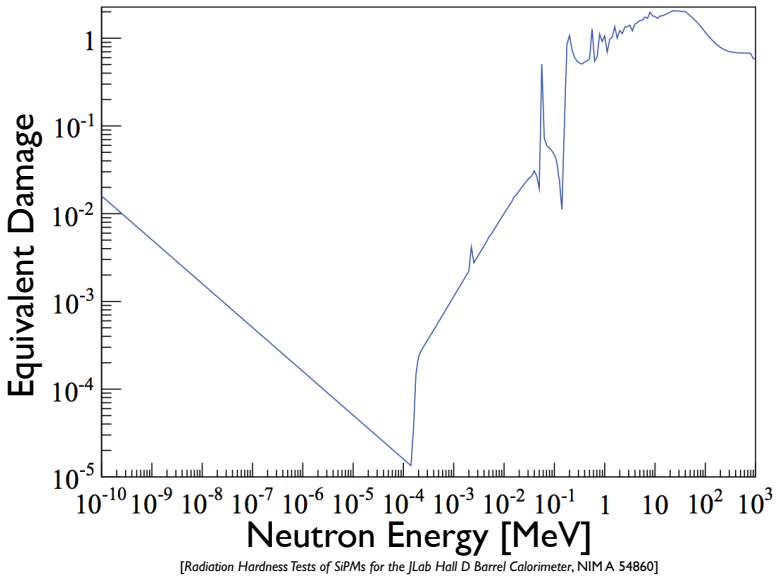

Figure 3.8: Equivalent damage versus neutron kinetic energy.

each disk is shown in Figure 3.9. The neutron flux at the front face of the first disk is fairly uniform and on average is $\phi_n \sim 2 \cdot 10^{11}$ neutrons/cm^2/year. In the second disk, the neutron flux peaks in the inner region at about 10^{11} neutrons/cm^2/year, because is not shielded by the first disk, and goes down to $4{\cdot}10^{10}$ neutrons/cm^2/year in the outer part, due to the shielding effect provided by the first disk. The number of neutrons absorbed by the crystals is easily obtained by taking the difference of the ϕ_n from these plots, which is of about $\sim 10^{11}$ neutrons/cm^2/year.

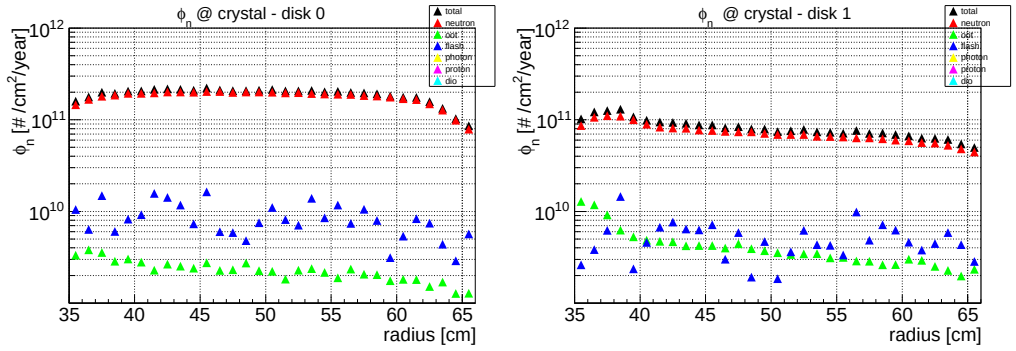

Figure 3.9: Neutron flux (ϕ_n) as a function of the radial position at the front face of the first (left) and second (right) disk. Background sources representing less than 1% of the total flux are not shown.

The 1 MeV-equivalent neutron flux in the back side of each disk, where the photosensors and the front end electronics are located, is obtained weighting the neutron flux using the damage curve shown in Figure 3.8. The 1 MeV-equivalent neutron flux as a function of the radial position is shown in Figure 3.10. The average flux is at the level of $\sim 3 \cdot 10^{10}$ ($\sim 10^{10}$) neutrons 1-MeV equivalent/cm^2/year for the front (back) disks, and rises up to $\sim 9 \cdot 10^{10}$ ($\sim 3 \cdot 10^{10}$) neutrons 1-MeV equivalent/cm^2/year for the innermost crystals.

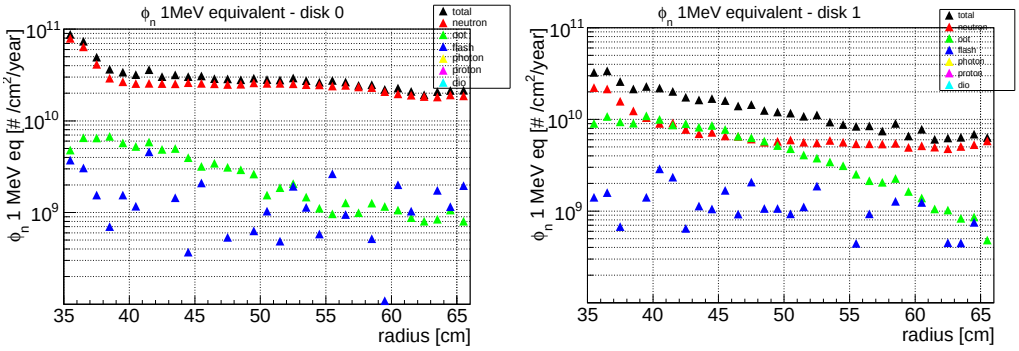

Figure 3.10: 1 MeV-equivalent neutron flux as a function of the radial position at the back face of the front (left) and back (right) disk. The backgrounds representing less than 1% of the total flux are not drawn

Recent studies [47] showed how optical properties of CsI change as a function of the neutron flux. Tests have been performed using ^{252}Cf sources to irradiate CsI

crystals. Figure 3.11 shows negligible variations in the EWLT and the LO up to 10^{11} neutrons/cm^2.

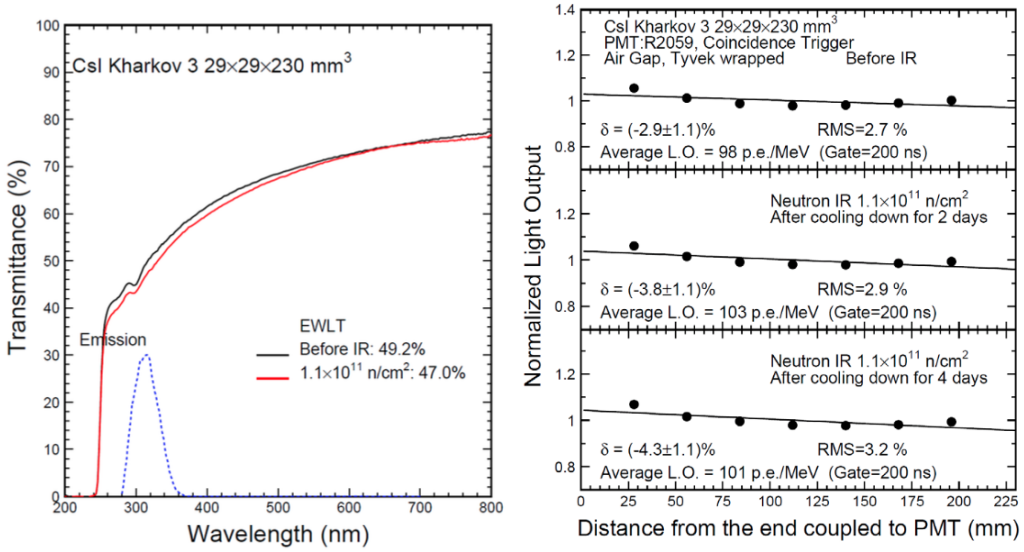

Figure 3.11: EWLT (left) and LO (right) as a function of the neutron flux.

3.6 Calibration system

A liquid radioactive source (Fluorinert^{TM}) is used to provide an absolute energy scale and the equalization in response of the crystals. This liquid source circulates through aluminum pipes on both disks surface, and is activated by a neutron source, producing the following decay chain:

$$\begin{aligned} {}^{19}F + n &\rightarrow {}^{16}N + \alpha \\ {}^{16}N &\rightarrow {}^{16}O^* + \beta^- + \bar{\nu}_e \ (\tau_{1/2} = 7\text{s}) \\ {}^{16}O^* &\rightarrow {}^{16}O + \gamma(6.13 \text{ MeV}) \end{aligned}$$

The liquid source circuit, represented in Figure 3.12, consists of 12 Al pipes, 0.5 mm thick, with a diameter of 3/8 inches and a length which ranges from 1.5 to 1.7 m. The selected geometry allows to have an uniform illumination of the disk with variation in the intensity less then 5% [48]. Figure 3.13 shows the calorimeter

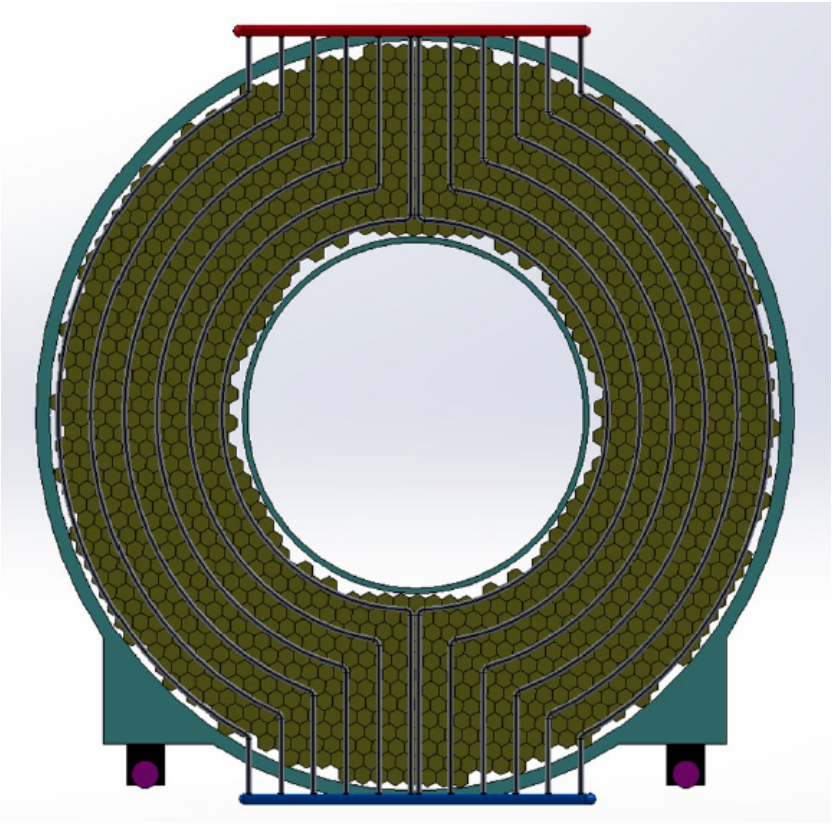

Figure 3.12: Liquid source circuit scheme.

energy response to these photons, where the large peak results from the sum of the full absorption peak, of the escape peaks at 5.62 and 5.11 MeV and the Compton spectrum.

The change in the crystal optical transmittance and photosensor gains is monitored continuously by a laser system, following a scheme similar to the one used for CMS [49]; each crystal is illuminated by UV light irradiated from the back of each crystal via fused silica optical fibers [1]. A reference monitor station based on PIN diodes is used to control the variation in the laser source intensity. The basic scheme of the laser system is shown in Figure 3.14.

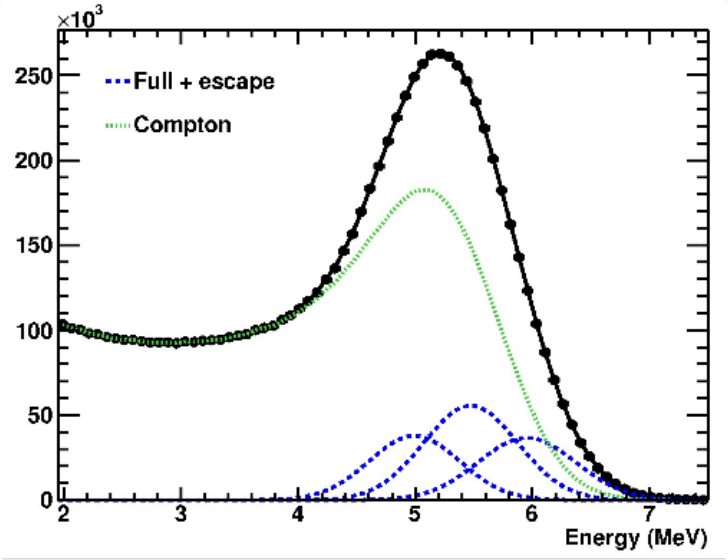

Figure 3.13: Energy spectrum for a crystal irradiated with 6.13 MeV photons from an $^{16}O^{*}$ source.

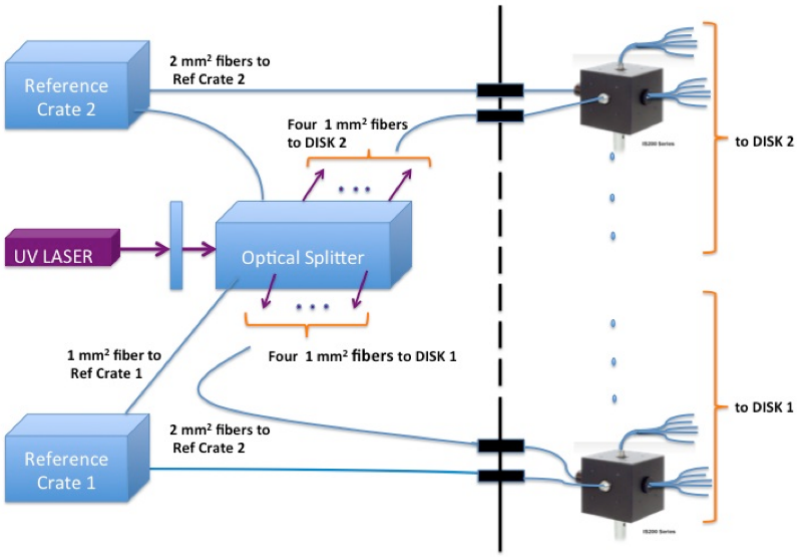

Figure 3.14: Laser system scheme.

3.7 Simulation of the calorimeter performance

Calorimeter performance has been studied using Monte Carlo simulations. Event simulation proceeds in several steps. The interaction of the incident particle with the crystals is first simulated by GEANT4 [50], then the energy deposition is converted into optical photons, taking into account fluctuations of the photo-statistics. Pulse shapes are then simulated in the following ways. First hits are grouped in a fixed time window, next the waveform, measured during experimental tests, is applied for each group of hits, and summed them up. The generated pulses are then processed for reconstructing the time and the energy. Time is reconstructed by performing a fit of the leading edge with an analytic function, while energy is reconstructed by integrating the pulse (detailed description of both algorithms is reported in the next chapter). Calorimeter clusters are finally reconstructed by means of a dedicated algorithm described in the next section.

3.7.1 Cluster reconstruction

The clustering algorithm starts by taking the crystal with the largest reconstructed energy as a seed, and adding one by one crystals that satisfies the following requirements:

- have a common side with the crystals already included;
- have reconstructed time within ± 10 ns from the seed crystal time;
- have reconstructed energy 3 times larger than the expected electronic noise.

3.7.2 Energy resolution

The energy resolution has been estimated by simulating $\mu^-\mathrm{N} \rightarrow e^-\mathrm{N}$ conversion electrons (E=104.97 MeV) together with the expected background. Figure 3.15 shows the distribution in energy residuals between the reconstructed cluster energy (E) and the Monte Carlo ($\mathrm{E_{MC}}$). The distribution shows an higher left tail due to the leakage. The energy resolution has been estimated with FWHM/2.35 of the distribution, which is of about 5 MeV.

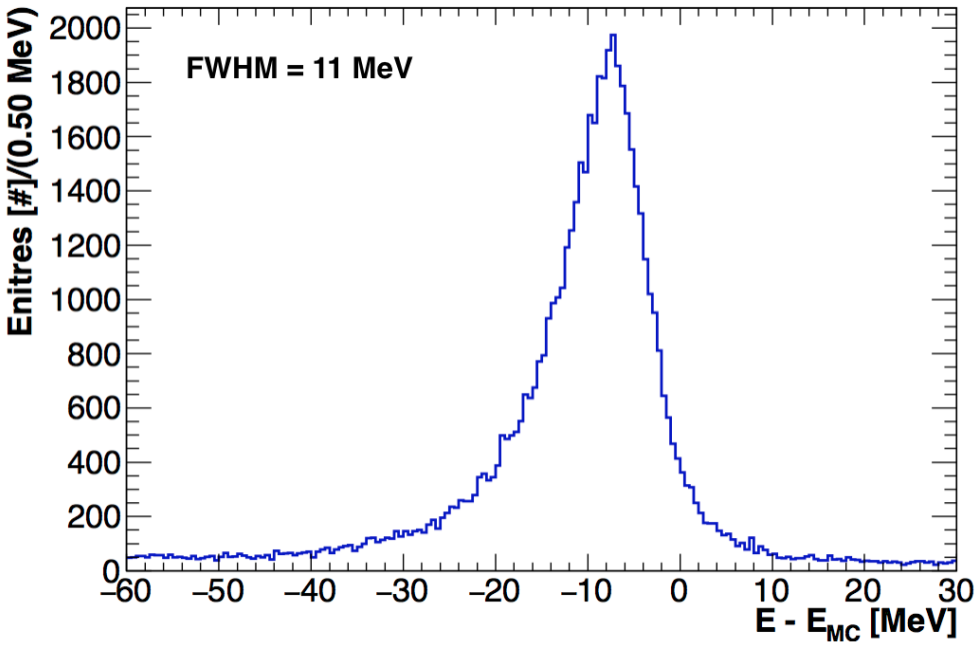

Figure 3.15: Distribution in energy residuals between the reconstructed cluster energy and the Monte Carlo value.

3.7.3 Coordinate resolution

The cluster position is necessary to match the reconstructed tracks with the calorimeter cluster. These coordinates are obtained using the linear energy weighted mean. The coordinate resolution has been estimated by simulating $\mu^-\mathrm{N} \rightarrow e^-\mathrm{N}$ conversion electrons together with the expected background. Figure 3.16 shows the distributions in track-cluster position residuals. A Gaussian fit of the distribution shows a sigma of about 1.4 cm along the x and y directions. The track extrapolation resolution on the calorimeter is of about 4 mm [1], so these plots represent a reasonable estimate of the expected cluster coordinate resolution.

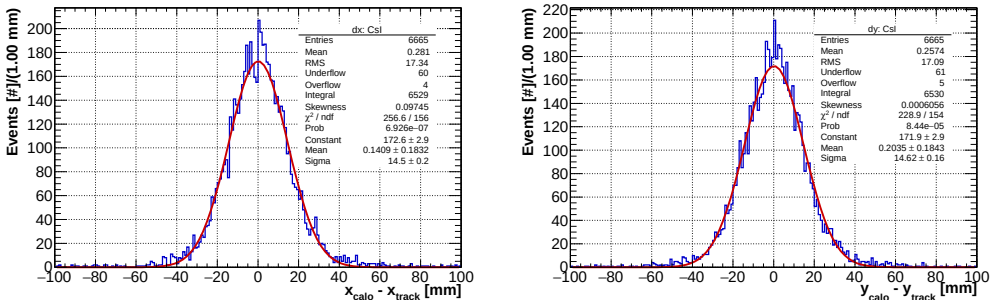

Figure 3.16: Distribution in position residuals along the x (left) and y (right) directions between the reconstructed cluster position and the track position extrapolated to the calorimeter.

3.7.4 Time resolution

As already mentioned, the simulation of the digitization process has been modeled using as input the waveform acquired with an experimental test setup. The cluster time has been defined as the linear energy weighted time of all the crystals belonging to the cluster. The time resolution has been estimated by simulating $\mu^-\mathrm{N} \rightarrow e^-\mathrm{N}$ conversion electrons. Figure 3.17 shows the time residuals between the reconstructed cluster time and the Monte Carlo truth. A Gaussian fit to this distribution shows that the expected time resolution is of about 110 ps.

3.7.5 Calorimeter trigger

Calorimeter data are processed by the data-acquisiton (DAQ) servers, and can be used to provide a trigger completely independent from the tracker. The trigger algorithm relies on an energy threshold on the reconstructed cluster energy. Efficiency and performance of the trigger have been studied using simulated $\mu^-\mathrm{N} \rightarrow e^-\mathrm{N}$ events, including the expected background coming from nuclear capture processes, and from the beam interactions with the stopping target. Figure 3.18 shows on top the corresponding DAQ rate as a function of the energy threshold, and on the bottom the DAQ rate as a function of the CE efficiency for several trigger energy thresholds. With a trigger threshold of 70 MeV the DAQ rate is lowered down from 590 (trigger-less configuration [1]) to 60 kHz, while keeping the efficiency on the CE higher than 90%.

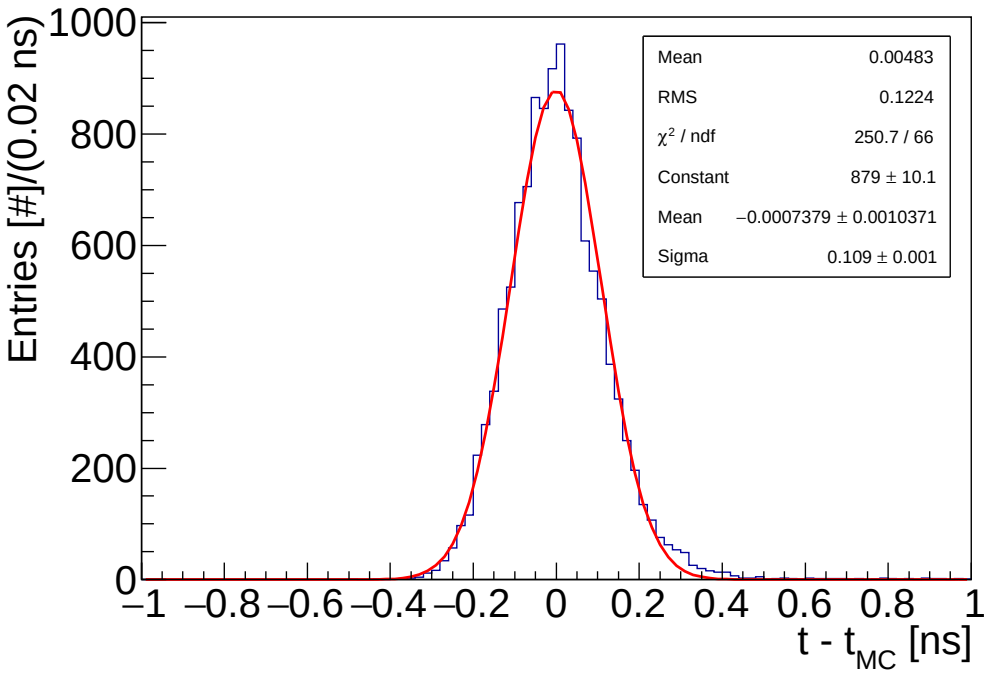

Figure 3.17: Distribution in time residuals between the reconstructed cluster time (t) and the Monte Carlo truth (t_{MC}).

The calorimeter trigger is important also to select samples of events independently from the track reconstruction algorithm, which can be used for measuring the track reconstruction efficiency.

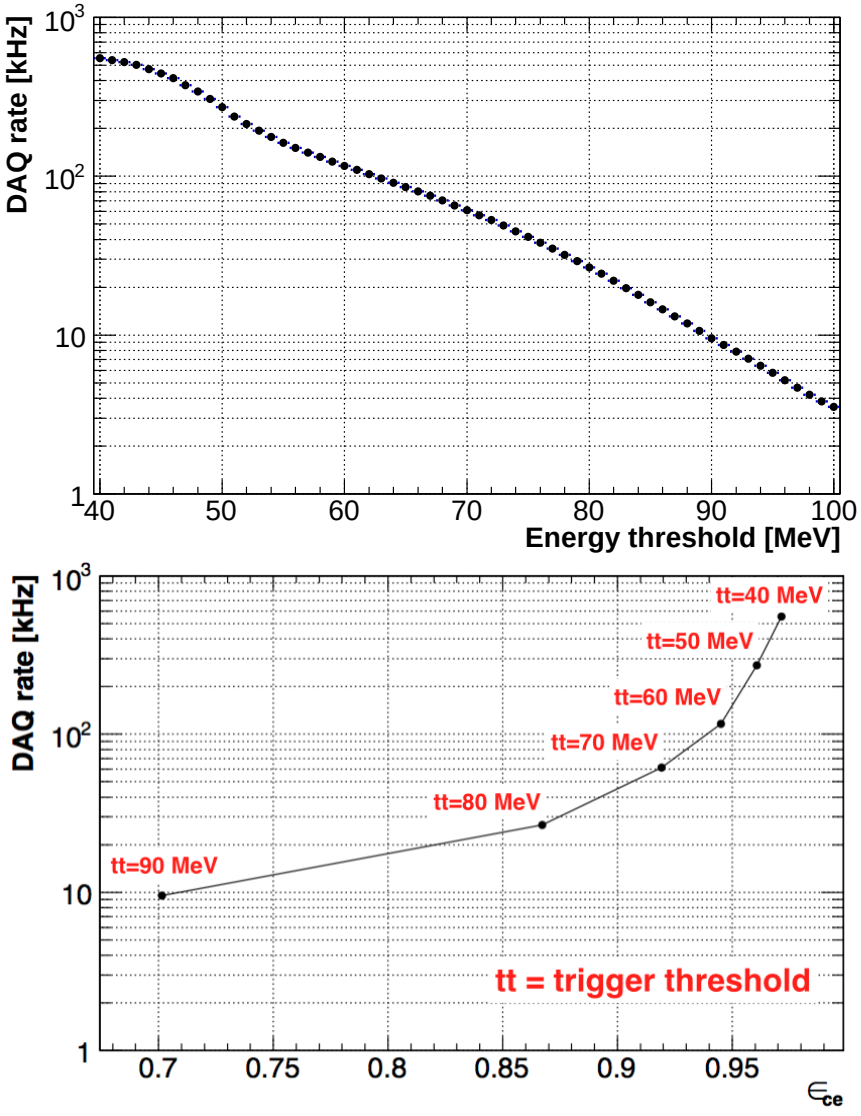

Figure 3.18: DAQ rate versus the trigger energy threshold (top) and the DAQ rate versus the CE efficiency for some trigger thresholds (bottom).

Chapter 4

Calorimeter prototype test

As discussed in the previous chapter, the Mu2e calorimeter is required to have a time resolution better than 0.5 ns for CEs. To demonstrate that a CsI based calorimeter satisfies this requirement, a dedicated beam test was set up during April 2015 at the Beam Test Facility in Frascati (Italy) [51]. Time and energy measurements have been performed using a low energy electron beam, in the energy range [80,120] MeV.

The photostatistics of the fast CsI component produces about 2000 optical photons per MeV; therefore in the energy range around 100 MeV photostatistics may be a major factor limiting the energy and time resolution. However, time resolutions better than 1 ns have been reported in the literature, see for example [52]. Recently, time resolution better than 0.5 ns was measured with the undoped CsI calorimeter at 100 MeV using the PMT-based readout combined with the signal waveform digitization at 125 MHz [53].

In this chapter a complete description of the beam test analysis is presented and discussed.

4.1 Experimental setup

The calorimeter prototype consisted of nine $3 \times 3 \times 20$ cm^3 undoped CsI crystals wrapped into 150 μm of Tyvek®, and arranged into a 3×3 matrix. Out of the nine crystals, two were produced by Filar OptoMaterials [54], while the remaining 7

came from ISMA [55]. Each crystal was previously tested with a ^{22}Na source to determine the LO and the LRU. All crystals showed acceptable properties:

- LO: about 90 pe/MeV, when read out with a UV-extended PMT R2059 by Hamamatsu [42] coupled through an air gap;
- LRU: LO variation at both ends of the crystals was smaller than 0.6%/cm.

Each crystal has been coupled to a large area 9×9 mm^2 MPPC-TSV from Hamamatsu [43] by means of the Rhodorsil 7 silicon paste [56]. The operating voltage was set at 55 V, about 3 V above the breakdown voltage, corresponding to an average gain of 1.3×10^6 and a PDE of about $35-40\%$ at 300 nm [43]. An MPPC is an array of single Silicon Photomultiplier (SiPM) and each of them has an anode. To get a single pulse from of several anodes, a front-end electronics (FEE) board has been used for each MPPC. The FEE provides a single pulse amplified by a factor 8.

The coincidence of the signals from two $5 \times 1 \times 2$ cm^3 plastic scintillating counters, crossed at 90 deg, was used for triggering the incoming beam. Figure 4.1 shows the positioning of the beam counters with respect to the prototype. In addition, another coincidence of the signals from two $10 \times 30 \times 4$ cm^3 scintillating counters was used to provide a cosmic ray trigger. Figure 4.2 shows the orientation of the cosmic ray counters with respect to the prototype.

Photosensors signals coming from the crystals and the scintillating counters were read out with the 12 bit, 250 MHz waveform digitizer boards V1720 from CAEN [57].

Coincidences of each pair of signals from the scintillating counters, one triggering the beam and the other for the cosmic rays, were used for triggering the data acquisition system.

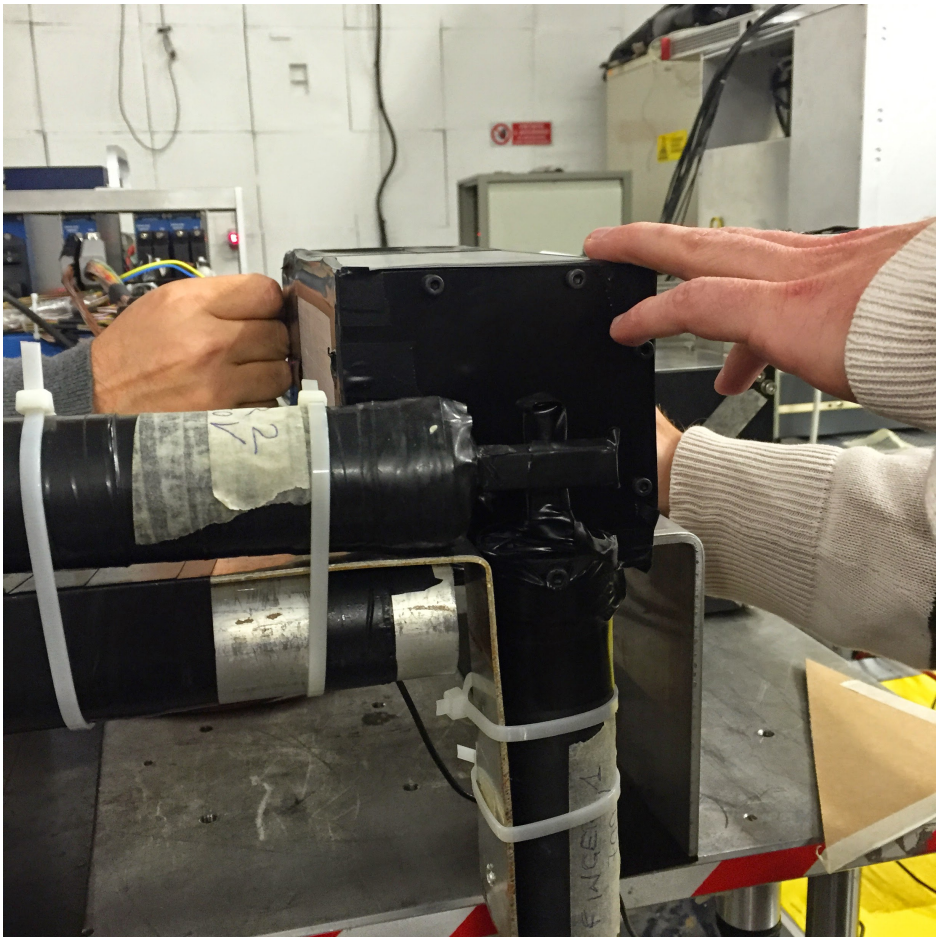

Figure 4.1: The CsI calorimeter prototype with the crossed trigger scintillating counters in front of it.

Two configurations schematically shown in Figure 4.3 were studied during the test:

1. beam at 0 deg with respect to the prototype front face, defined as the side opposite to the photosensors;
2. beam at 50 deg with respect to the prototype surface.

Figure 4.4 shows the system of reference adopted for the numbering.

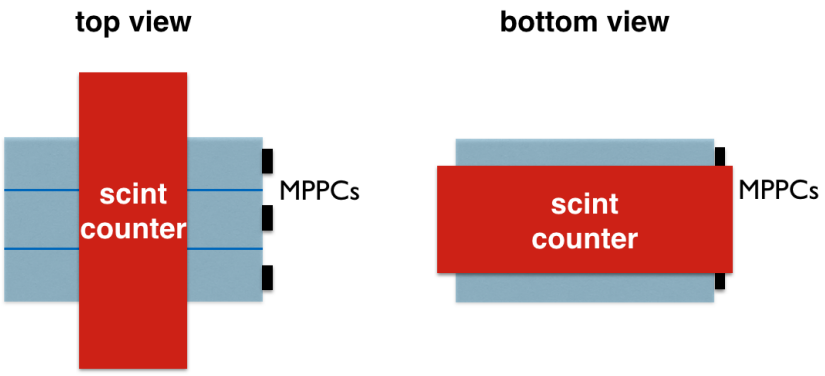

Figure 4.2: Cosmic ray counter orientation.

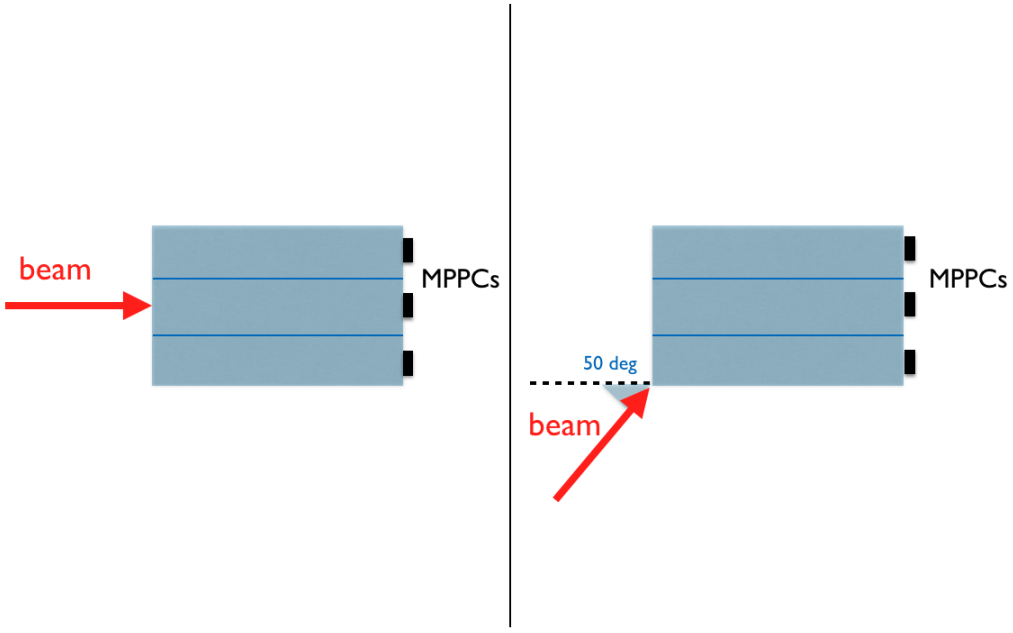

Figure 4.3: Beam test configurations: beam normal to the prototype front face (left) and beam at 50 deg with respect to the normal of the prototype surface (right).

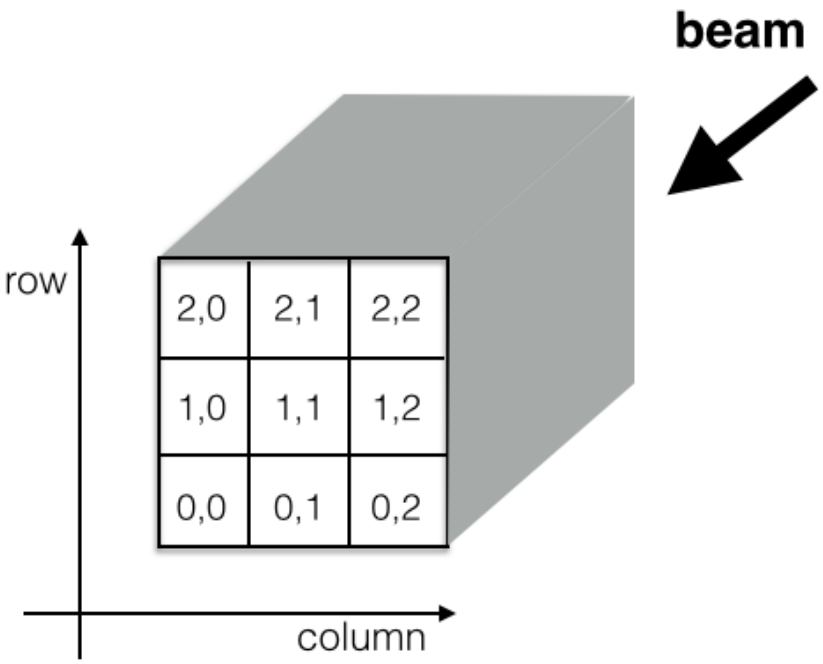

Figure 4.4: Crystal indexing.

4.2 Charge and time reconstruction

A waveform sampling-based readout allows to design deadtime-less data acquisition system, and is more and more widely used in particle and medical physics. In addition, this kind of system allows a more accurate analysis of the signals, which can be helpful to solve typical problem of high intensity experiments, like the pile-up.

The total charge and the time of the detected pulse were determined from the digitized waveform as follows. The signal time has been determined by fitting the leading edge of the waveform with an analytic function, and defining the pulse

time based on the fit results. Assuming a constant pulse shape, the best accuracy can be achieved by setting the signal time with a threshold fixed at a constant fraction of the pulse height. Pivotal for this procedure, usually called digital constant fraction (DCF), are the choices of: fit function, fit range, and threshold. Several parametrizations were tested, like: single and double exponential functions, their integrals over the sampling units, exponential functions convoluted with a Gaussian, log-Normal function $\exp(-(\ln x - \mu)^2/2\sigma^2)$, and several others. For each case, a scan over the DCF threshold and the fit range has been performed. The best result was obtained with the asymmetric log-Normal function [58] defined as:

$$f(t) = N \exp\left(-\frac{\ln^2\left[1 - \eta(t - t_p)/\sigma\right]}{2s_0^2} - \frac{s_0^2}{2} \right) \frac{\eta}{\sqrt{2\pi}\sigma s_0} , \tag{4.1}$$

where N is the normalization parameter, t_p is the position of the peak, $\sigma = \mathrm{FWHM}/2.35$, η is the asymmetry parameter, and s_0 can be written as

$$s_0 = \frac{2}{\xi} \mathrm{arcsinh}\left(\frac{\eta\xi}{2}\right), \quad \xi = 2.35 .$$

This can be understood, as the asymmetric log-Normal function captures several important features of the electronic pulse, like start of the pulse development at a finite time $t = t_p + \sigma/\eta$, exponential growth at a very early stage of the pulse development, and presence of the pulse maximum.

The charge was estimated by numerical integration of the waveform; two time windows of 400 ns were used as integration gates in order to guarantee the full integration of the signals from the CsI crystals. The first gate was used to estimate the pedestal Q_{ped} at early time, where no pulse is present, and the second gate, around the signal peak, was used to integrate the signal charge Q_{signal}. The reconstructed charge was then defined as $Q_{reco} = Q_{signal} - Q_{ped}$.

Scintillating counter waveforms

In the beam test scintillating counters had signals with a very steep leading edge, about 15 ns (2-3 samples), and a total width less than 100 ns. Since the asymmetric log-Normal is defined by 4 parameters, the necessary fit range exceeds 15 ns. The lower edge of the fit was set at the first sample where the signal exceeds 5 mV, while the upper edge was set 16 ns after the peak. Figure 4.5 shows an example of a typical signal fit.

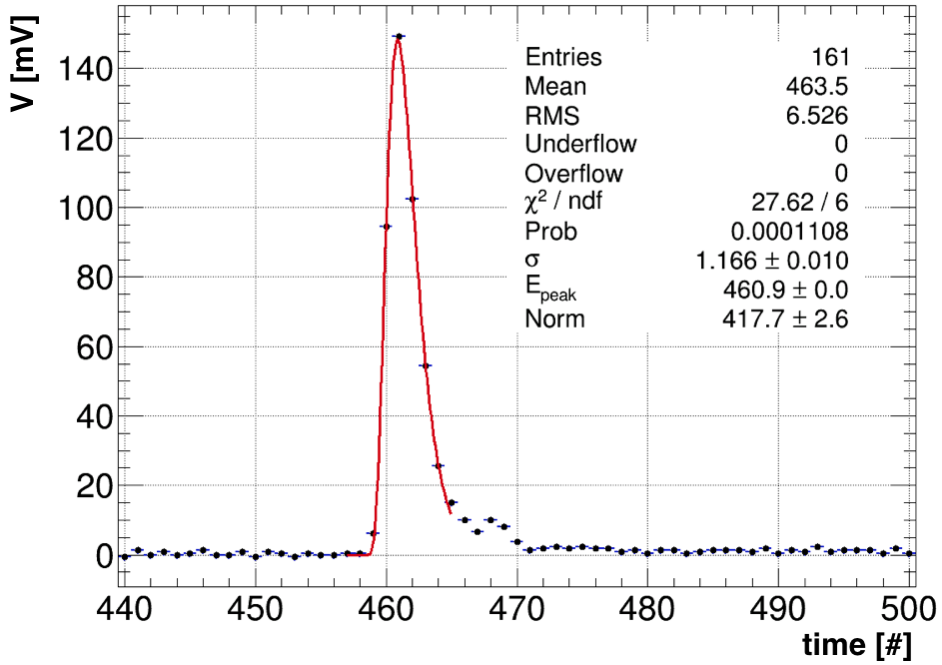

Figure 4.5: Fit of a scintillating counter waveform using a log-Normal function.

This procedure was checked looking the distribution in number of degrees of freedom (N_{DOF}) and χ^2/N_{DOF} . The distributions in N_{DOF} in Figure 4.6, shows that

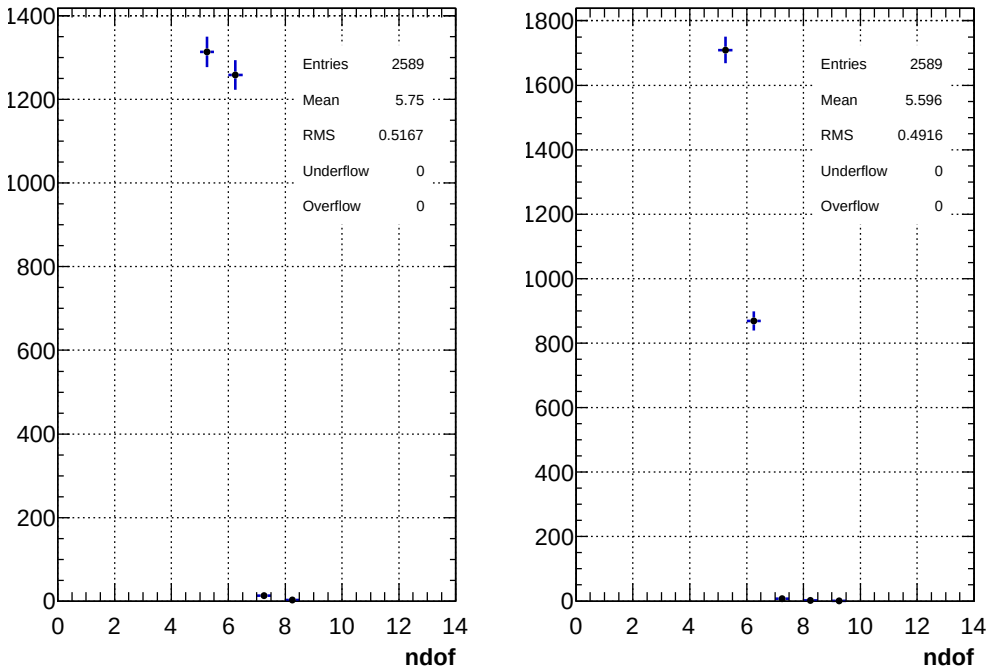

Figure 4.6: Distribution in N_{DOF} for the two scintillating counters.

the selected range provides more than 8 samples to perform the fit.

The χ^2/N_{DOF} distribution, see Figure 4.7, shows that the error set to the points has been underestimated, because the mean of the χ^2/N_{DOF} distributions is larger than 1. Presence of systematic effects has been investigated also looking at the

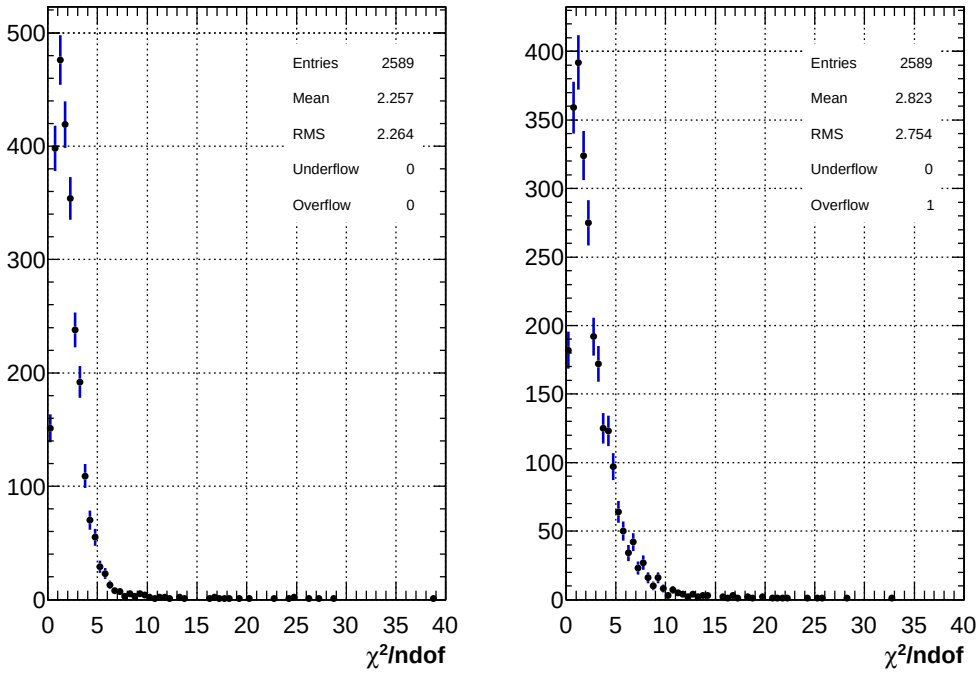

Figure 4.7: χ^2/N_{DOF} distribution.

distribution of the reconstructed time within the digitized sample (Δt_{edge}). Figure 4.8 shows the distributions in Δt_{edge} for both scintillating counters. Fit results of these distributions to a constant show that they are reasonably flat.

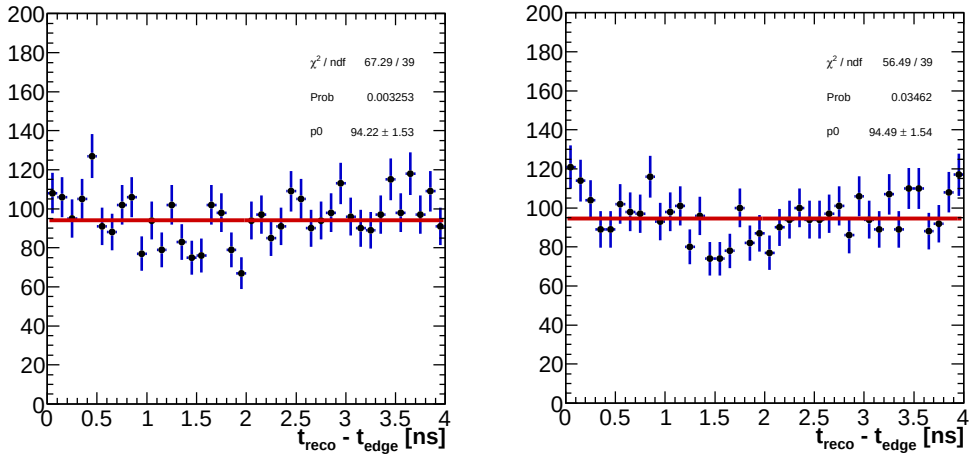

Figure 4.8: Distribution in time residuals between the reconstructed scintillating counter time (t_{reco}) and the edge of the corresponding digitized sample. Red line shows the fit result to a constant.

CsI crystal waveforms

Waveforms corresponding to signals from the CsI crystals have the leading edge of about 25 ns, and a total width of about 300 ns. The width of the leading edge allows to perform the fit only on this part of the signal. The fit range has been defined as follows; the lower limit was set at the first time sample where the pulse exceeds 0.5% of the pulse maximum, while the upper limit - at the first time sample where the pulse exceeds 85% of the pulse maximum. The DCF threshold, used to determine the reconstructed time, has been optimized using the data taken with a 80 MeV electron beam at 0^o incidence angle.

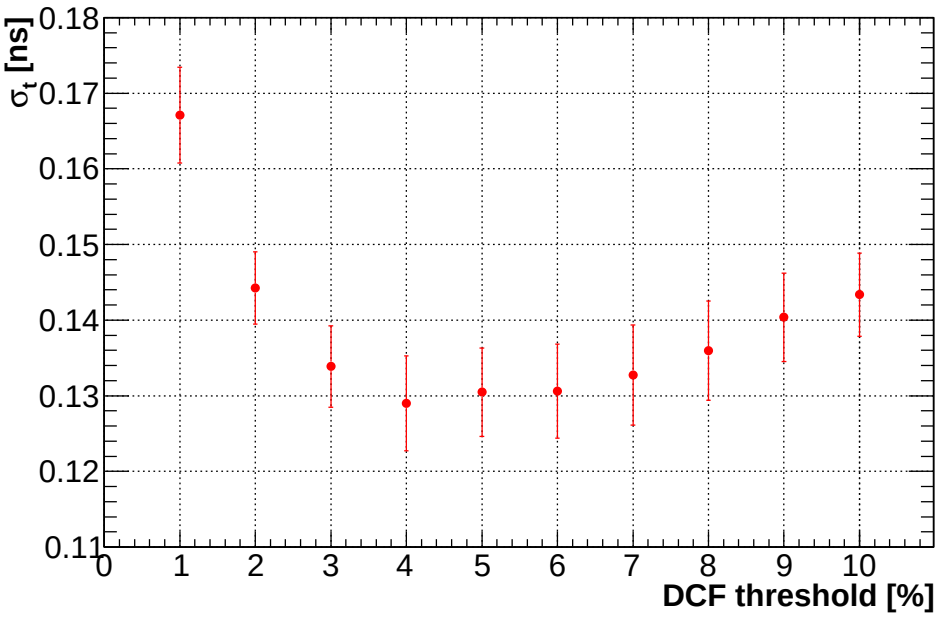

Figure 4.9: Time resolution using 80 MeV electron beam as a function of the DCF threshold.

Figure 4.9 shows that for the thresholds in the range 2% - 10% of the maximal pulse height, the time resolution is stable within 10%. So the DCF threshold has been set to 5% of the maximum pulse height. Figure 4.10 shows as an example, the fit results for a large and a small pulse.

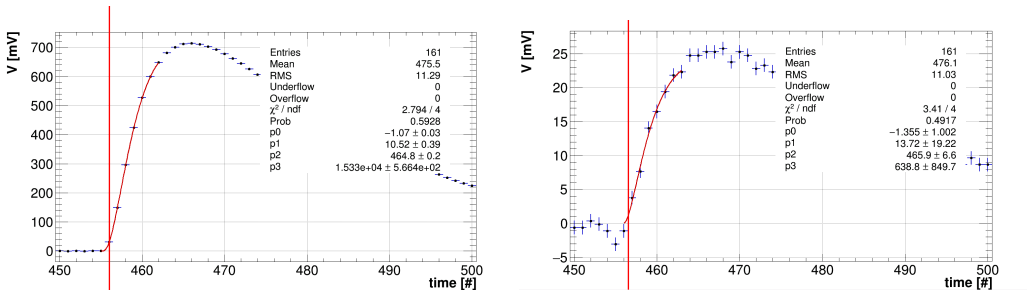

Figure 4.10: Example of waveform fit for a large (left) and a small (right) pulse.

Figure 4.11 shows that the χ^2/N_{DOF} distribution looks normal. The distribution in N_{DOF} , see Figure 4.11, shows that, for CsI pulses, the selected fit range includes 7-8 points.

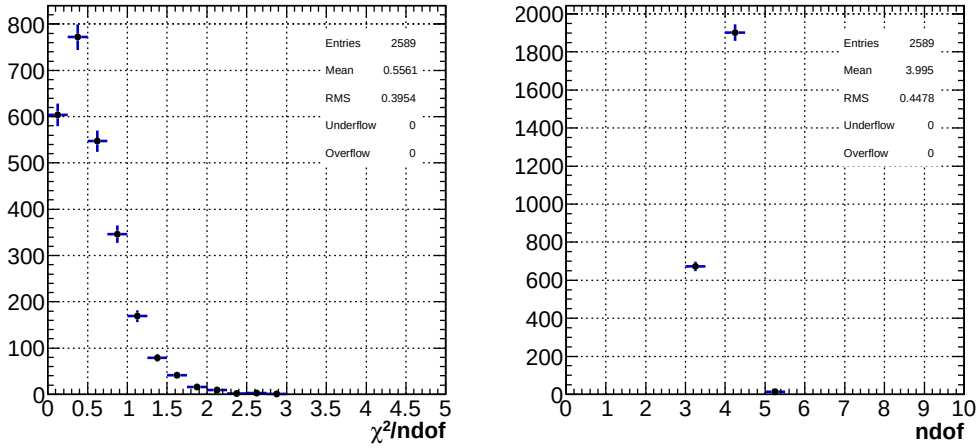

Figure 4.11: χ^2/N_{DOF} distribution (left) and distribution in N_{DOF} (right).

Important note is that the distribution in Δt_{edge} in Figure 4.12 is flat and does not show any significant systematic effect.

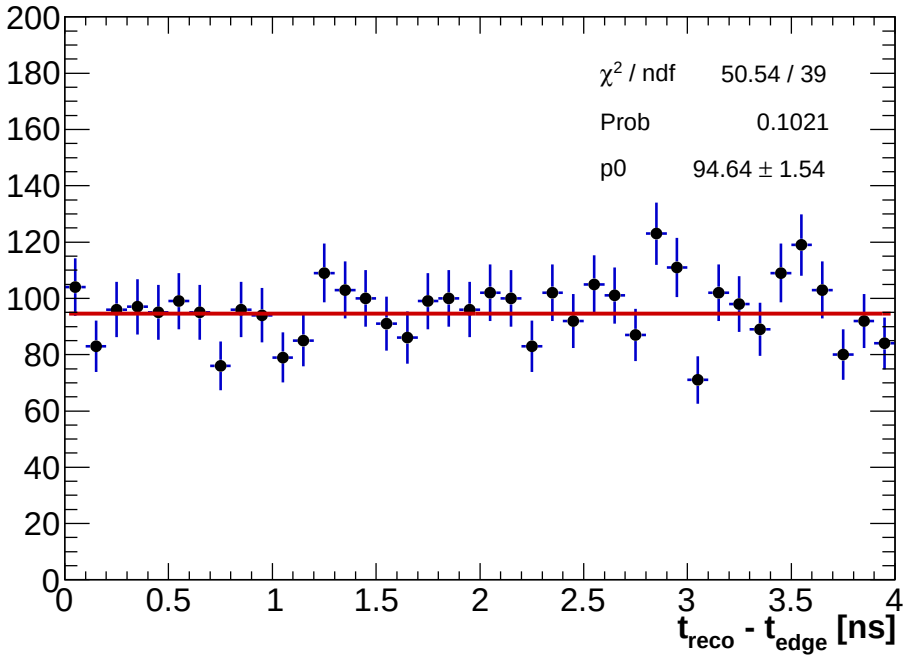

Figure 4.12: Distribution of the reconstructed time of the CsI pulses within their respectively digitized sample. Red line shows the fit result to a constant.

4.3 Analysis selection

Events with a single beam particle, within the integration gate, were selected requiring:

1. Energy deposition in the beam counters consistent with the single particle.
2. Pulse shape discrimination on the waveforms from the CsI crystals, to discard events with one or more channels saturated because of pileup.

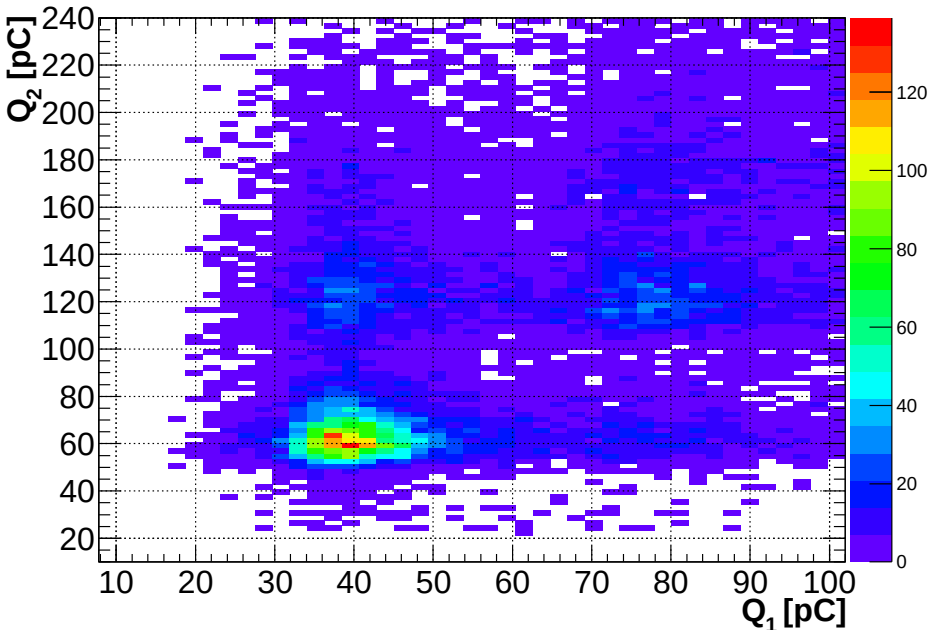

Figure 4.13: Scatter plot of the reconstructed charges in the two scintillation counters used for triggering the beam.

Figure 4.13 shows the scatter plot of the charges reconstructed in the beam counters, Q_1 and Q_2. The cuts applied for selecting the single particle events are the following: $Q_1 \in [30, 50]$ pC and $Q_2 \in [50, 80]$ pC. However, this selection was not sufficient to discard events with more than 1 electron. Figures 4.14 show two examples of saturated signals in events surviving the scintillating counter selection. For that reason, an additional selection has been made using a discriminator

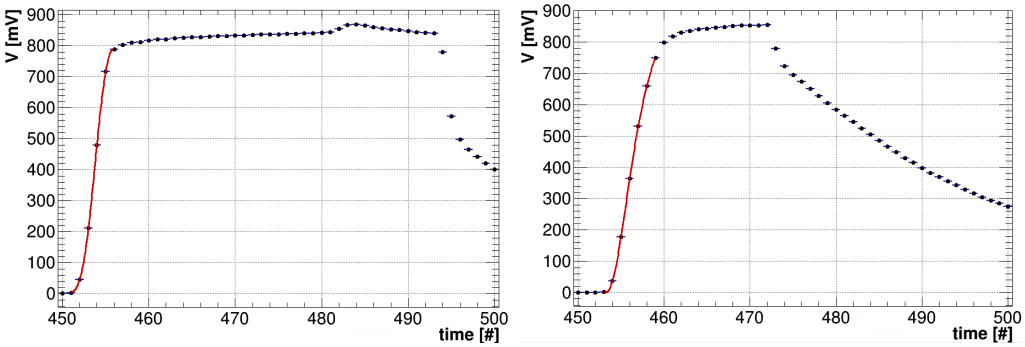

Figure 4.14: Saturated signals read out by the channel (0, 0). Red lines show the fit result used for the time reconstruction.

variable, psd, defined as follows:

$$\text{psd} = \frac{\int_a^b \text{Waveform}}{\text{Total waveform charge}} ,$$

where a and b are respectively the time samples at 1% of the maximum pulse height on the leading edge, and 90% of the maximum pulse height on the trailing edge. Figure 4.15 shows, as an example, the distribution in psd as a function of the reconstructed charge for the channel (0, 0). The psd cut has been set at 0.36. Discrimination with the psd variable allows its use at any beam energy without changing the cut value.

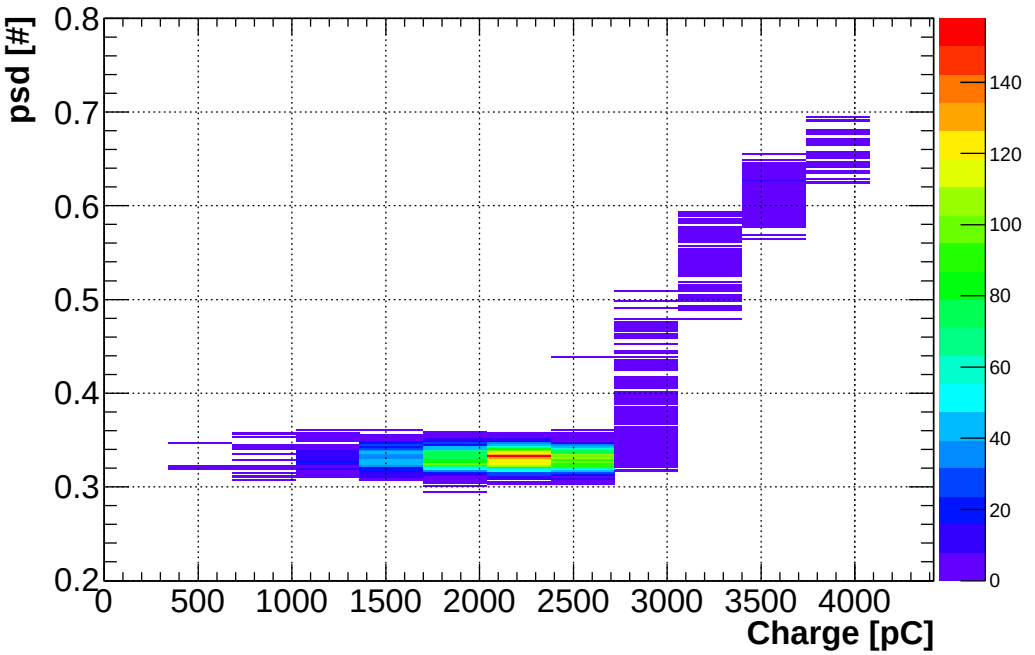

Figure 4.15: Pulse shape discriminator variable versus the reconstructed charge.

4.4 Calibration

Response of the prototype channels was equalized performing runs with a 80 MeV beam at 0 deg centered on each crystal. Figure 4.16 shows the charge distributions of the scanned crystals resulting from the equalization runs. The peak positions, determined from the asymmetric log-normal fit to the charge distributions, were used to equalize the crystal response. The resulting equalization factors were within [0.93, 1.02]. The calibration of the global energy scale has been performed using the beam at 0 deg in the energy range [80, 120] MeV, varying the energy with 10 MeV step. An additional point at E $\sim$ 20 MeV was included using the cosmic ray data (a detailed description of the cosmic ray selection follows in section 4.5.3). The global energy scale has been determined comparing data with the results obtained by means of a GEANT4 [50]-based Monte Carlo simulation. Figure 4.17 shows a linear fit to these points.

The equalization runs were also used to determine the time walk corrections of

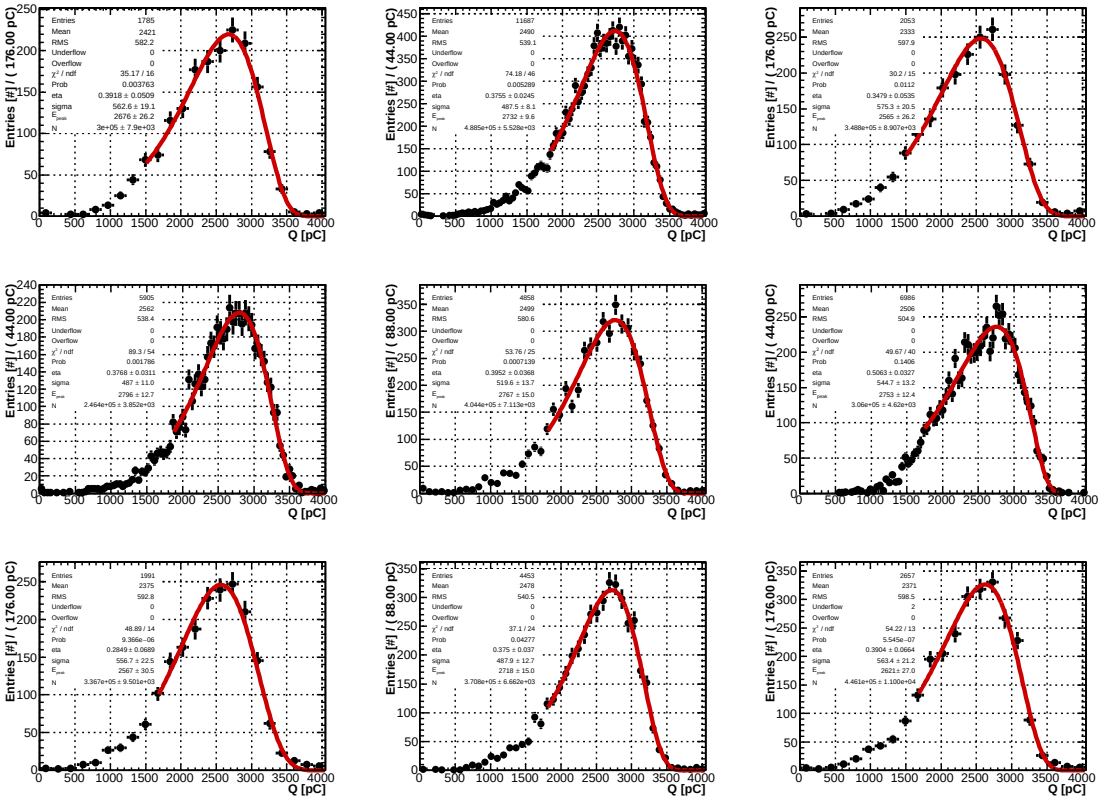

Figure 4.16: Distribution in charge (given in pC) from the calibration runs for all the calorimeter channels.

the prototype channels. A reference time t_{scint} was set as the average of the beam counter reconstructed times ($t_{\text{scint:1,2}}$): $t_{\text{scint}} = (t_{\text{scint:1}} + t_{\text{scint:2}})/2$. Figure 4.18 shows that for the beam energies in the range [80, 120] MeV, the jitter of t_{scint}, defined as the standard deviation of its distribution in each run, is of about 100 ps, with fluctuations smaller than 4%. The time of each channel (i, j), has been defined as:

$$t(i,j)_{\text{corr}} = t(i,j) - t_{\text{scint}} \ ,$$

where t(i, j) is the time reconstructed in the crystal (i, j). Figure 4.19 shows the correlation between $t(i,j)_{\text{corr}}$ and the reconstructed charge for the prototype channels. Distributions in the same Figure show a charge dependence of $t(i,j)_{\text{corr}}$ that

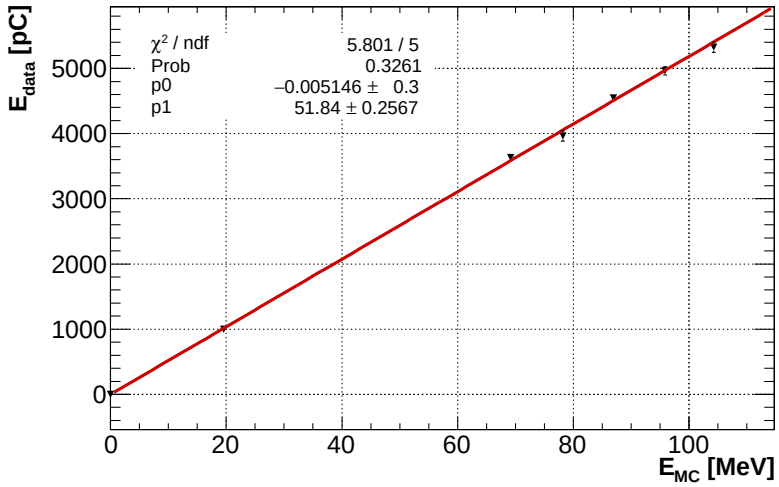

Figure 4.17: Reconstructed total charge of the prototype in the calibration runs (E_{data}) versus the expected prototype energy deposition from the Monte Carlo simulation (E_{MC}).

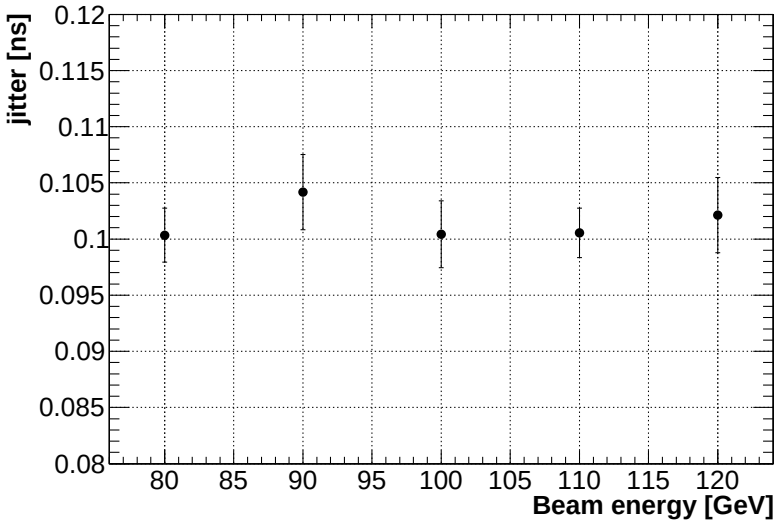

Figure 4.18: Jitter of $t_{scint} = (t_{scint:1} + t_{scint:2})/2$ versus the beam energy.

is well described by the following function:

$$f(Q) = p0 + p1/\sqrt{Q}\,,$$

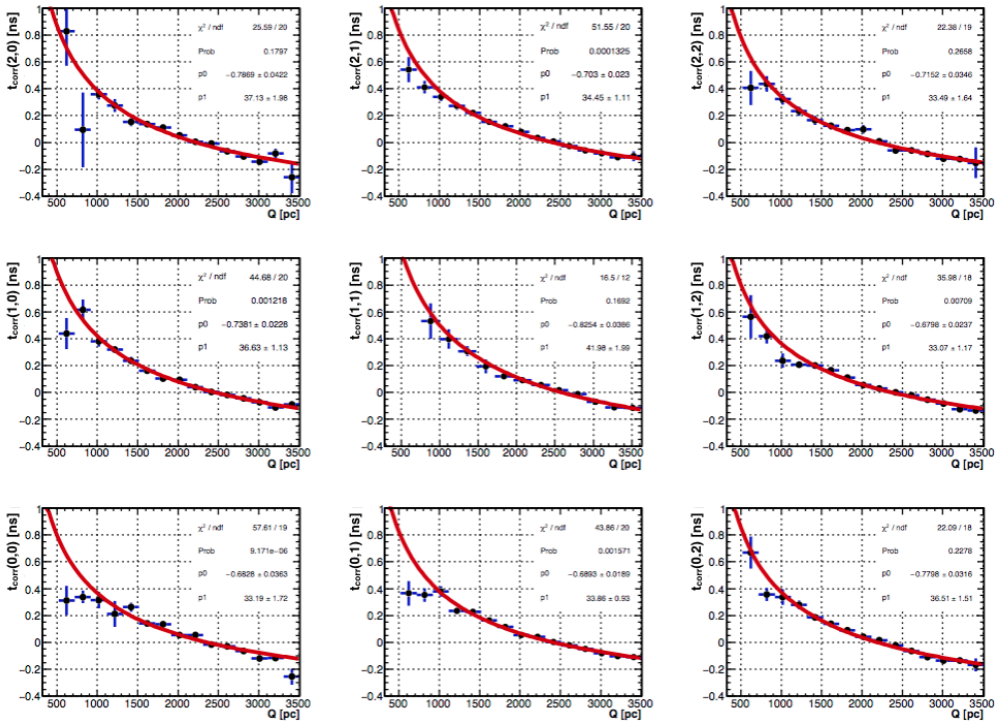

Figure 4.19: $t(i,j)_{corr}$ versus channel charge Q (i,j). Distributions are fit to: $f(Q) = p0 + p1/\sqrt{Q}$

where p0 and p1 are free parameters. For signals with charge $Q > 1000$ pC (~ 20 MeV), the corrections stay within 0.5 ns. Using the fit results, another correction on t_{corr} was made, defining $t_{crystal}$ as follows:

$$t_{crystal}(i,j) = t_{corr}(i,j) - p0(i,j) - p1(i,j)/\sqrt{Q(i,j)}\ .$$

Investigating other possible sources of systematic effects, a dependence of $t_{crystal}$ on the waveform rise time was identified. Figure 4.20 shows the correlation between the rise time and the reconstructed charge. To reduce the impact of the

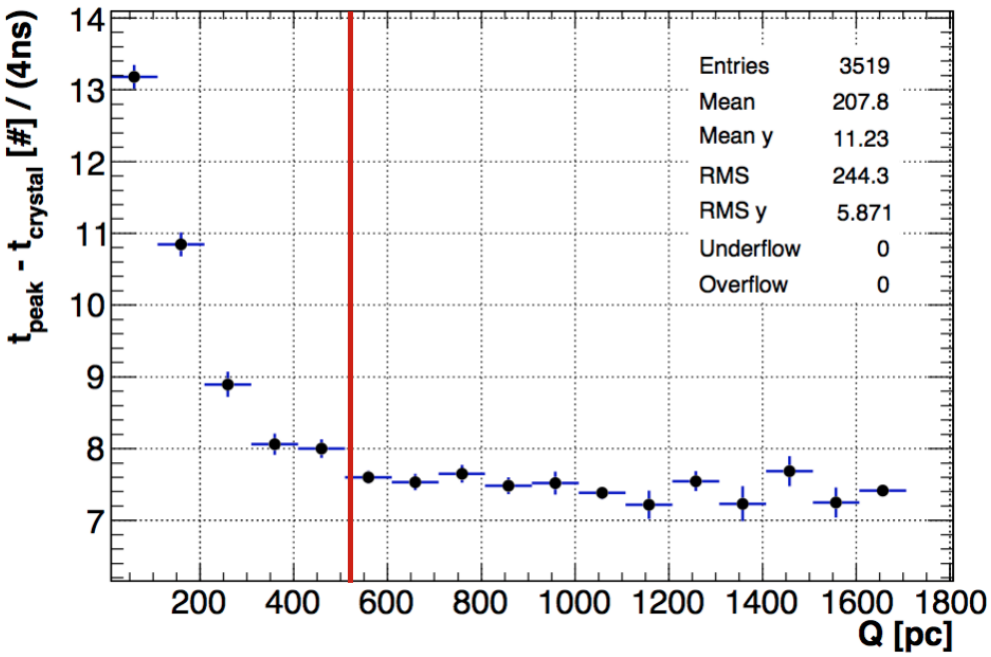

Figure 4.20: Pulse rise time versus reconstructed charge. t_{peak} is the pulse peak time, derived from the log-normal fit. The red line indicates the 10 MeV equivalent threshold.

changing pulse shape on the reconstructed times, a threshold at 10 MeV was made on the crystal signals used for the time resolution studies.

4.5 Measurement of the time resolution

The time resolution has been measured using three different techniques:

1. using only the crystal with the largest energy deposition;
2. using the energy-weighted mean time of all crystals in the matrix:

$$t = \sum_{i,j} (t_{crystal(i,j)} \cdot E_{i,j})/E_{tot}, \qquad E_{tot} = \sum_{i,j} E_{i,j}$$

3. using two neighboring crystals with similar energy deposition.

The first two techniques require an external time reference t_{scint}. No reference is needed for the third one. Methods 1 and 2 were used with both beam configurations: at 0 deg and 50 deg. Method 3 was used only on the runs with the beam at 50 deg.

4.5.1 Beam incidence at 0 deg

The configuration at 0 deg represents the simplest one from the point of view of the analysis, providing an helpful handle for the development of the time reconstruction method. However it has been noted that the expected average CE incidence angle is quite different - about 50 deg, as shown in Figure 4.21.

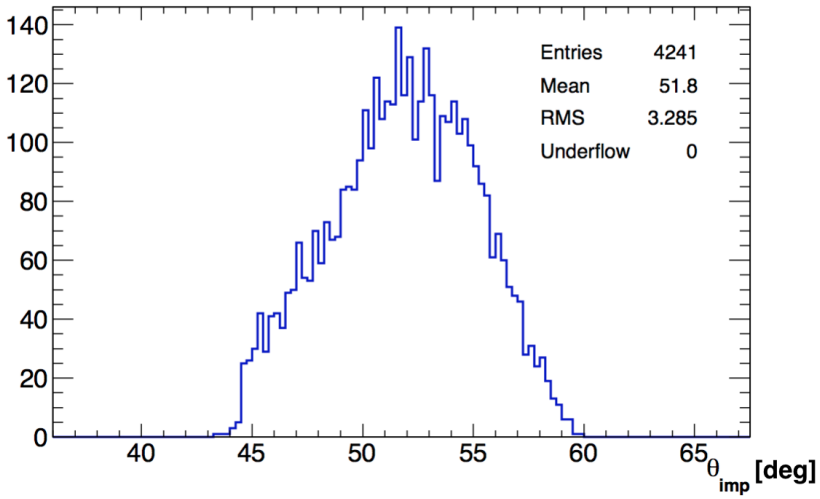

Figure 4.21: Distribution in impact angle θ_{imp} on the calorimeter for reconstructed CE tracks in the Mu2e experiment.

The time resolution (σ_t) has been measured for the beam energies in the range [80, 120] MeV, with 10 MeV step and the beam focused in the center of the crystal (1, 1). Figure 4.22 shows the time resolution resulting from Method 1 as a function of the energy deposited in the crystal with the t_{scint} jitter (about 100 ps) subtracted in quadrature. The time resolution ranges from 130 ps at 46 MeV, to 110 ps at 69 MeV.

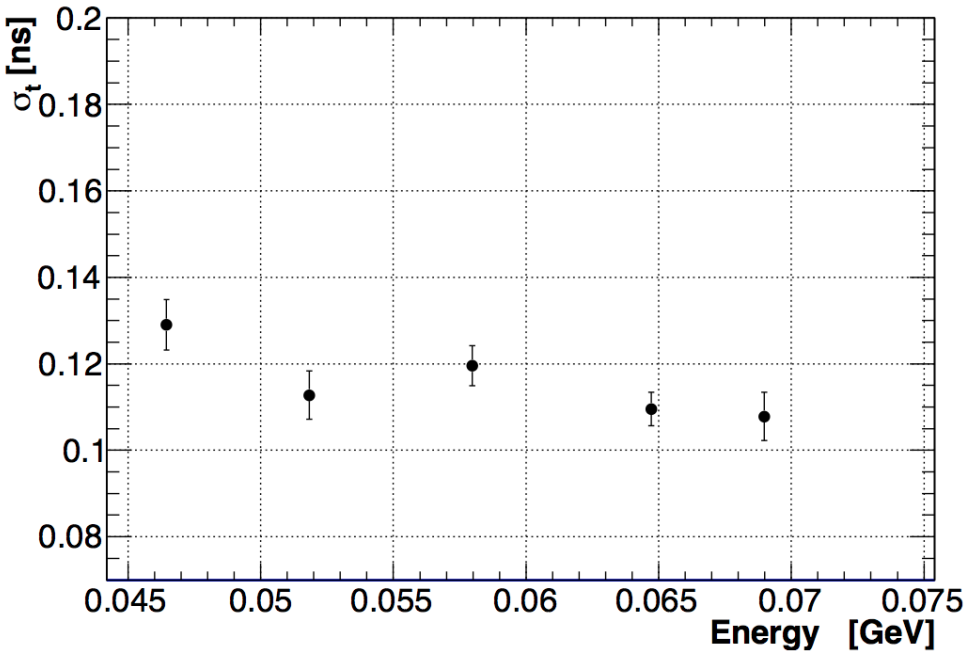

Figure 4.22: Time resolution using the most energetic crystal versus the mean energy deposited in the crystal with the t_{scint} jitter subtracted in quadrature.

Figure 4.23 shows the time resolution determined with Method 2 as a function of the mean cluster energy. Figure 4.24-left shows the mean number of crystals used in the Method 2, as a function of the beam energy. As an example, Figure 4.24-right shows the distribution in number of crystals above 10 MeV for the run at 100 MeV. With the beam at 0 deg, the second method, in most of the cases, uses only one or two crystals.

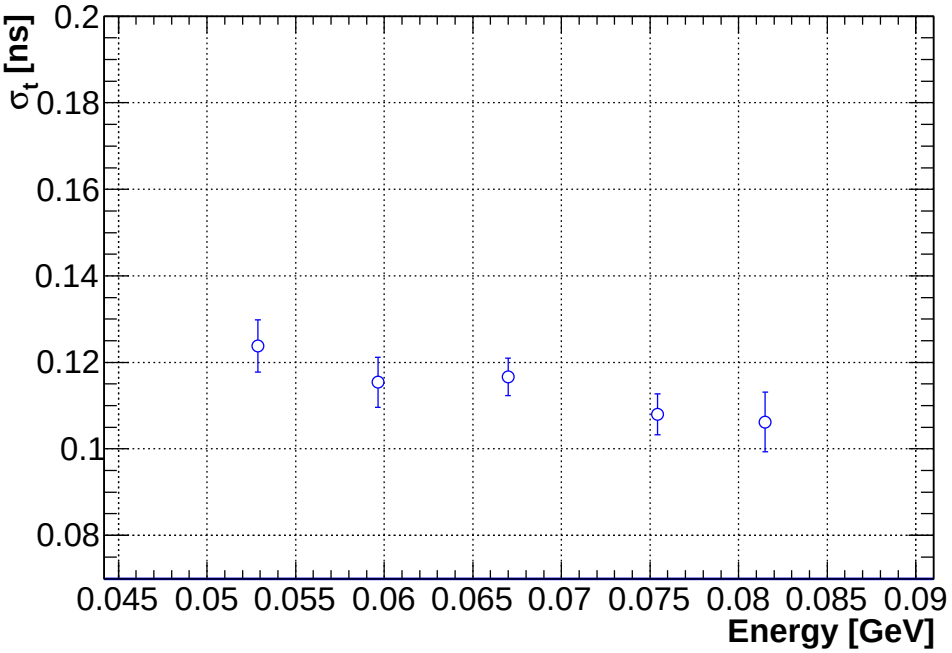

Figure 4.23: Time resolution using the energy weighted mean versus the mean cluster energy with the t_{scint} jitter subtracted in quadrature.

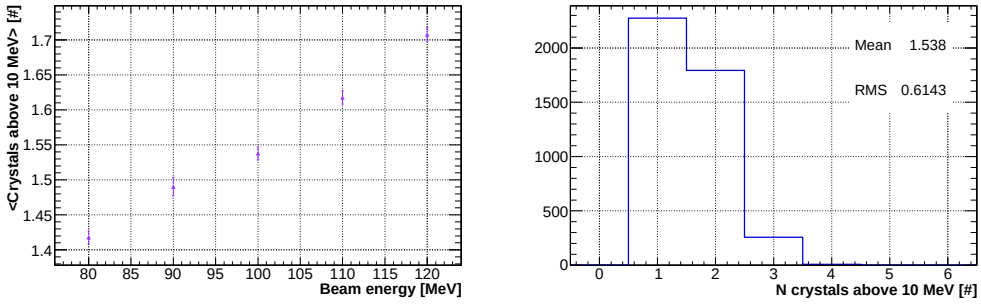

Figure 4.24: Left: mean number of crystals above 10 MeV versus the beam energy. Right: occupancy distribution, with a threshold at 10 MeV, in the run with beam energy at 100 MeV.

4.5.2 Beam incidence at 50 deg

With the prototype rotated by 50 deg, data was taken in three different beam impact points, as shown in Figure 4.25:

1 on the edge of the crystal (1, 0);

2 7.7 mm from the edge;

3 15.4 mm from the edge.

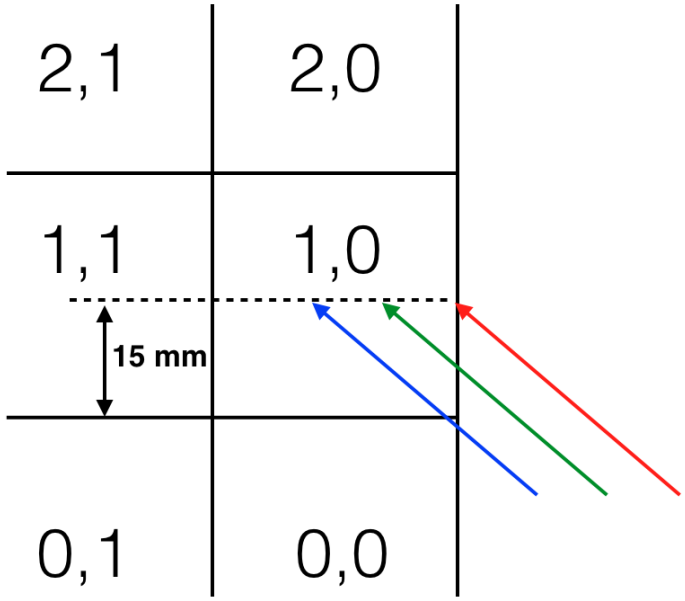

Figure 4.25: Impinging beam positions used in the run with the beam at 50 deg incidence angle. Distance between the impinging points is of about 7.7 mm.

Figure 4.26 shows the time resolution resulting from Method 1 measured in the three runs, with the t_{scint} jitter subtracted in quadrature. Subtracting the t_{scint} jitter, the time resolution is of about 160 ps. Measurements at different beam positions are consistent within 10-15 ps.

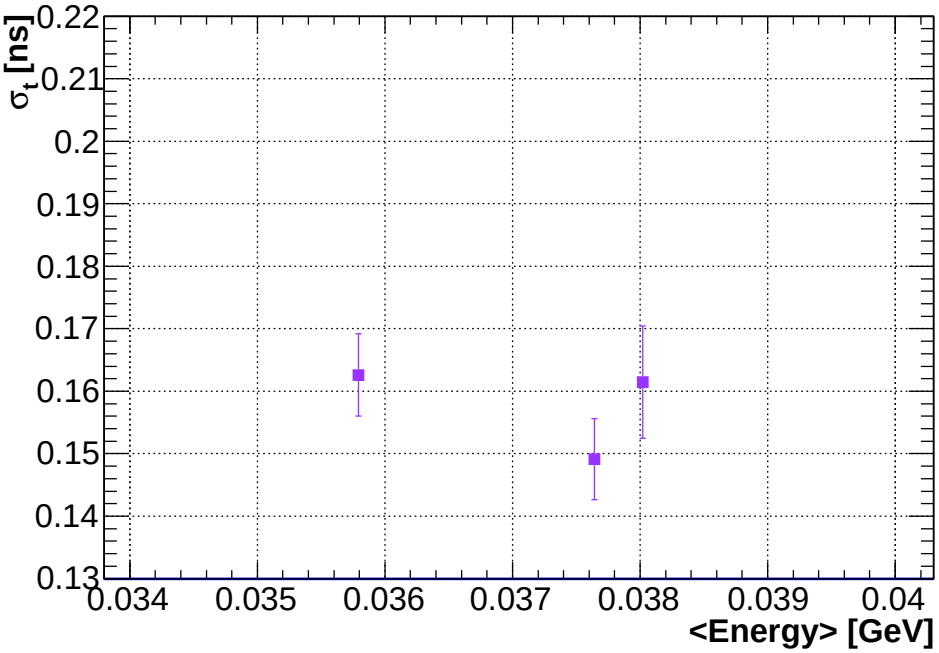

Figure 4.26: Time resolution using the most energetic crystal versus the mean energy deposited in the crystal with the t_{scint} jitter subtracted in quadrature.

Figure 4.27 shows the time resolution resulting from Method 2. The mean cluster energy is close to 60 MeV, and the resulting time resolution is of about 140 ps.

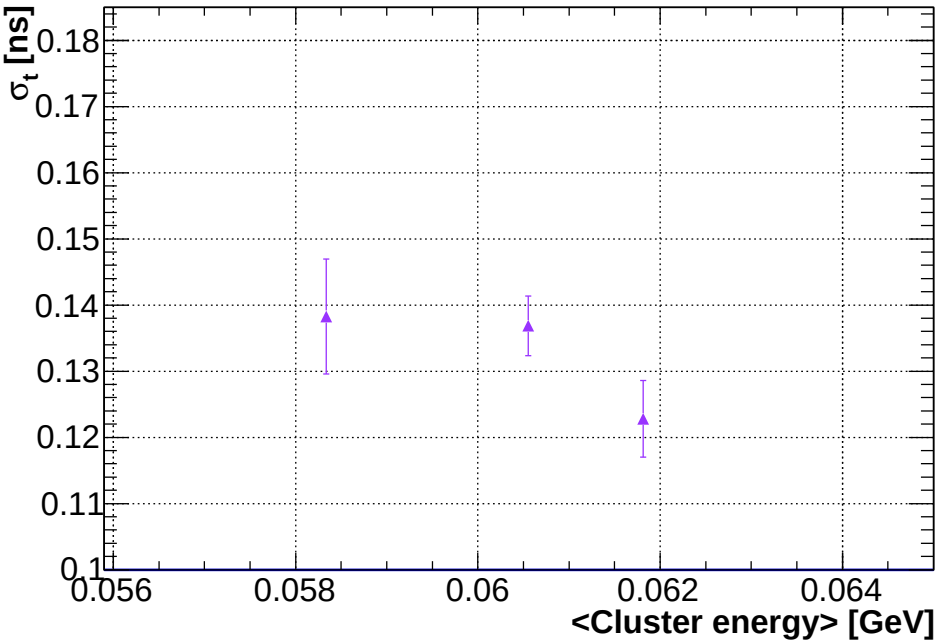

Figure 4.27: Time resolution using the energy weighted mean versus the mean cluster energy with the t_{scint} jitter subtracted in quadrature.

Figure 4.28 shows the distribution in number of crystals above 10 MeV for the configuration with the beam focused on the edge of the prototype (red arrow on Figure 4.25).

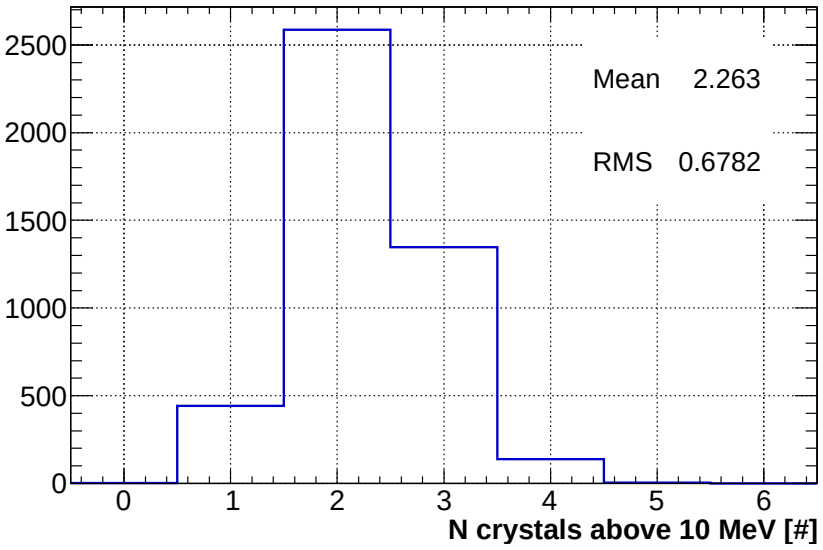

Figure 4.28: Distribution in number of crystals with energy above 10 MeV for the run with 100 MeV beam impinging in the prototype edge.

All data taken with the tilted configuration were combined to apply Method 3, and crystals (1, 1) and (1, 0) were used. Figure 4.29 shows the distribution in the reconstructed energy ratio between the two selected crystals.

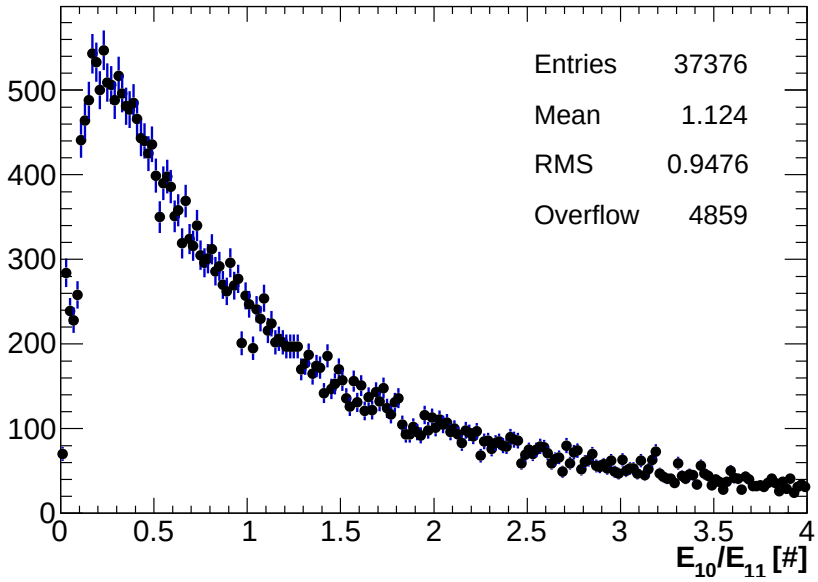

Figure 4.29: Distribution in reconstructed energy ratio between crystals (1,0) and (1,1).

To select the events, their energy ratio $E_{1,1}/E_{1,0}$ was required to be: $0.8 < E_{1,1}/E_{1,0} < 1.2$. Figure 4.30 shows the distribution in time residuals between $t_{crystal(1,1)}$ and $t_{crystal(1,0)}$. The sigma resulting from a Gaussian fit to the distribution is 282 ps. So, assuming the time resolutions of the two channels are the same, the single channel time resolution is $\sigma_t = 283/\sqrt{2} = 200$ ps.

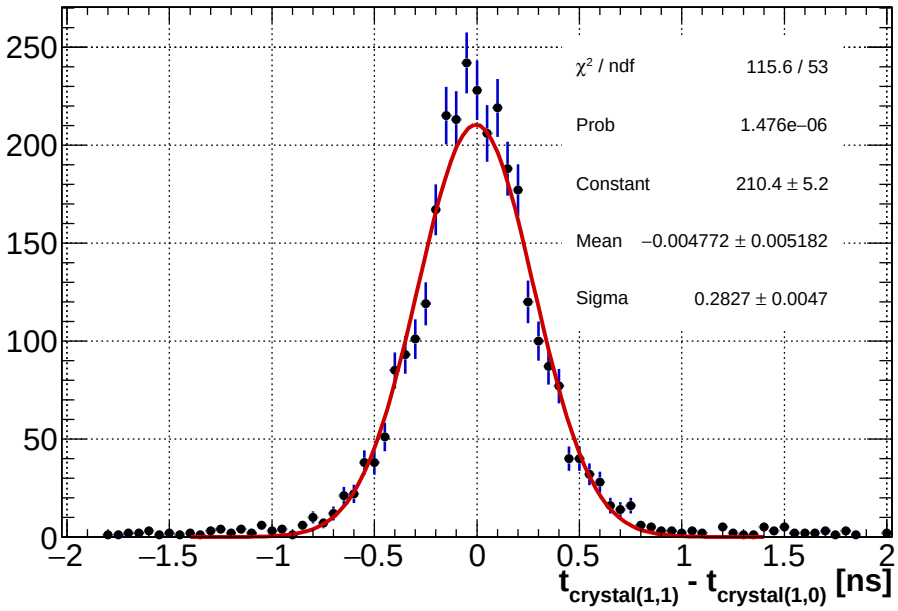

Figure 4.30: Time residuals between channels (1, 0) and (1, 1).

One can expect the resolution measured with this technique to vary as a function of the energy ratio cut. Figure 4.31 shows the dependence of the time resolution with respect to both: the energy ratio cut, and the mean energy deposited in the crystal (1, 1) for each selection. Results shown in Figure 4.31 includes a systematic error evaluated varying the fit range of the Gaussian fit used to derive the time resolution. The result reflects the physics expectation; as the cut in the energy ratio gets loose, the time resolution deteriorates because of the contribution of the lower energy crystal.

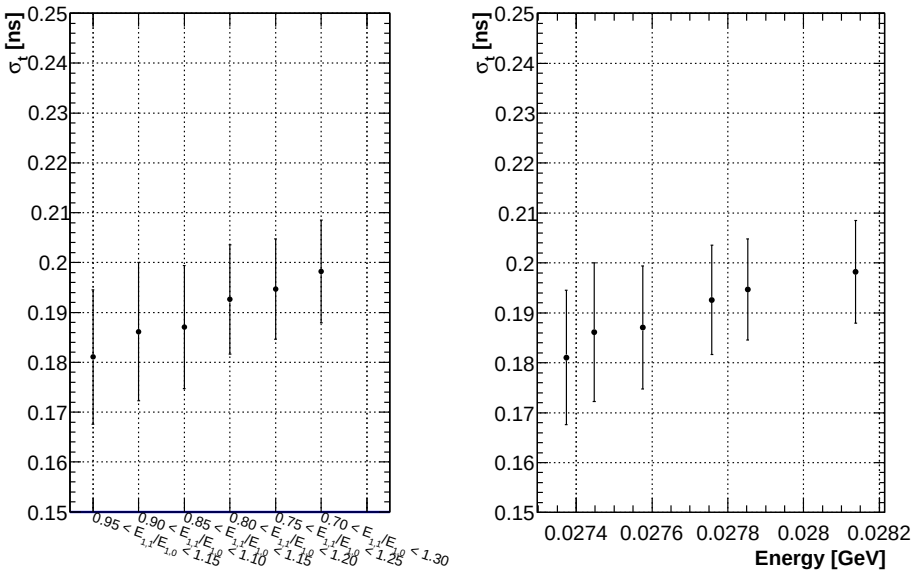

Figure 4.31: Left: time resolution as a function of the charge ratio cut. Right: mean energy deposited in the central crystal as a function of the charge ratio cut.

To cross check the result obtained with this technique, Method 1 has been used to measure the time resolution for the same events. Figure 4.32 shows the time residual between $t_{crystal(1,1)}$ and t_{scint}. Subtracting in quadrature the t_{scint} jitter results in a time resolution of about 200 ps, which is compatible with the result from Method 3.

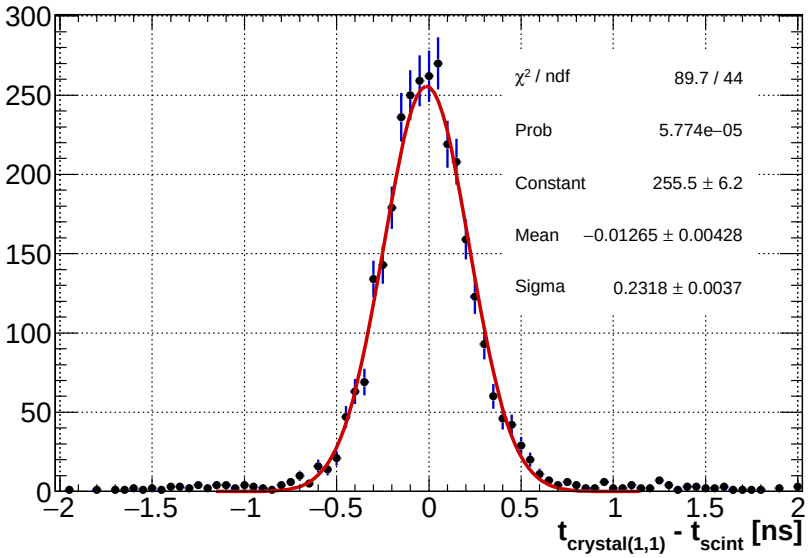

Figure 4.32: Time residuals between $t_{crystal(1,1)}$ and t_{scint}.

4.5.3 Cosmic rays

As Minimum-Ionizing Particles (MIP) crossing 3 cm of CsI crystal, on average, deposit about 20 MeV of energy, cosmic muons allow to measure the time resolution at fairly low energies. Only events where the cosmic ray was crossing the central column of the prototype have been selected, and the "neighboring crystals" technique was used to measure the time resolution. This procedure, however, includes an additional fluctuation due to the jitter in the path length of the muons crossing multiple crystals at different angles.

The cosmic event selection requires a reconstructed energy above 5 MeV for each of the crystals in the central column, and less than 5 MeV of deposited energy for each of the other 6 crystals. Figure 4.33 shows the energy distribution of all crystals after the selection.

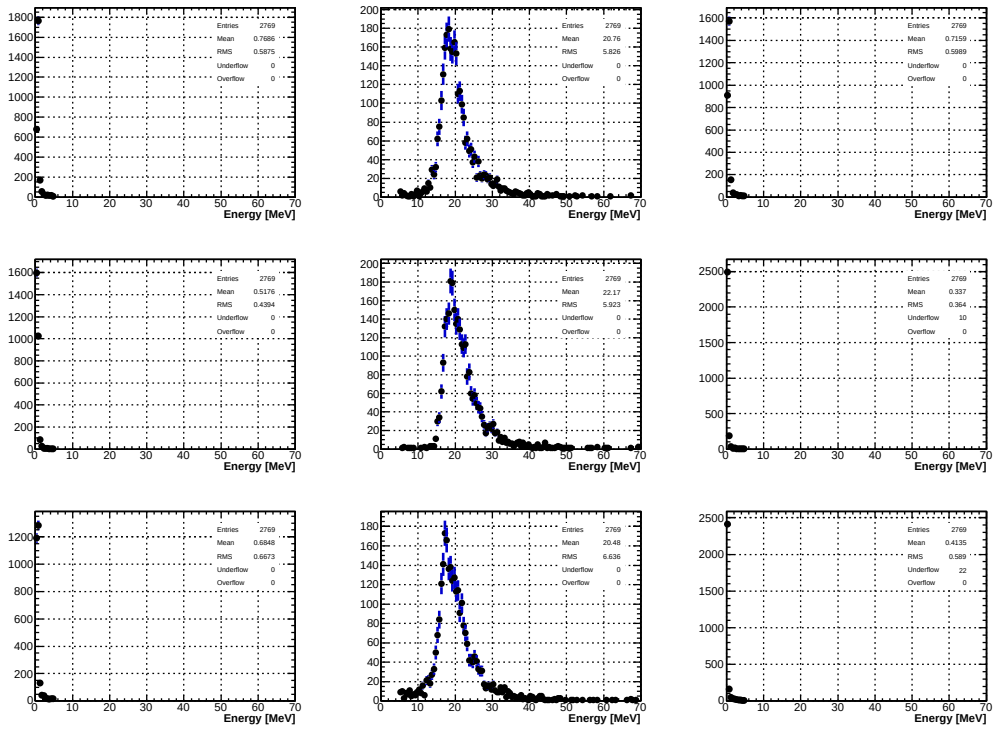

Figure 4.33: Energy distributions in crystals of the prototype for events passing the cosmic selection. Distributions are arranged as described in Figure 4.4

The energy response of the calorimeter prototype to the MIP has been compared with the Monte Carlo. Figure 4.34 and Figure 4.35 show respectively the energy distributions for crystals in the central column and the distribution in the total energy deposited in the central column for data overlaid with the Monte Carlo. Both figures show a good agreement between data and Monte Carlo.

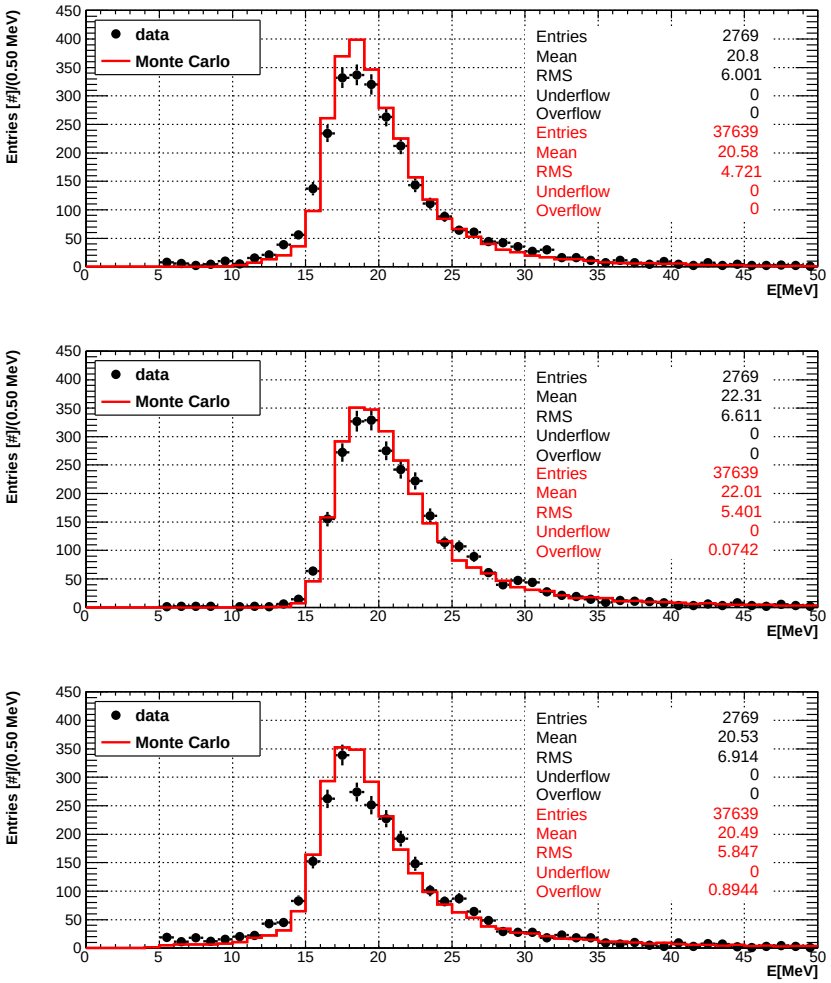

Figure 4.34: Energy distributions for the crystals in the central column overlaid with the Monte Carlo, after the column selection has been made.

With a total of three crystals in the central column, there are two independent pairs of neighboring crystals – (2, 1)-(1, 1) and (1, 1)-(0, 1) – that were used to measure the time resolution with Method 3. Figure 4.36 shows the time residuals for the two pairs. The time resolution has been quoted using the average of the sigma resulting from the fit of the two previous residuals distribution to a Gaussian, and assuming the resolution in all channels to be the same: $\sigma_t \sim 250$ ps.

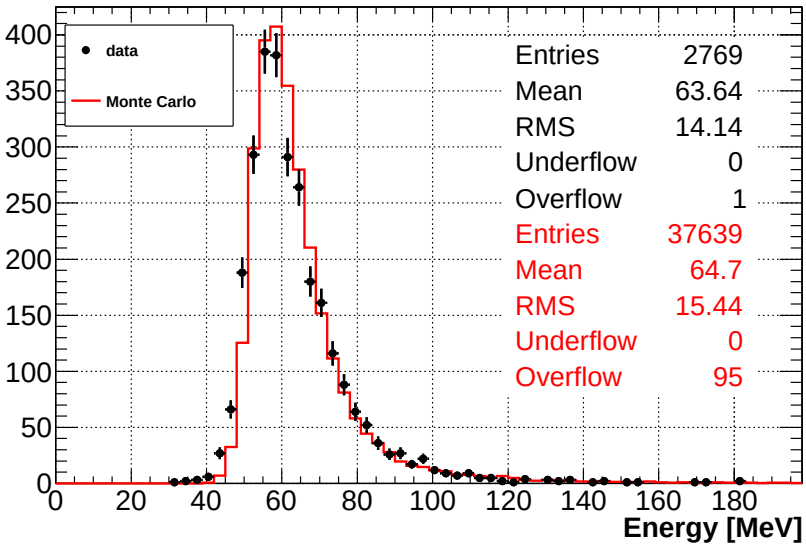

Figure 4.35: Sum of the reconstructed crystal energies in the central column, after the column selection has been made.

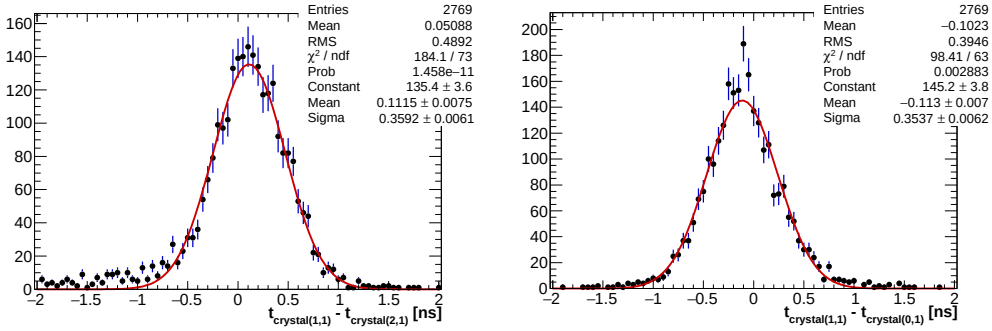

Figure 4.36: Distributions in time residuals between crystals (1,1) and (2,1) (left) and crystals (1,1) and (0,1) (right).

Discussion of the results

Three different techniques have been used to determine the time resolution of the undoped CsI calorimeter prototype in different geometrical configurations. All results plotted versus energy are shown in Figure 4.37.

The first observation is that the time resolution measured using Method 3 (red markers) is compatible with the measurement resulting from Method 1 on the same sample (open triangles).

Furthermore, in the same energy range, the time resolution using Method 2 is slightly worse when the beam impacts at 50 deg (violet triangles). Fluctuations

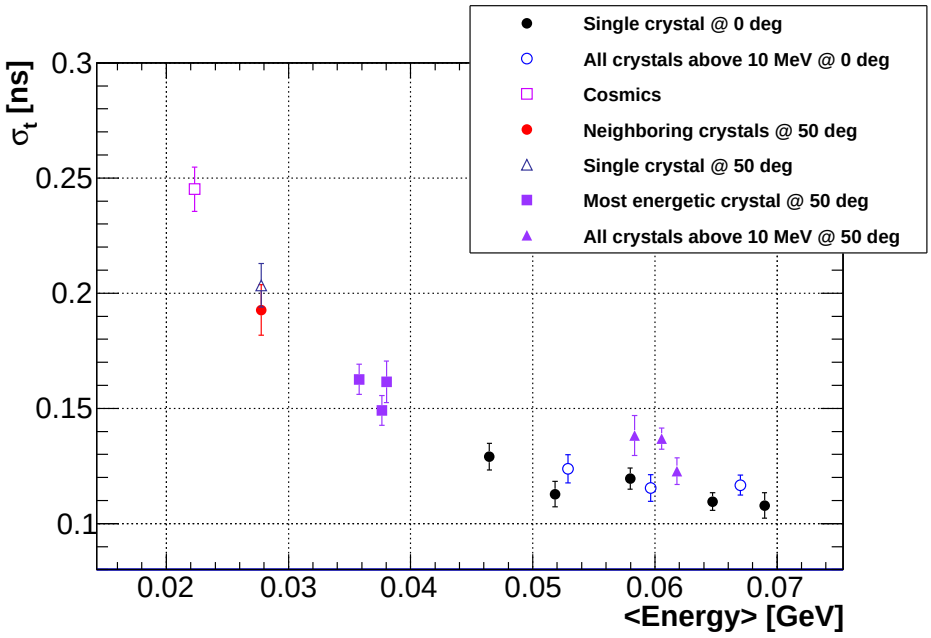

Figure 4.37: Time resolution summary plot.

of the shower development could result in additional time jitter between the signals from different crystals, and might be, partially responsible for this discrepancy.

4.5.4 Time resolution without using time walk corrections

The results discussed in the previous paragraphs used the time walk corrections. In order to quantify importance of these corrections, in Figure 4.38 the time resolutions determined using Method 1, with and without the time walk corrections, are compared. For the case with the beam incidence angle of 50 deg, ignoring the

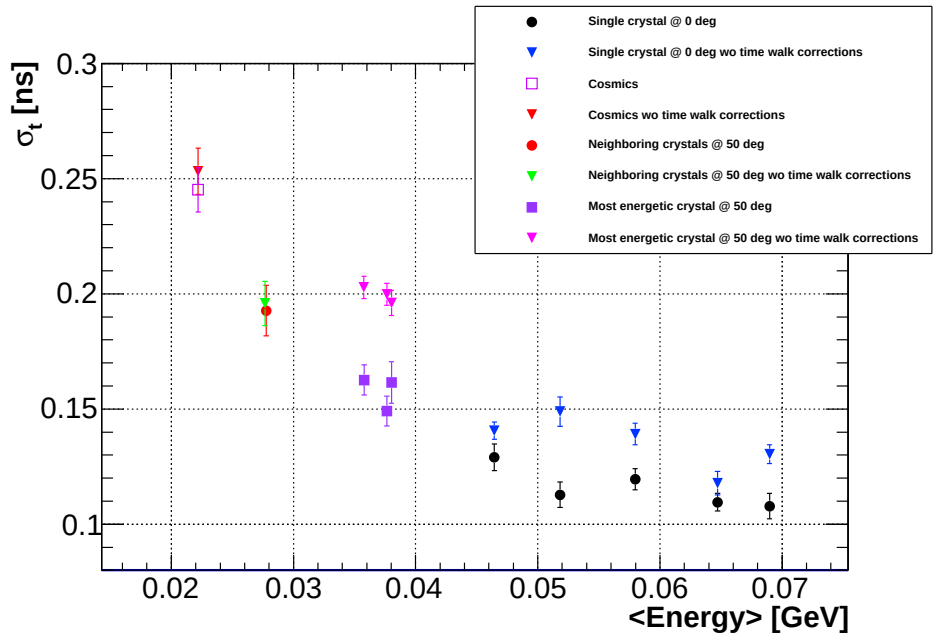

Figure 4.38: Time resolution from Method 1 with and without time walk corrections.

time walk corrections adds a term $\sigma_{\text{walk}} \simeq 120$ ps in quadrature to the time resolution . As for $\mu^-\text{N} \rightarrow e^-\text{N}$ conversion electrons the mean angle of incidence in the calorimeter is 50 deg, even without the time walk corrections, one can expect the time resolution for 100 MeV electrons to be close to the measured $\sigma_t = 200$ ps.

4.6 Measurement of the energy resolution

The tested calorimeter prototype has dimension of $9 \times 9 \times 20$ cm^3 that, in "natural shower units", corresponds to $\sim$ (1.3 $R_{Moliere}$)$^2 \times$ $\sim$ 10 X_o. Due to the small dimensions, the transverse and longitudinal leakages impact significantly in the energy response. The primary goal of the energy resolution measurement is therefore not to establish the absolute number - for a large prototype it should be better, but to provide a comparison between data and Monte Carlo. Energy resolution has been measured for both 0 and 50 deg beam incidence angles.

4.6.1 Beam incidence at 0 deg

The prototype energy response has been studied using the electron beam in the energy range of [80, 120] MeV with 10 MeV steps. Figure 4.39 shows the distribution in the total energy deposition obtained from data compared with the Monte Carlo. Figure 4.40 shows the measured energy resolution as a function of the total energy reconstructed in the prototype, with the simulation results superimposed. Within the uncertainties, data and Monte Carlo distributions are in agreement. The measured energy resolution varies from 7.4% to 6.5% in the energy range [70, 102] MeV.

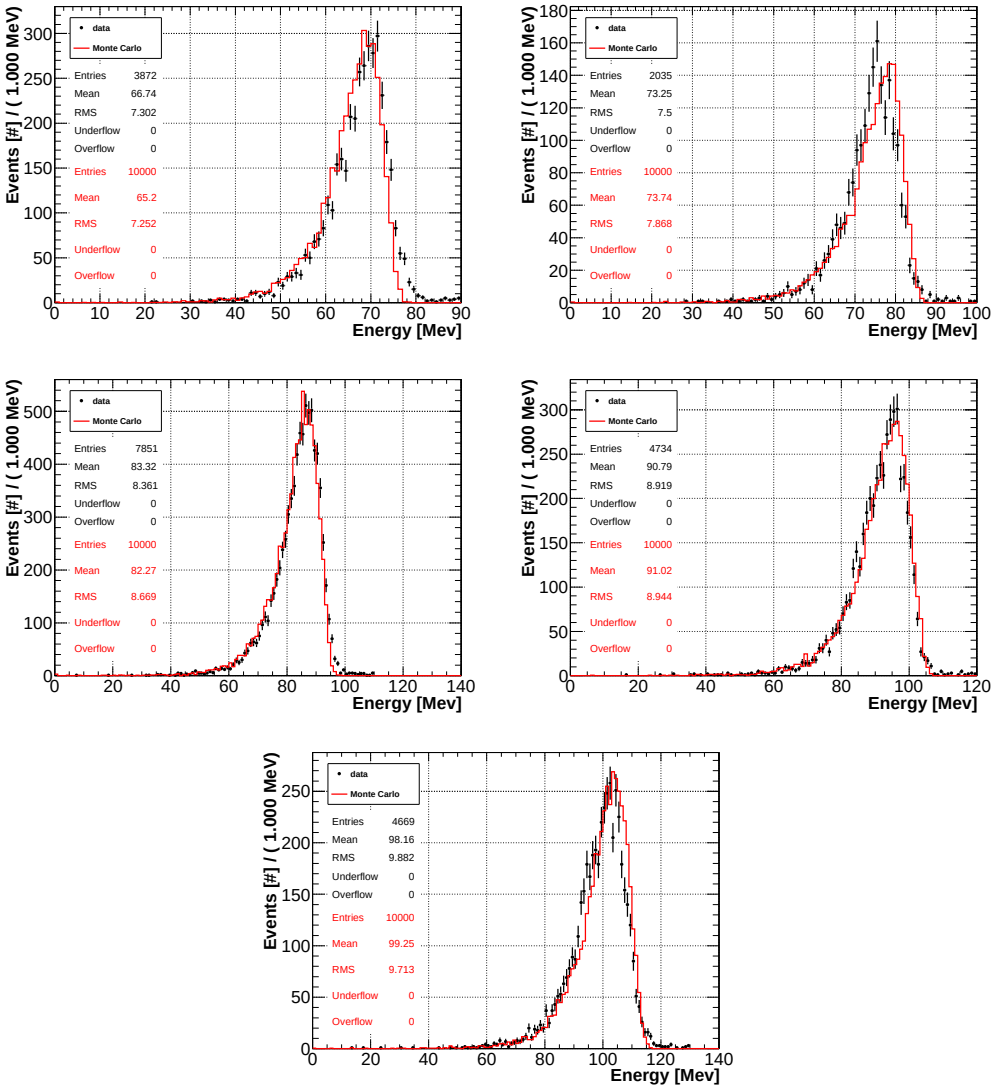

Figure 4.39: Distribution in energy obtained from the data from data overlaid with the Monte Carlo for the following beam energies: 80 (top-left), 90 (top-right), 100 (middle-left), 110 (middle-right) and 120 (bottom) MeV.

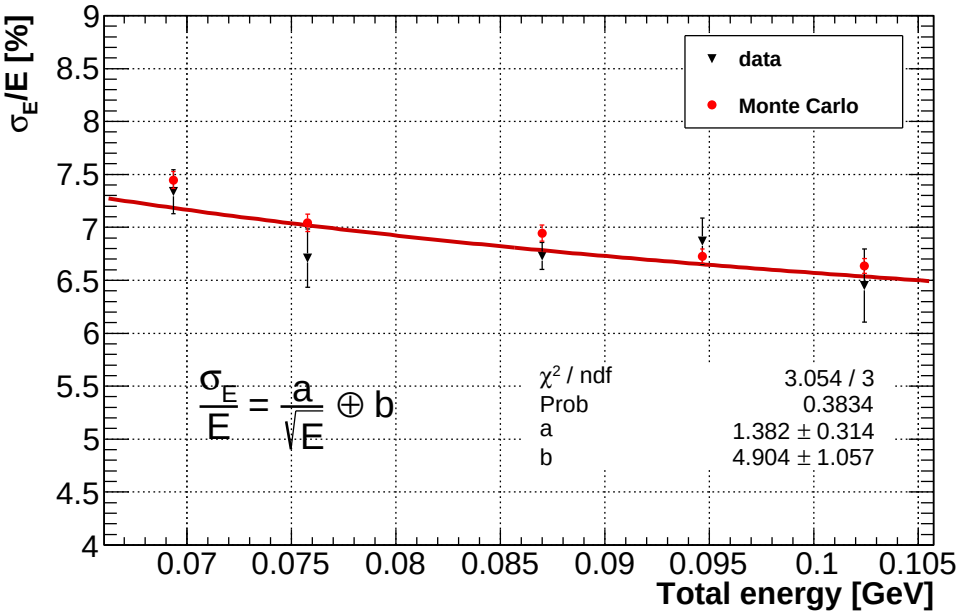

Figure 4.40: Energy resolution obtained from the data (black) compared with the Monte Carlo (red).

4.6.2 Beam incidence at 50 deg

For the data taken at 50 deg beam incident angle, the energy response of each individual crystal has been compared to the Monte Carlo simulation. As an example, Figure 4.41 shows the comparison between data and Monte Carlo for the configuration with the beam focused on the prototype edge (red arrow on Figure 4.25). Distributions in the central row of the same figure show a discrepancy at a level below 15%. Potential sources of this discrepancy could be different Moliére radius in the Monte Carlo.

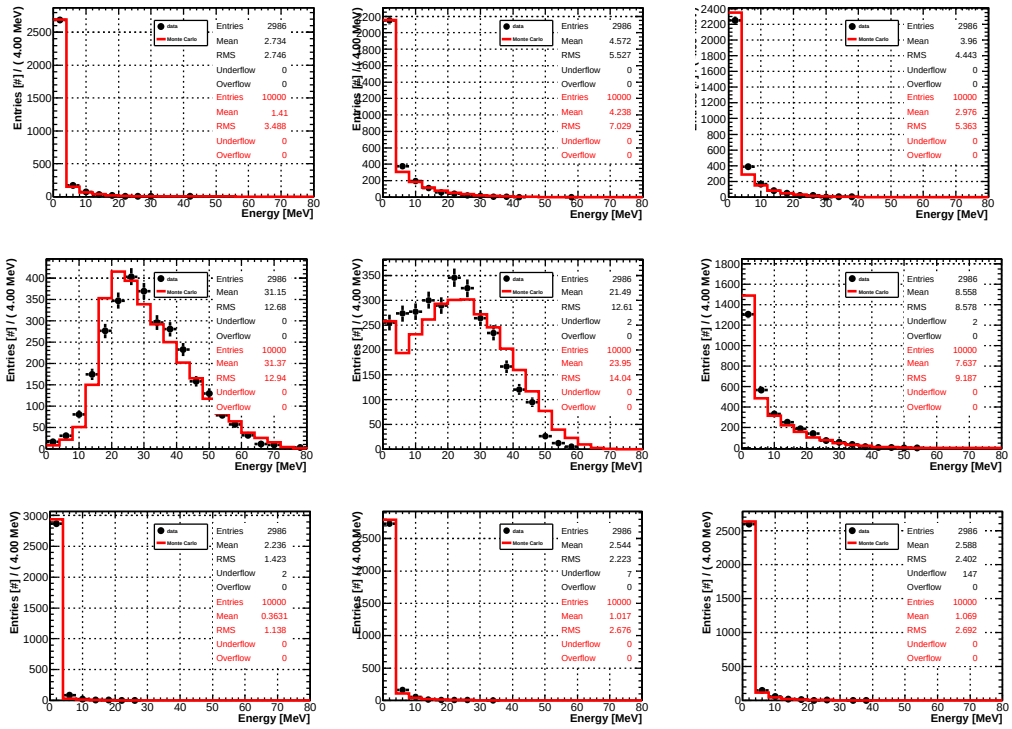

Figure 4.41: Energy response of each crystal from data (black) overlaid with the Monte Carlo (red) for the runs with 100 MeV electrons at 50 deg impinging on the external side of crystal (1,0).

Summary

The time resolution and the energy response of the CsI prototype have been studied, using electron beam in the energy range [80, 120] MeV, and cosmic rays. The time resolution $\sigma_T = 130$ ps has been measured with the beam impinging at 50 deg, which is close to the mean incidence angle in the calorimeter, expected for $\mu^-\mathrm{N} \rightarrow e^-\mathrm{N}$ conversion electron. Even without using the time-walk corrections, the resolution is better than 200 ps.

The small size of the prototype did not allow to measure the energy resolution in a configuration similar to the Mu2e case, but still the comparison with the Monte Carlo represented an important test for the Monte Carlo simulation.

Chapter 5

Calorimeter driven pattern recognition

Introduction

The Mu2e track reconstruction has several specific features. First, a CE (p $\sim$ 105 MeV/c) makes 2-3 full turns moving inside the tracker, so a track consisting of several loops has to be reconstructed. This topology is very different from the typical tracks reconstructed in most HEP experiments, where "extra" loops are often discarded. In addition, as the muon nuclear capture or a muon decay happen at an unspecified time, the electron production time is also unknown. It is easy to show that the reconstructed track parameters depend on the particle timing. Let's call T_0 the time when the particle crossed the middle of the tracker. The T_0 is used as input to determine the drift radii of the straw hits. Wrong calculation of the drift radii or mis-assignment of the drift directions impacts the reconstruction performance. For each track hit, T_0 explicitly enters the calculation of the hit drift radius r_{drift}:

$$r_{\text{drift}} = v_{\text{drift}} \cdot (t_{\text{measured}} - T_0 - t_{\text{flight}}) \, ,$$

where v_{drift} is the drift velocity, and t_{flight} is the particle's time of flight from the middle of the tracker to the corresponding straw. So the track hit coordinates depend on T_0, and T_0 becomes an additional parameter to be determined from the fit.

The Mu2e track reconstruction proceeds in two main steps: first a track search

provides a pattern of straw hits consistent with a track candidate, then a Kalman-based track fitter performs the final reconstruction. The track finding uses two algorithms: a standalone algorithm, and a calorimeter-driven algorithm. The standalone algorithm relies only on the tracker information to perform an helix search [1, 59]. The calorimeter-seeded track search [60] is a specialized algorithm, optimized to search for electron tracks generated in the stopping target that produced clusters in the calorimeter. The algorithm uses the reconstructed time and position of the calorimeter cluster to search for a track pointing to that cluster. This procedure improves the track search and makes the global track reconstruction more efficient and robust with respect to the expected background level. In the next sections the calorimeter-seeded pattern recognition is presented.

5.1 Algorithm description

The pattern recognition finds an electron track candidate - a set of hits consistent with a particle trajectory. With an accuracy of few %, the magnetic field can be considered uniform in the tracker region, so the trajectory is well parametrized with a helix. In addition, the pattern recognition determines the helix parameters that are used by the track fitter as input. The algorithm searches for CEs (E ∼100 MeV), so only calorimeter clusters with $E_{cluster} > 60$ MeV are used to seed the track search. The chosen energy threshold is a compromise between the acceptance and the performance: ∼ 93% of CEs that traverse the tracker have $E_{cluster} > 60$ MeV, and the average number of background clusters per event above that threshold is about 2.44. Figure 5.1 shows that using this threshold the number of reconstructed clusters per event is reduced by a factor ∼ 17. For each selected cluster a track search is performed. The pattern recognition starts performing first a straw hits pre-selection, and then a helix search.

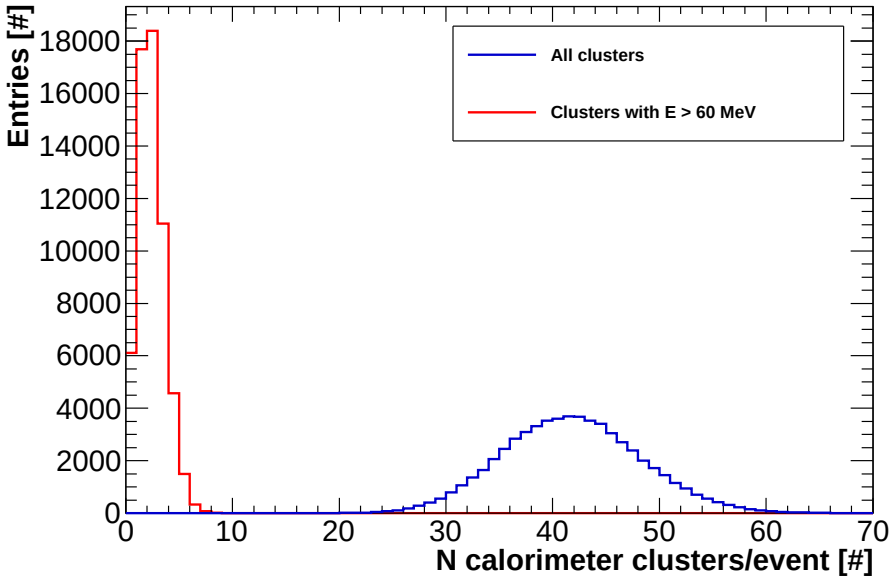

Figure 5.1: Distribution in number of reconstructed clusters per event with (red line) and without (blue line) the E > 60 MeV cut.

5.1.1 Straw hits pre-selection

The majority of hits in the tracker are due to the background, so a hits pre-selection is used to improve the S/N before starting the real search for CE track. Hits produced by the same particle in different detectors are correlated in time. This correlation is illustrated in Figure 5.2, where the red histogram shows the distribution in time residuals $\Delta t = t_{cluster} - t_{straw\ hit}$ between the reconstructed cluster time ($t_{cluster}$) and straw hit time ($t_{straw\ hit}$) for simulated CE-only events. The distribution is contained within the window of 60 ns, determined by the maximal drift time and the particle time of flight in the detector. The blue histogram in Figure 5.2 shows the Δt distribution for CE events simulated including the expected background. The shift of the peak with respect to $\Delta t = 0$ ns is due to the following reasons:

- the average time-of-flight of a CE from the middle of the tracker to the calorimeter is $\sim$ 8 ns;
- the mean value of the drift time in the straws is 20 ns ($v_{drift} = 62.5\ \mu$m/ns).

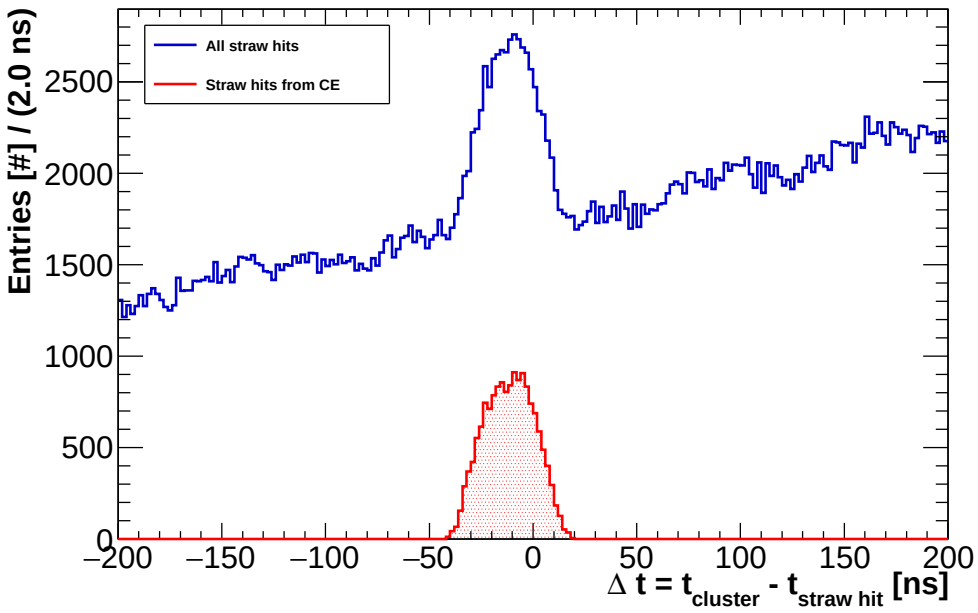

Figure 5.2: Blue line: distribution in Δt for all the straw hits. Red line: same distribution using only straw hits generated by the CE. The distributions are truncated at ±200 ns.

The difference between the two numbers (∼ -12 ns) is consistent with the peak value. The requirement $\Delta t \in [-50, 30]$ ns changes the relative fraction of hits produced by the CE: N(CE)/N(background), from 0.01 to 0.18.

Furthermore, the knowledge of the cluster position allows to improve the background rejection. The graded magnetic field, between the stopping target and the tracker, acts as a lens and focuses the electrons so that CEs within the tracker geometric acceptance have a transverse momentum in the rather narrow range range of 75-86 MeV/c. So in the XY plane, hits produced by a CE are contained within a semicircle centered on the cluster, as illustrated in Figure 5.3. The requirement that the hit azimuthal angle ϕ is contained within $\pi/2$ from the cluster: $|\phi_{\text{hit}} - \phi_{\text{cluster}}| < \pi/2$ reduces the background by an additional factor of two. Figure 5.4 shows how the hits pre-selection reduces the number of background hits in a typical event with one CE overlaid with the expected background. In addition to these requirements, a dedicated multivariate algorithm is used to remove hits produces by δ-electrons. Description of the algorithm can be found in refer-

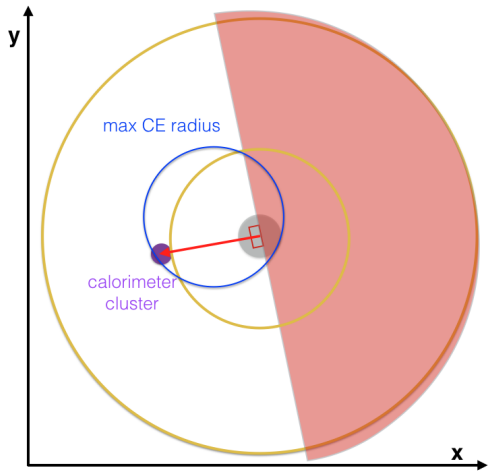

Figure 5.3: Illustration of the calorimeter cluster ϕ selection in the XY plane. Legend: sienna lines limit the tracker volume, the grey bullet is the Al stopping target, magenta bullet is the cluster, and blue circle is the CE trajectory in the transverse plane.

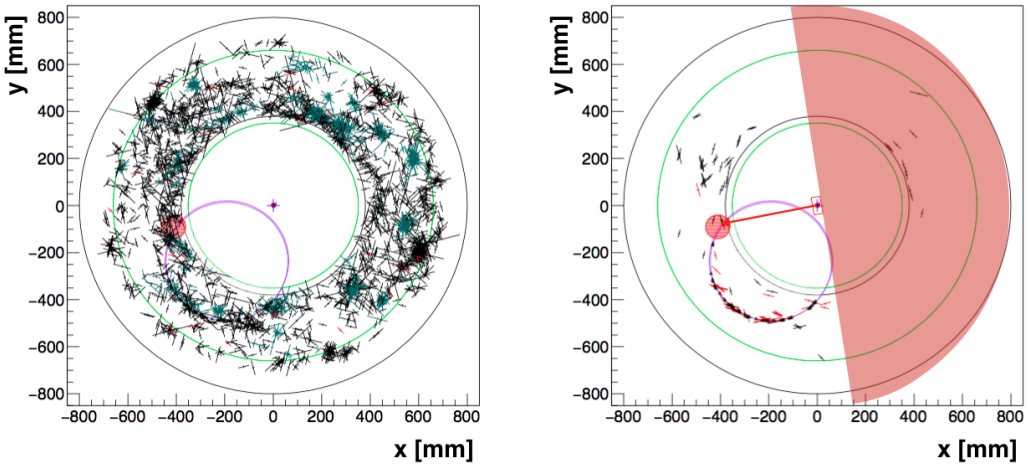

Figure 5.4: Transverse view of an event display for a CE event with background hits included, with (right) and without (left) the calorimeter pre-selection. The black crosses represent the straw hits, the red bullets the calorimeter clusters, and the red circle the CE trajectory.

ence [59].

5.1.2 Helix search

The pattern recognition searches for a set of hits consistent with a helix. The helix parallel to the Z direction is defined by 5 parameters: R - radius of the circle, X_0 and Y_0 - coordinates of the helix center, $d\phi/dz$, and ϕ_0 - the azimuthal angle ϕ at Z=0.

The search starts from three points (a triplet): the center of the stopping target, a straw hit, and the calorimeter cluster. X and Y coordinates of the three points give an initial estimate of R, X_0, and Y_0. As the number of track turns is unknown when the search starts, is not possible to derive unambiguously the value of $d\phi/dz$ ($d\phi/dz = (\Delta\phi + 2\pi n)/dz$), the mean $d\phi/dz$ value expected for the CE is used when the search starts.

The search continues layer by layer moving downstream the first selected straw hit of the triplet. The hit position at a given Z-coordinate is predicted using the helical extrapolation from the last accepted straw hit. The closest hit within the search road is added to the track candidate if:

$$d_{xy} \leq d_0 + d_1 \cdot dz \, ,$$

where d_{xy} is the XY-distance between the straw hit position and the prediction. The value of d_0 is set to 100 mm, approximately 3-4 times the spatial resolution along the wire, dz is the Z-distance from the last straw hit accepted. The value of d_1 is determined by the expression:

$$d_1 = \sigma_{d\phi/dz} \cdot < r_{CE} > \, , \tag{5.1}$$

where $\sigma_{d\phi/dz}$ is the resolution on $d\phi/dz$ during the track search, and $< r_{\mathrm{CE}} >$ is the mean CE radius.

As soon as another straw hit, with coordinates (ϕ, z), is found within $dz \in [10, 50]$ cm from the straw hit of the initial triplet, with coordinates (ϕ_{triplet}, z_{triplet}), the value of $d\phi/dz$ is re-evaluated:

$$d\phi/dz = (\phi - \phi_{\mathrm{triplet}})/dz \, .$$

Figure 5.5 shows the accuracy of the $d\phi/dz$ reconstruction once all straw hits

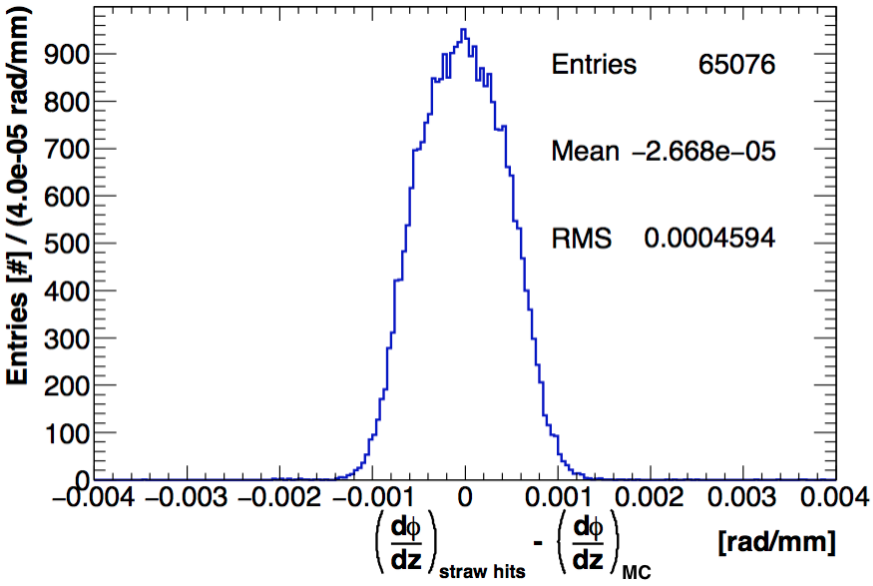

Figure 5.5: Distribution in $d\phi/dz$ residuals: "straw hits" refers to the reconstructed value, and MC to the Monte Carlo truth in the middle of the tracker.

have been scanned, by comparing $d\phi/dz$ with the Monte Carlo value. The width of the distribution defines the value of $\sigma_{d\phi/dz}$ in equation 5.1. Figure 5.6 shows the dependence of d_{xy} on dz.

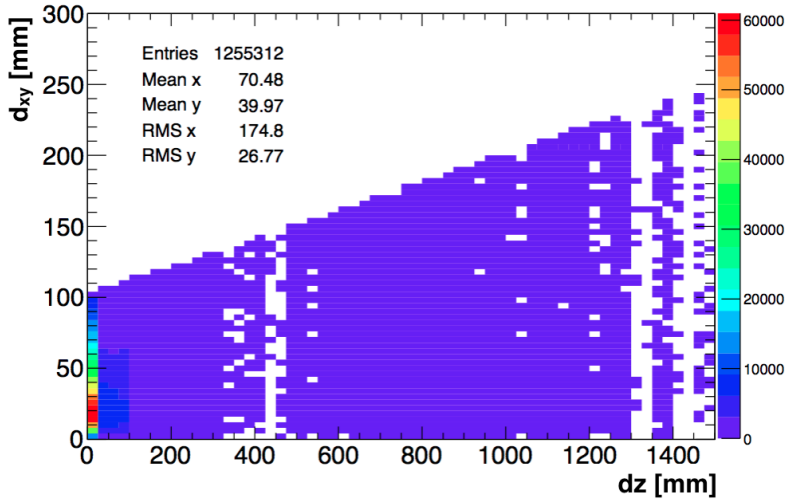

Figure 5.6: Radial distance of the straw hit from the helix prediction versus the distance along the z axis dz of two consecutive straw hits.

As the search progresses, and more straw hits are added to the track candidate, the parameters X_0, Y_0, and R of the helix are updated using a simplified least squares method (LSM) [61]. At this stage of the process, all straw hits used in the fit have equal weights. The resolution on R has been estimated comparing the LSM and the Kalman filter results. Figure 5.7 shows that the resolution on R is of the order of 13 mm. Once the first pass of the hit search is completed, the helix parameters are re-evaluated more accurately. The circle parameters are recalculated analytically using the LSM algorithm, generalized to account for different individual hit weights; assuming the X_0 and Y_0 are known with an accuracy $\sigma_{X,Y} << R$, the hit weights are recalculated individually by projecting the hit errors on the direction connecting the hit with the center of the circle (X_0, Y_0) as illustrated in Figure 5.8. This step is rather important as the hit position uncertainty in the drift direction is better than the resolution along the wire by more than two orders of magnitude.

To determine $d\phi/dz$ and ϕ_0 using all the selected straw hits, one needs to know the number of full turns the particle made in the detector. To obtain this information, in each station $< \phi_i >$ - the mean value of ϕ, is calculated for hits, within the same i-th station, associated with the track candidate. Then all values of $(< \phi_i > - < \phi_j >)/(z_i - z_j)$, evaluated using all combinations of stations (i, j), are collected

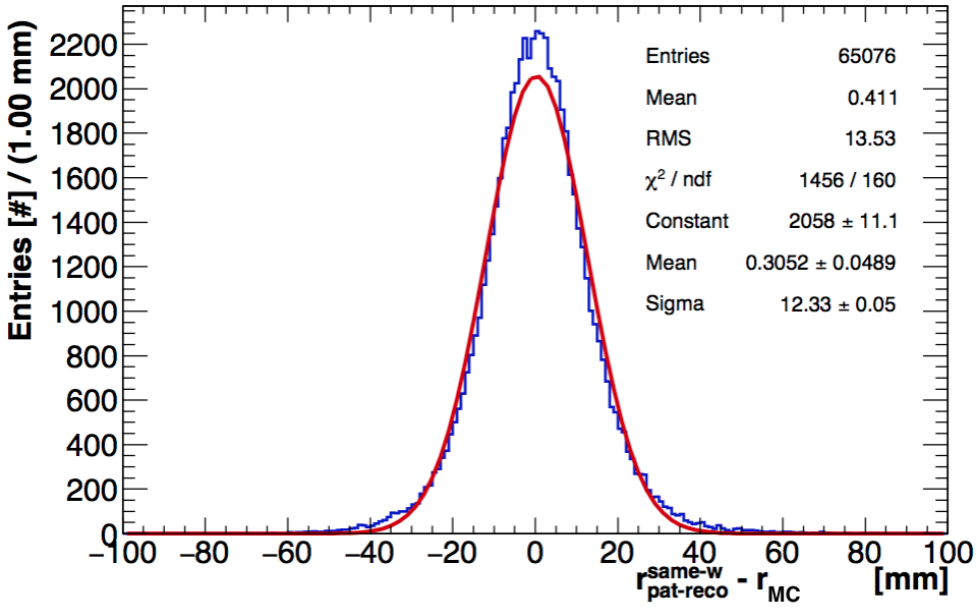

Figure 5.7: Distribution in radius residuals: $r^{same-w}_{pat-rec}$ refers to the LSM result, and MC to the Monte Carlo truth in the middle of the tracker.

in a histogram with a bin-width of $4 \cdot 10^{-4}$ rad/mm. The most probable value of the resulting distribution provides $d\phi/dz$ with sufficient accuracy to determine the number of track turns in the detector. Using this information, ϕ_0 and $d\phi/dz$ are determined from a linear fit of all $< \phi_i >$ corrected for the number of turns. Figure 5.9 shows the resulting resolution in $d\phi/dz$.

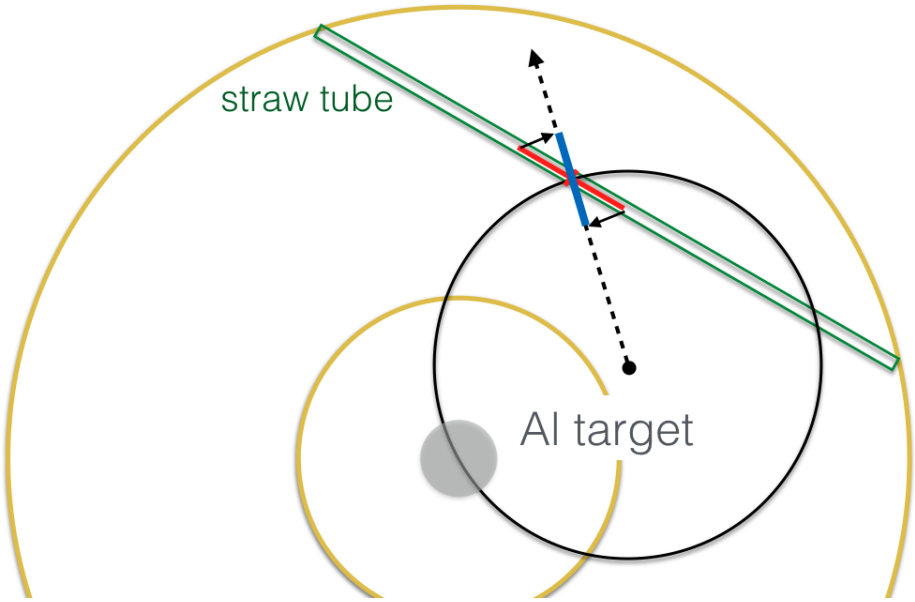

Figure 5.8: Illustration of the hit error projection along the radial direction of the electron trajectory.

At this point, resolution on $d\phi/dz$ is sufficient to determine the ϕ coordinate off all the straw hits, taking into account the number of helix turns. Performing a linear fit on the resulting ϕ allows to improve the resolution on $d\phi/dz$ by $\sim$ 30%, as shown in Figure 5.10.

Then, a search for hits missed by the first pass is performed around the helical trajectory. In case new hits are added, the helix parameters are recalculated using the LSM in XY plane, and the linear fit in Z-ϕ. Figure 5.11 shows results of the X-Y circle fit. The resolution in the helix radius is 8.4 mm that corresponds to $\sim$ 2.5 MeV/c resolution in the transverse momentum. Figure 5.12 shows the fit χ^2 distributions of the circle and the linear fit.

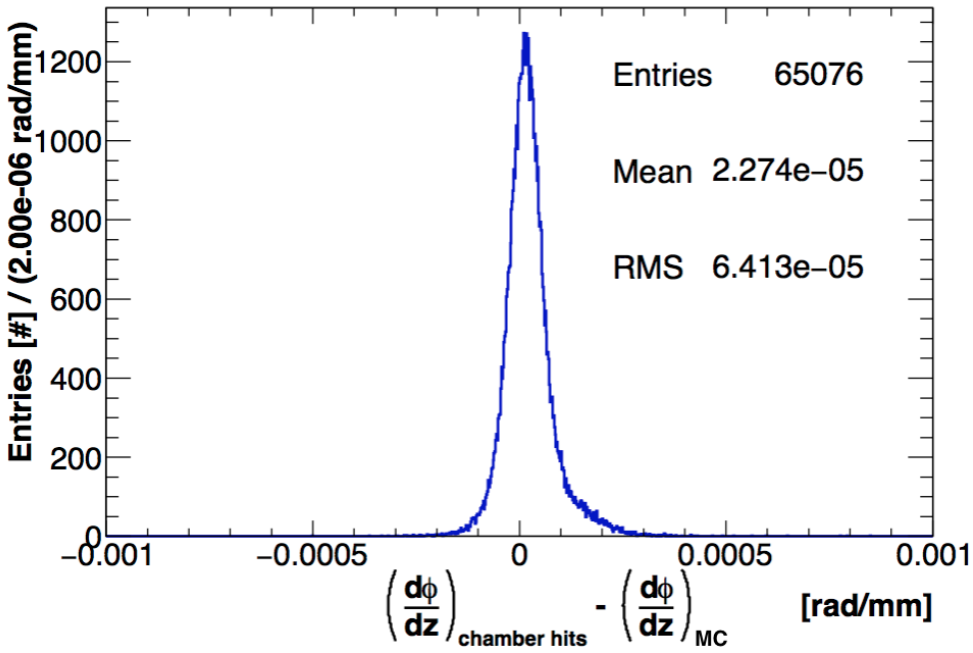

Figure 5.9: Distribution in $d\phi/dz$ residuals: "chamber hits" refers to the results of linear fit of the ($< \phi >$, z) of the station included in the track candidate, and MC to the Monte Carlo truth in the middle of the tracker.

Radius and $d\phi/dz$ reconstruction performance has been studied also including the background hits in the CE simulation, and testing cases with higher background occupancy. Figure 5.13 and 5.14 show respectively that up to 3 times the expected background, the resolution in the reconstructed radius and in $d\phi/dz$, relative to their expected mean values, are improved by 5% and 2%, respectively.

5.2 Pattern recognition efficiency

Performance of the described pattern recognition algorithm has been studied using simulated $\mu^-\text{N} \rightarrow e^-\text{N}$ conversion electrons with:

- at least 25 hits in the tracker with T_{hit} falling into the DAQ trigger time window [500, 1695] ns ($T = 0$ is the time corresponding to the proton beam arrival in the Production Solenoid);

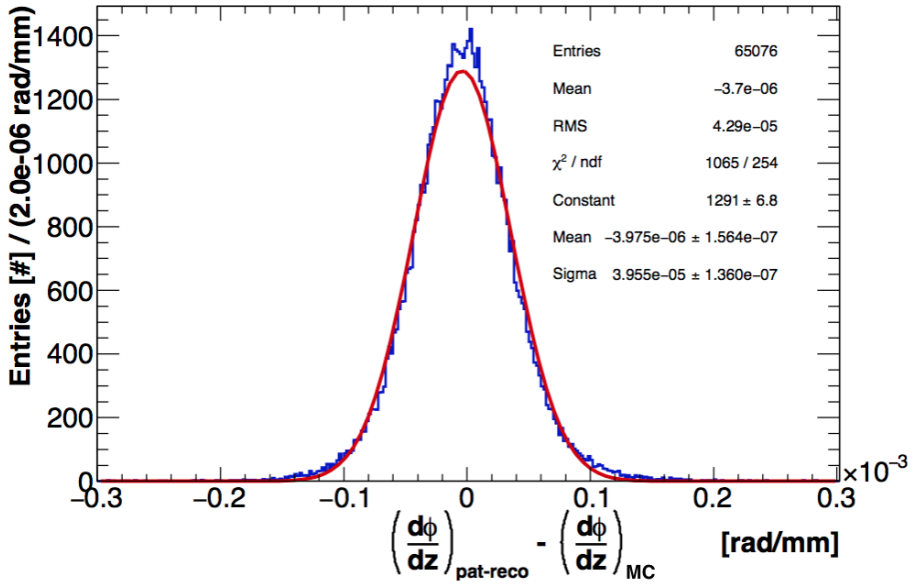

Figure 5.10: Distribution in $d\phi/dz$ residuals at the end of the pattern recognition.

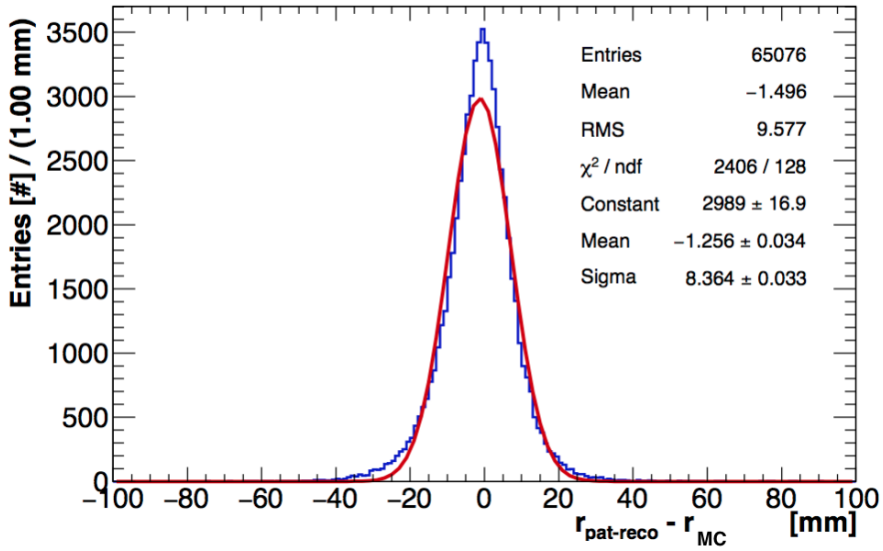

Figure 5.11: Distribution in radial residuals at the end of the pattern recognition.

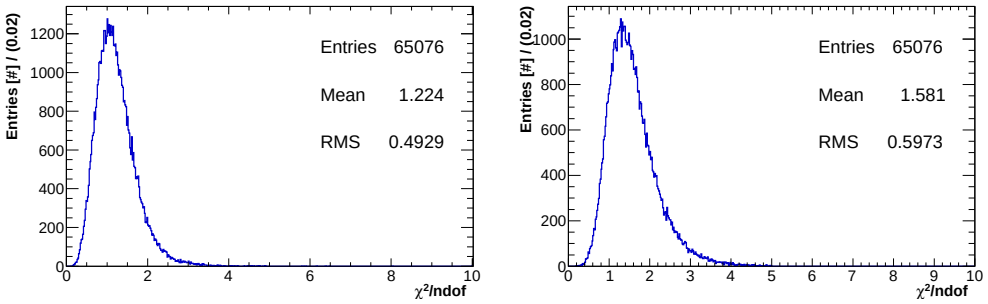

Figure 5.12: Normalized χ^2 distribution for the X-Y circle fit (left) and the ϕ-Z linear fit (right).

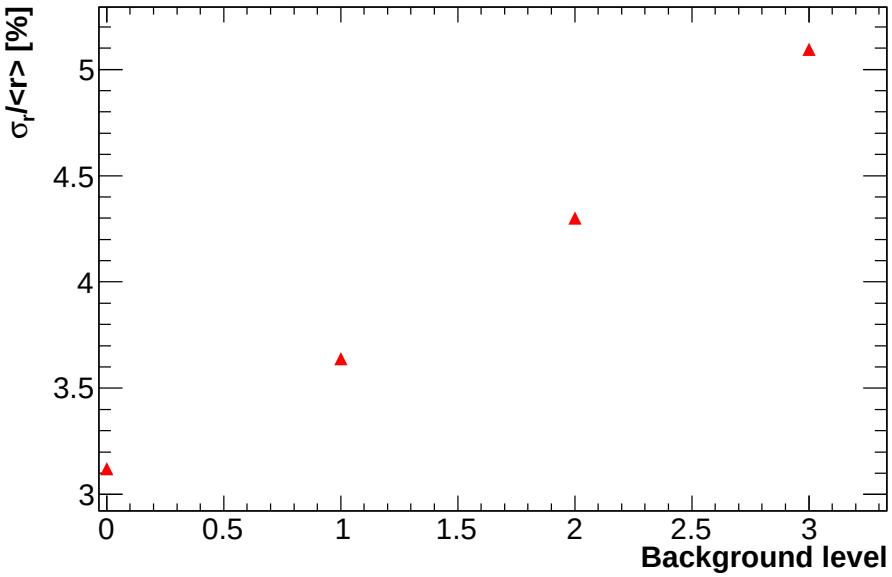

Figure 5.13: $\sigma_r / < r >$ versus the background level. Units on the X axis indicate the background occupancy relative to the nominal case (Background level = 1).

- momentum at the tracker front face $P_{\text{front}} > 100$ MeV/c;
- reconstructed cluster energy above 60 MeV.

Efficiency calculation was performed counting events where the track candidate has at least 15 straw hits. The choice of the threshold corresponds to the require-

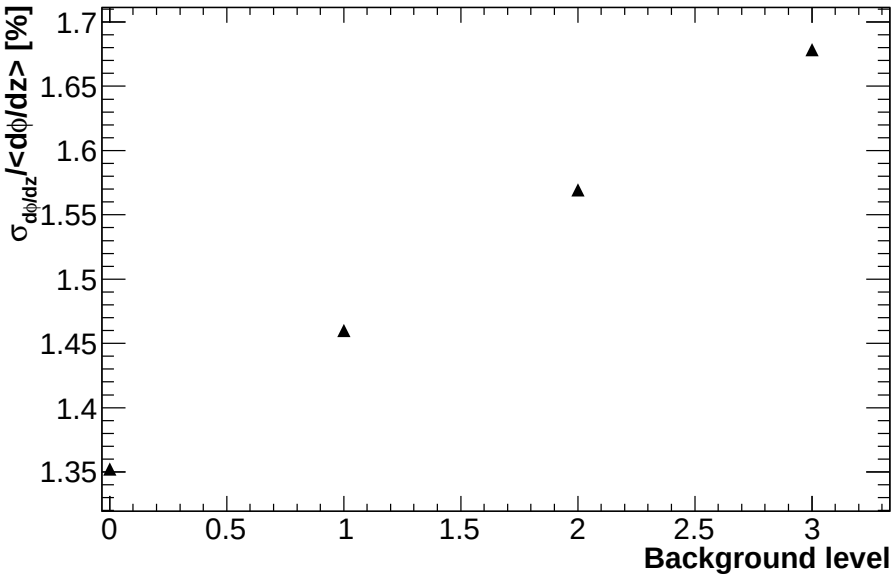

Figure 5.14: $\sigma_{d\phi/dz}/ < d\phi/dz >$ versus the background level. Units on the X axis indicate the background occupancy relative to the nominal case (Background level = 1).

ment to have at least 5 hits for each track loop. Figure 5.15 shows how the pattern recognition efficiency varies as a function of the assumed background occupancy. For background occupancy two times than the expected one, the efficiency goes down by only 3%.

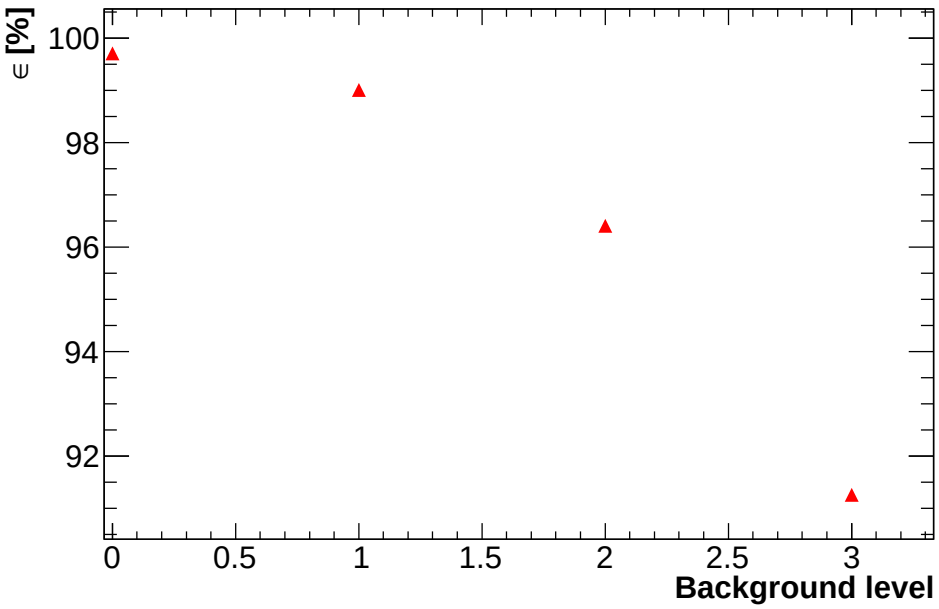

Figure 5.15: Pattern recognition efficiency for simulated $\mu^-\mathrm{N} \rightarrow e^-\mathrm{N}$ events versus the background level. Units on the X axis indicate the background occupancy relative to the nominal case (Background level = 1).

Chapter 6

Improvements in the track reconstruction

Introduction

For Mu2e, the momentum reconstruction is crucial, and its performance drives the sensitivity of the experiment. For that reason, track candidates provided by the two pattern recognition methods (the standalone and the calorimeter-seeded method) are processed separately by a Kalman-based fitter. Track reconstruction performance has been studied using simulated $\mu^-\mathrm{N} \rightarrow e^-\mathrm{N}$ events, and selecting only tracks that fulfill the following quality cuts [1]:

- number of straw hits associated with the track ≥ 25;
- fit-consistency $\geq 2 \cdot 10^{-3}$;
- impact parameter d_0 in the range [-80, 105] mm (geometrical consistency of being produced in the Al stopping target);
- $T_0 > 700$ ns;
- pitch angle - at the entrance of the tracker, $\theta = \arctan(p_L/p) \in [45,60]$ deg.

Tracks reconstructed starting by the two pattern recognition algorithms define three sets of events:

1. events, in which both the calorimeter-seeded and the standalone algorithm found a track fulfilling the quality cuts ($\sim 78\%$ of the total);
2. events, in which only the standalone algorithm found a track fulfilling the quality cuts ($\sim 12\%$ of the total);
3. events, in which only the calorimeter-seeded algorithm found a track fulfilling the quality cuts ($\sim 10\%$ of the total).

In the first case, to avoid duplication of the same track, when two tracks share more than half of their straw hits, only the one with best track-fit χ^2/N_{DOF} is picked up.

Events on the second class can be divided into two sub-samples:

- events, in which no calorimeter cluster above 60 MeV is present ($\sim 92\%$ of this sample);
- events, in which the calorimeter-seeded algorithm fails or does not allow to reconstruct a track fulfilling the quality cuts ($\sim 8\%$ of this sample).

Figure 6.1 shows the distribution in momentum residuals residuals Δp between the reconstructed momentum and the Monte Carlo truth, for the tracks reconstructed in the first class of events. The figure shows no evident systematic effect on the momentum resolution for tracks found by the calorimeter-seeded algorithm.

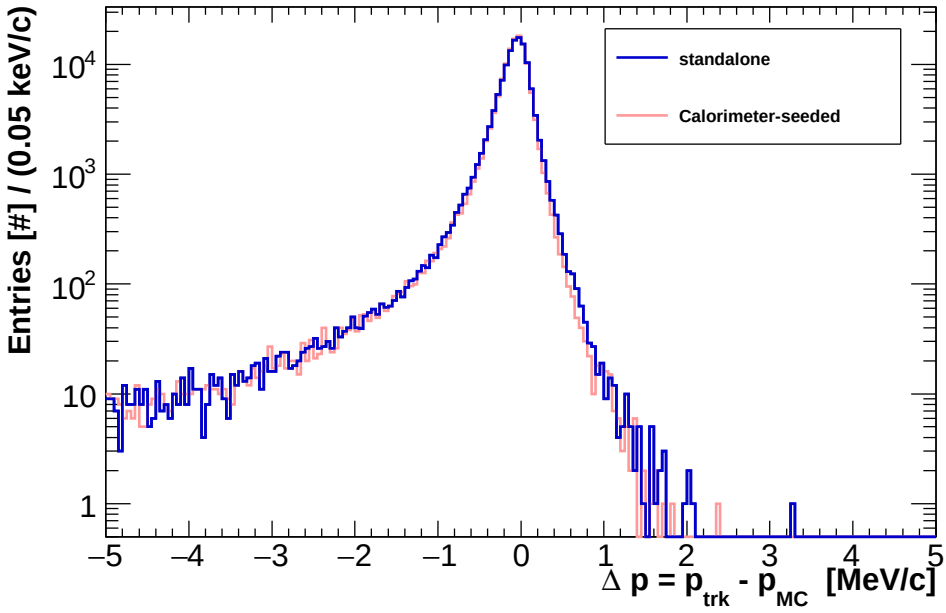

Figure 6.1: CE momentum residuals Δp at the tracker front for tracks found by the standalone (blue line) and the caloriemter-seeded algorithm (red line).

6.1 Improvement in the momentum resolution

For an experiment like Mu2e, where the expected signal is positioned at the kinematic edge of the DIO electrons momentum spectrum, understanding of the momentum resolution, and its tails, becomes of special importance. There are several effects contributing to non-Gaussian tails of the momentum resolution: multiple scattering in the tracker, readout threshold effects, etc. Normally, the misreconstructed hits are rejected by the track fitter. However, there is one more effect that complicates the problem. The drift time reconstruction in a straw tube determines only the drift radius, but not the drift direction. In most cases, large multiple scattering results in large values of the track fit χ^2. However, it is also possible that the best χ^2 inadvertently corresponds to an incorrect assignement of the drift direction, where the drift signs of one or several hits are reversed relative to the correct assignment. Figure 6.2 illustrates this effect. In this case, the reconstructed track momentum corresponding to a hit configuration with the best track fit χ^2 could be significantly different from the true momentum value.

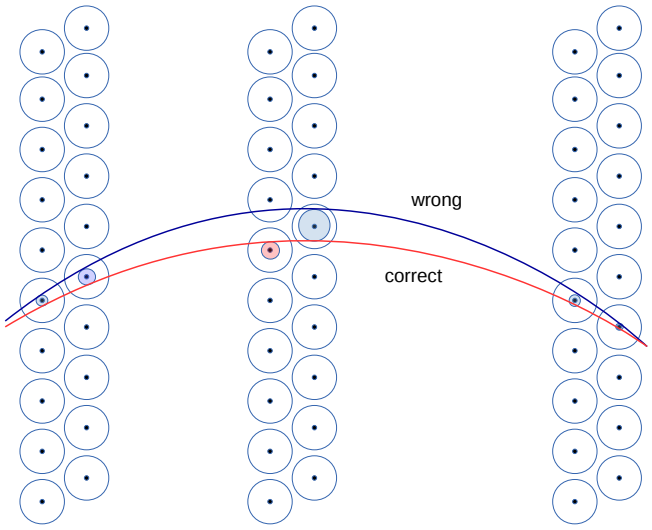

Figure 6.2: Illustration of how wrongly assigned drift signs can impact in the track reconstruction.

The hit drift directions are determined based on the preliminary trajectory of the Kalman fitter, and are used as an input for the track fitter. However, the accuracy of the preliminary trajectory is not sufficient to determine the drift direction unambiguously. As a typical drift distance ($\sim$ 1 mm) is large compared to the hit position resolution ($\sim$ 100 μm), a mis-assigned drift direction could significantly impact the value of the reconstructed momentum. Moreover, the unknown track T_0 complicates correct assignment of the hit drift directions. In principle, one could try all combinations of drift signs. However, with an average of 40 straw hits associated to CE track, performing 2^{40} fits per event is not realistic.

The Mu2e tracker is composed of 2-layer panels. With $\sim$ 80% probability a track has 2 or more hits per panel; such hit configuration is defined as a "doublet". As shown in Figure 6.3, depending on the hit drift directions, one can distinguish same-sign (SS) and opposite-sign (OS) doublets.

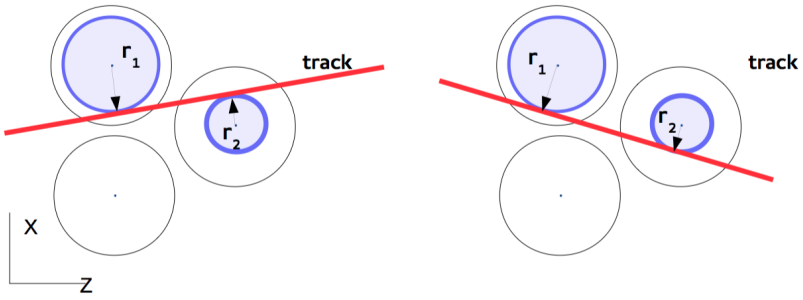

Figure 6.3: Doublet configurations: opposite-sign (OS) hit doublet on the left and same-sign (SS) doublet on the right. Blue circles represent the isochrone lines corresponding to the reconstructed drift times.

As shown in Figure 6.4, the reconstructed trajectory should be close to one of the four lines tangent to the two circles - isochrones, corresponding to the measured drift times. Each line corresponds to a specific combination of the hit drift directions.

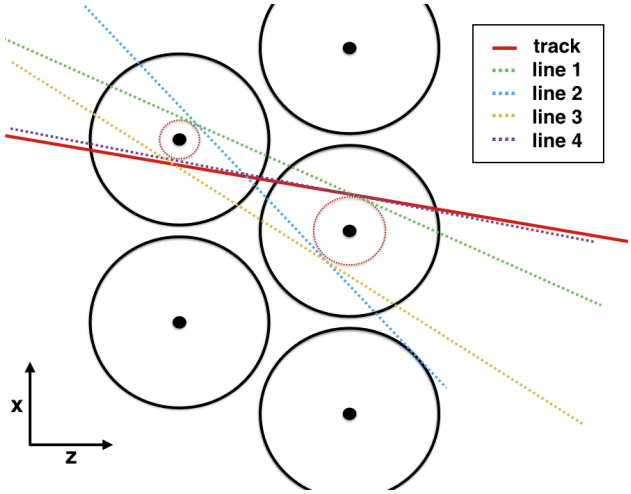

Figure 6.4: Ambiguity resolver scheme: black circles represent the straw tubes, red dashed circles - the drift radii, dashed colored lines - the predicted local particle slopes, and the solid line is the track slope.

To determine the best combination, for each doublet the following χ^2 is evaluated:

$$\chi^2 = \frac{(x\prime_d - x\prime_t)^2}{\sigma^2_{x\prime}} + \frac{(x_d - x_t)^2}{\sigma^2_x},$$

where $x\prime = dx/dz$, t refers to the track, d to the hit doublet with a particular combination of drift directions, σ_x and $\sigma_{x\prime}$ are constants used for combining the two contributions. Figure 6.5 compares the distributions in momentum resolution for tracks reconstructed using two different drift ambiguity resolution algorithms: the hit-based ambiguity resolver (AR) that assigns the hit drift directions based on the hit residuals with respect to the initial trajectory [59], and the doublet-based ambiguity resolver (DAR) introduced above. Using the DAR reduces the

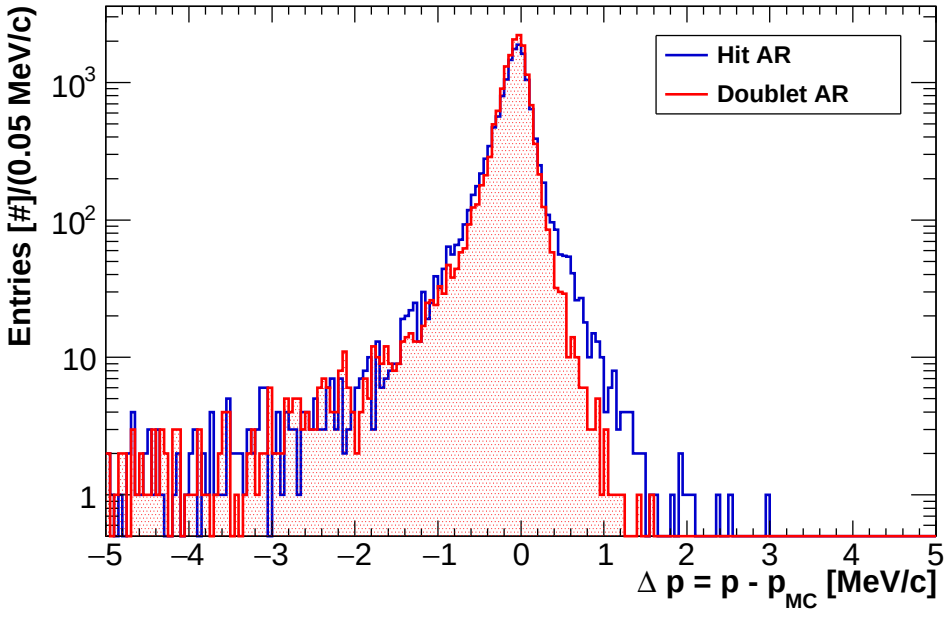

Figure 6.5: CE momentum resolution at the tracker front. Open histogram: AR, hatched histogram - DAR.

high momentum resolution tail such that the total number of events with $\Delta p > 1$ MeV/c goes down by a factor of 5. This allows both to increase the acceptance for CE, and to reduce the expected background from DIO electrons. Distribution in reconstructed momentum, for simulated $\mu^-\mathrm{N} \to e^-\mathrm{N}$ conversion electrons, is shown in Figure 6.6.

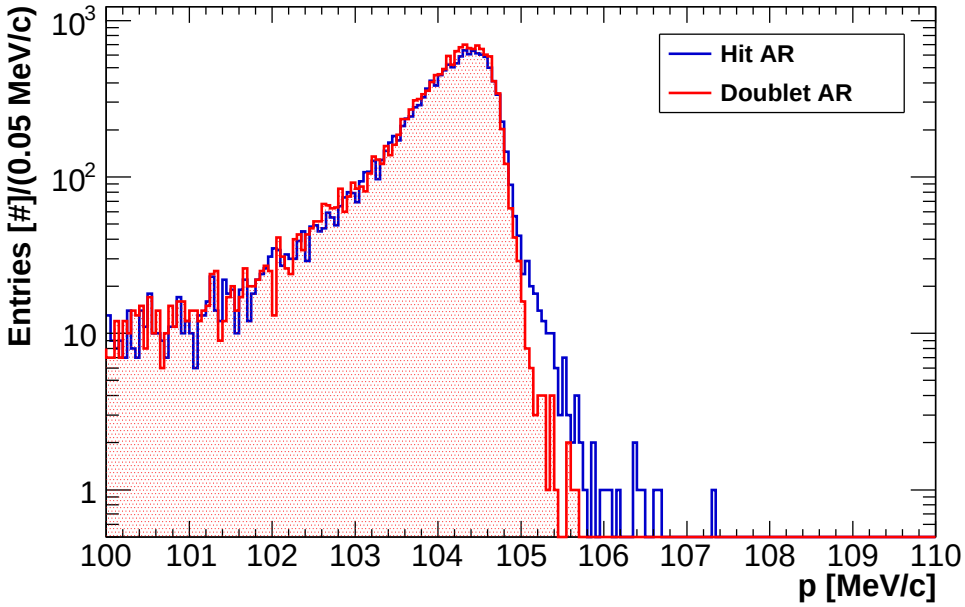

Figure 6.6: Momentum distributions for reconstructed CE. Open histogram: default AR, hatched histogram - DAR.

For the DAR, the high-momentum tail of the distribution is visibly reduced; the number of events with the reconstructed momentum above 105 MeV goes down by a factor of $(2.7 \pm 0.5^{\text{stat}})$. Figure 6.7 shows the reconstructed momentum distributions for simulated DIO electrons. Using DAR results in a significant reduction of the right tail: in the region [103.5, 105] MeV/c, nearby the CE peak, the expected DIO background is reduced by a factor of about 1.8.

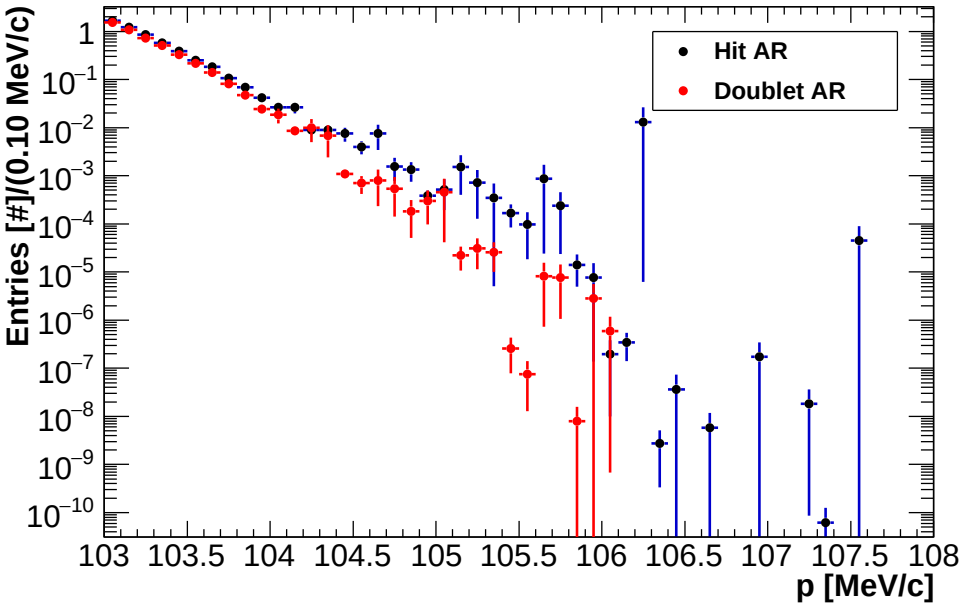

Figure 6.7: Momentum distribution for DIO electrons. Black (red) markers: AR (DAR).

6.2 Efficiency improvement using the calorimeter

Impact of the calorimeter-seeded track search on the track reconstruction efficiency has been evaluated using simulated $\mu^-\mathrm{N} \rightarrow e^-\mathrm{N}$ events, and using only tracks with reconstructed momentum $p > 100$ MeV/c and passing the track quality cuts, as defined in the previous sections. Figure 6.8 shows the track reconstruction efficiency as a function of the expected background level with and without including the calorimeter-seeded algorithm in the pattern recognition. Compared to the standalone algorithm, including the calorimeter-seeded track-finding increases the number of events with the reconstructed CE tracks by $\sim$ 11%. Moreover, same figure shows that the calorimeter-seeded pattern recognition makes the track reconstruction more robust in scenarios with higher background level.

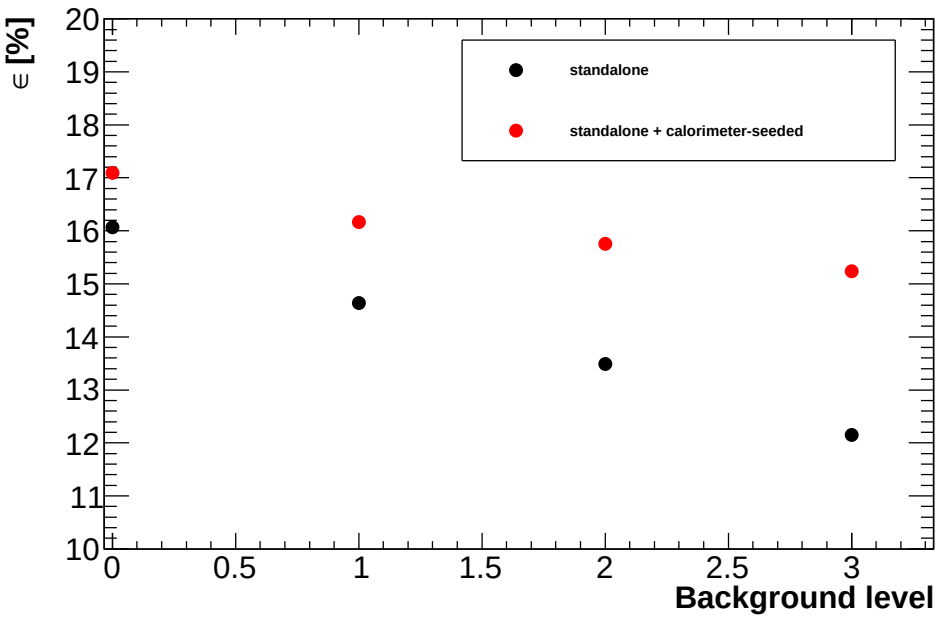

Figure 6.8: Track reconstruction efficiency versus the expected background level. Black dots: standalone track reconstruction, red dots: standalone plus calorimeter-seeded track reconstruction.

Figure 6.9 shows the relative improvement in the efficiency versus the background level; the gain ranges from 11 up to 25 % for the background three times higher than the expected one.

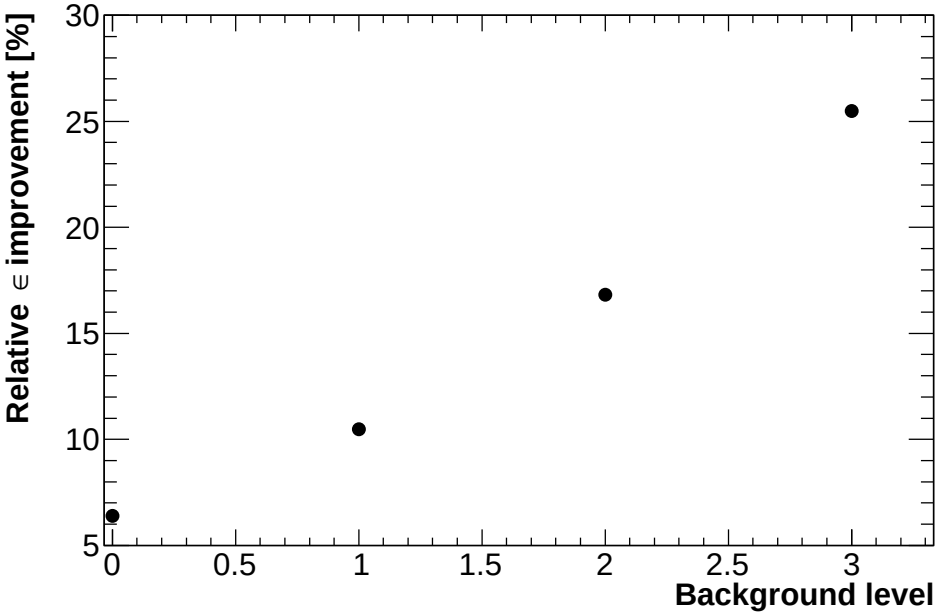

Figure 6.9: Track reconstruction efficiency improvement, by means of the caloriemter-seeded algorithm, versus the expected background level.

Chapter 7

Particle identification and expected sensitivity

For a discovery experiment like Mu2e, suppression of the background sources is fundamental. As already discussed in the first chapter, in the Mu2e case two of the main background sources are: cosmic muons, and products from antiprotons annihilation. The cosmic and the antiproton induced background can be divided into two main categories:

1. Electrons produced via interactions that produce a electron track;
2. Non-electron particles (such as muons or pions), that are reconstructed as an electron track.

The first category represents the irreducible part, while the second one can be suppressed by means of particle identification.

7.1 Calorimeter-based particle identification

The Mu2e, the particle identification (PID) combines information from reconstructed tracks and calorimeter clusters, to reject non-electron particles that can mimic CEs. Simulation results show that after 3 years of data taking, and assuming a Cosmic ray veto inefficiency of 10^{-4}, the total number of background events induced by cosmic muons are: 0.078 ± 0.017 from electrons, and 0.77 ± 0.4

from mis-reconstructed muons [1]. The requirement for the backgrond from mis-reconstructed muons to be much lower than the background from cosmic $\mu \rightarrow e$ can be satisfied by a whole range of choices. For example, a muon rejection factor R > 100 results in the background from mis-reconstructed muons being about 10% of that from electrons. Our choice of R = 200 or better corresponds to the 5%.

7.1.1 Cosmic muons rejection

100 MeV/c electrons are ultra-relativistic ($E/m_e \sim 200$), while 100 MeV/c muons travel at a speed of about 0.7 c. Therefore only with the correct assumption about the particle mass, will the time of the particle track, when extrapolated to the calorimeter, be compatible to the one measured in the calorimeter itself.

as extrapolated to the calorimeter face, will be compatible to the one measured by means of the calorimeter. If a muon track has been extrapolated into the calorimeter assuming it was an electron, the predicted arrival time t_{track} of the muon will be systematically lower than the calorimeter time $t_{cluster}$.

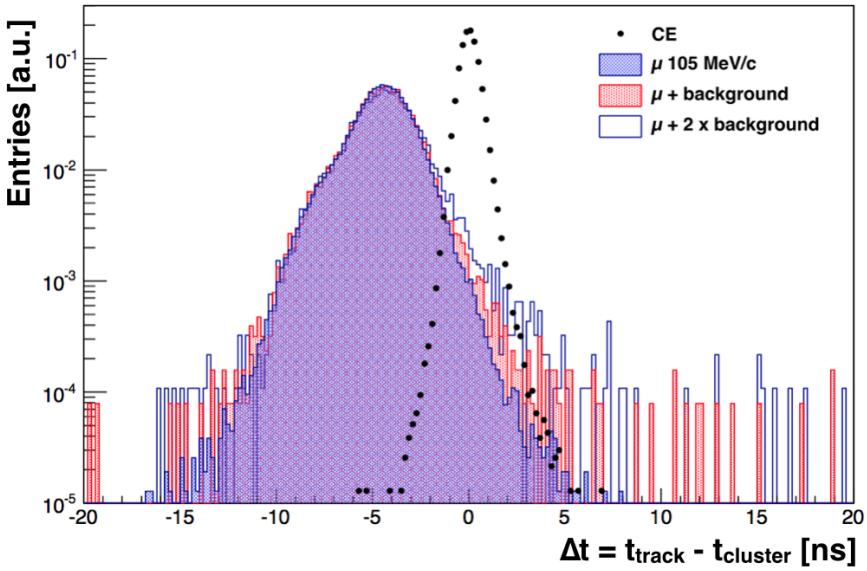

Figure 7.1: Distribution in $\Delta t = t_{track} - t_{cluster}$ [ns] for CEs (open histogram) and 105 MeV/c muons (blue filled histogram). Different colors correspond to different assumption of the background level.

Figure 7.1 shows the distributions in $\Delta t = t_{track} - t_{cluster}$ for CEs and 105 MeV/c muons reconstructed as electrons. The maxima of the electron and muon distributions differs by about 5 ns.

The $\mu - e$ separation is improved by using also the quantity E/p, where E is the reconstructed cluster energy and p is the track momentum. Figure 7.2 shows distributions in E/p for CE and 105 MeV/c muons. The peak at 0.4 in the muon E/p distribution corresponds to its kinetic energy summed with the energy from the μ^- capture. The muon distribution also shows a long tail above E/p=0.4, corresponding to the μ^- 3-bodies decay $\mu^- \rightarrow e^- \bar{\nu}_e \nu_\mu$.

Δt and the E/p are combined in the following log likelihood:

$$\ln L_{e,\mu} = \ln P_{e,\mu}(\Delta t) + \ln P_{e,\mu}(E_{cluster}/p_{track}) \,, \tag{7.1}$$

where $P_{e,\mu}(\Delta t)$ and $P_{e,\mu}(E_{cluster}/p_{track})$ are the probability densities for electrons and muons respectively. The likelihood ratio is then used for the final decision:

$$\ln L_{e/\mu} = \frac{\ln L_e}{\ln L_\mu} = \ln L_e - \ln L_\mu. \tag{7.2}$$

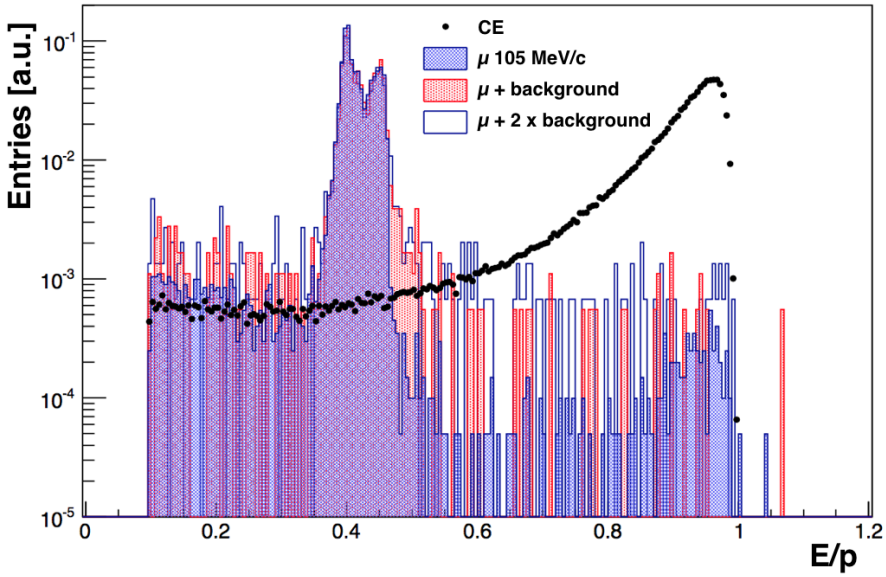

Figure 7.2: Distribution in E / p for CEs (open histogram) and muons (blue filled histogram). Different colors correspond to different assumption of the background level.

Figure 7.3 shows the distribution in $\ln L_{e/\mu}$ for CEs and 105 MeV/c muons. A cut at $\ln L_{e/\mu} \geq 1.5$ ensures a muon rejection factor of 200, as requested by [1]; Figure 7.4 shows the muon rejection factor as a function of the electron identification efficiency in different scenarios: no background, x1, x2 expected background. At the expected occupancy level the electron identification efficiency is of about 96.5% and it goes down to 93% when the background occupancy doubles.

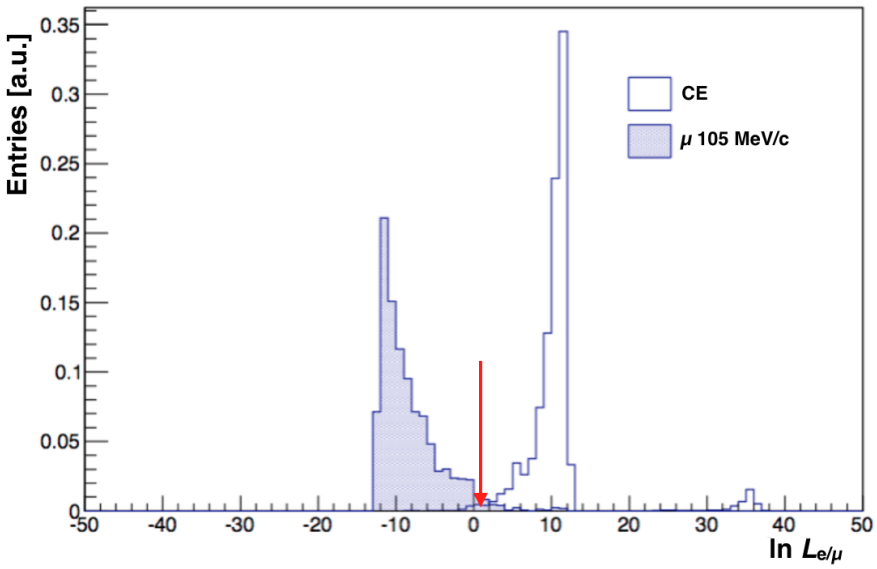

Figure 7.3: Likelihood ratio distribution for CEs (open histogram) and muons (blue filled histogram). Red arrow points to L = 1.5.

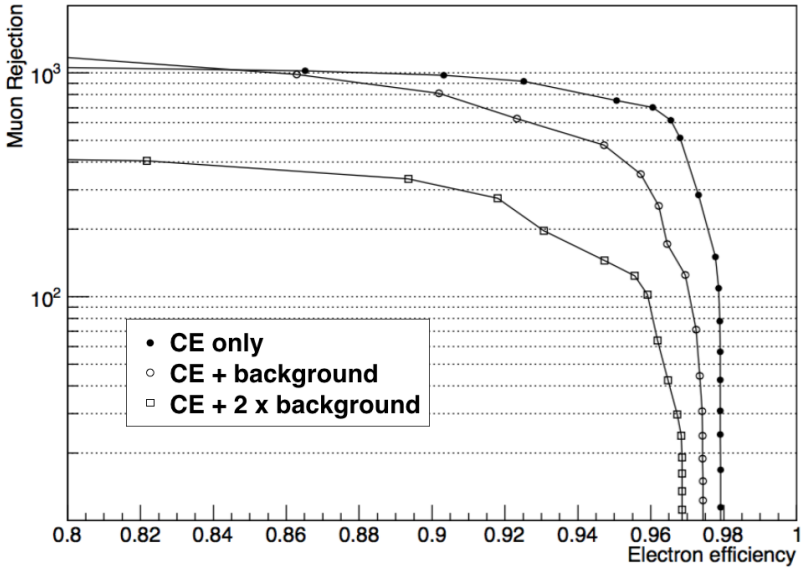

Figure 7.4: Muon rejection factor versus electron identification efficiency for several scenarios: no presence of backgrounds, x1 and x2 the expected background.

PID performance has been studied varying the expected calorimeter performance. Figure 7.5 shows the CE identification efficiency in the configuration with the

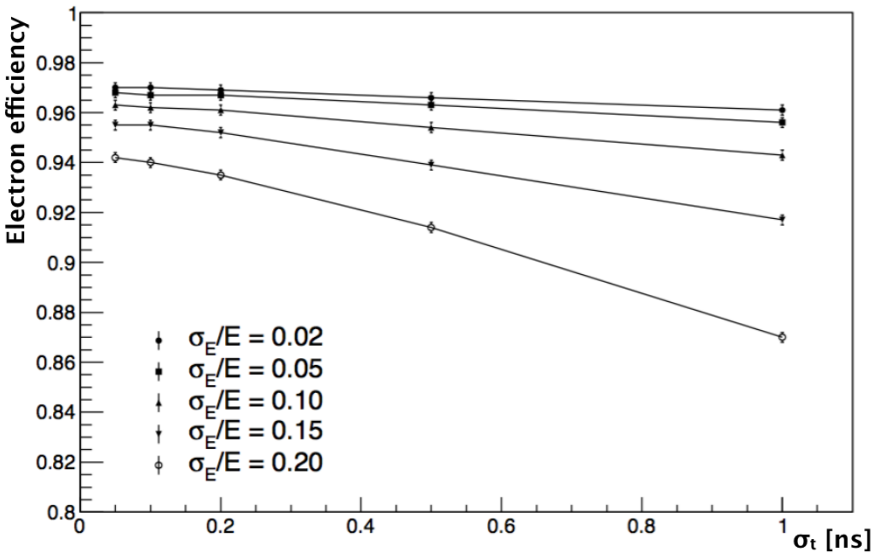

Figure 7.5: PID efficiency versus σ_t assuming the energy resolution $0.02 < \sigma_E/E < 0.2$ with a muon rejection factor of 200.

expected background level, at a fixed rejection factor of 200, versus the expected time resolution σ_t, assuming several values of energy resolution σ_E. In the range of resolutions $\sigma_E/E < 0.1$ and $\sigma_t < 0.5$ ns, the PID efficiency is stable within 2%.

7.1.2 $\bar{p}$ induced background rejection

Antiprotons reaching the detector solenoid can interact either in the collimator at the entrance of the detector solenoid, or in the Al stopping target, producing different particles in a wide momentum range. Figure 7.6 shows the momentum distributions, at the production time, for the particles produced in the annihilation. Figure 7.7 shows the reconstructed momentum distribution for particles recon-

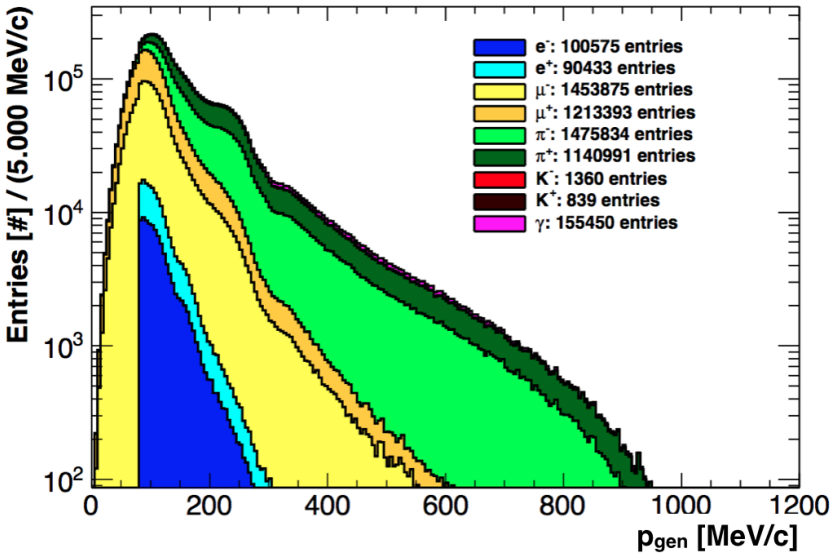

Figure 7.6: Momentum distribution at the time of production for all particles originating from $\bar{p}$ annihilation.

structed in the tracker.

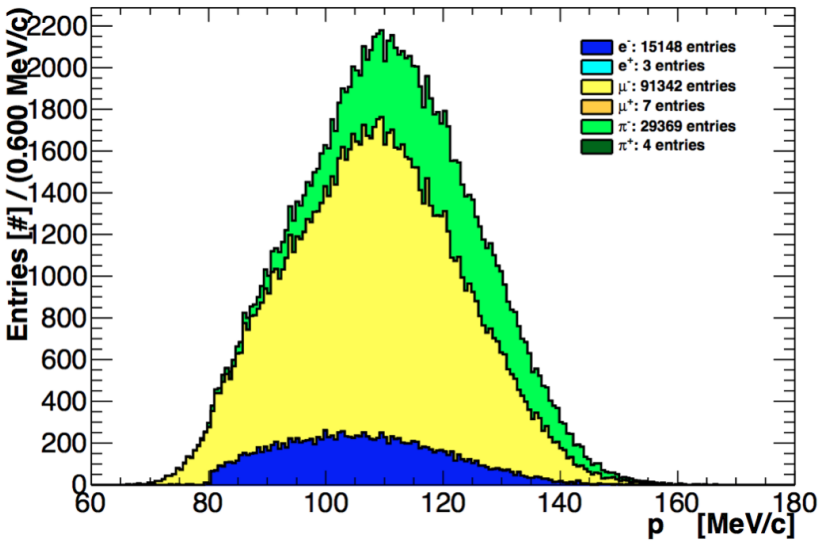

Figure 7.7: Reconstructed momentum distribution for all tracks from the $\bar{p}$ annihilation.

The electron tracks in the range close to 105 MeV/c mimic the CE, and represent the irreducible background [1]. On the contrary, pion and muon tracks mimicking the CE can be rejected using the calorimeter PID. Figure 7.8 shows the distribution in Δt for tracks in the momentum range [101, 106] MeV/c. As expected, the electron component of the Δt distribution in Figure 7.8 is well centered to zero, while distributions for μ^- and π^- are peaked approximately around -5 ns, because their β is respectively $\sim$ 0.7 for μ^- and $\sim$ 0.6 for π^- . Figure 7.9 shows the distribution in E/p for the tracks in the same momentum range. The π^- component of the distribution peaks close to 0.4, according to its kinetic energy, and has a large right tail above E/p=0.4 due to the π^- charge exchange processes, followed by the π^0 decay. The μ^- behavior is as already shown in the previous paragraph.

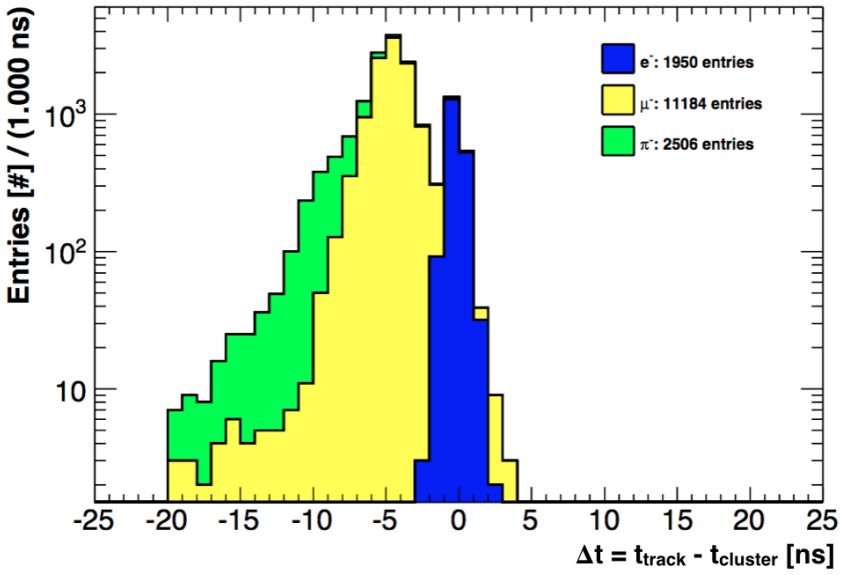

Figure 7.8: Distribution in Δt for e^-, μ^- , and π^- tracks with p $\in$ [101, 106] MeV/c.

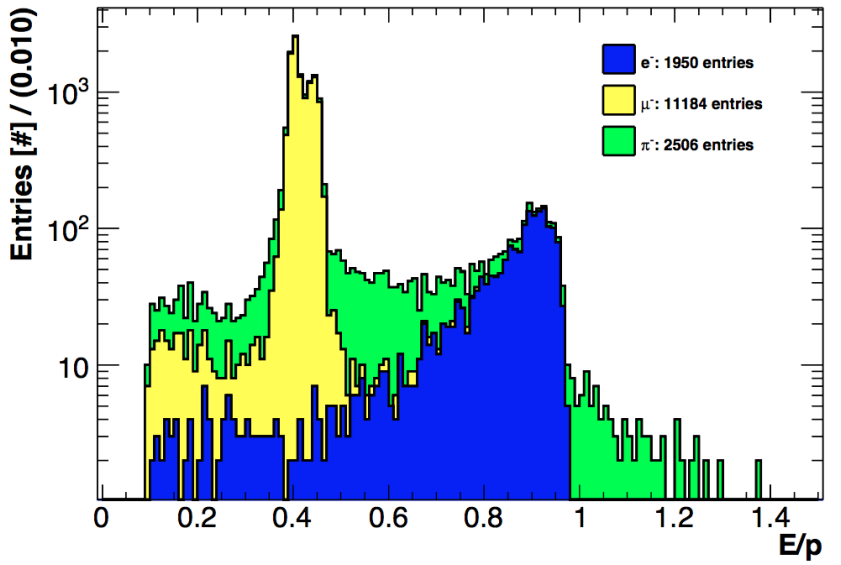

Figure 7.9: Distribution in E/p for e^-, μ^- , and π^- tracks with p $\in$ [101, 106] MeV/c.

Pion and muon distributions in Δt and E/p are similar. For that reason, only the muon template has been used in the PID algorithm. Figure 7.10 shows the resulting distribution in the likelihood ratio $\ln L_e/L_\mu$. Applying the same cut used for

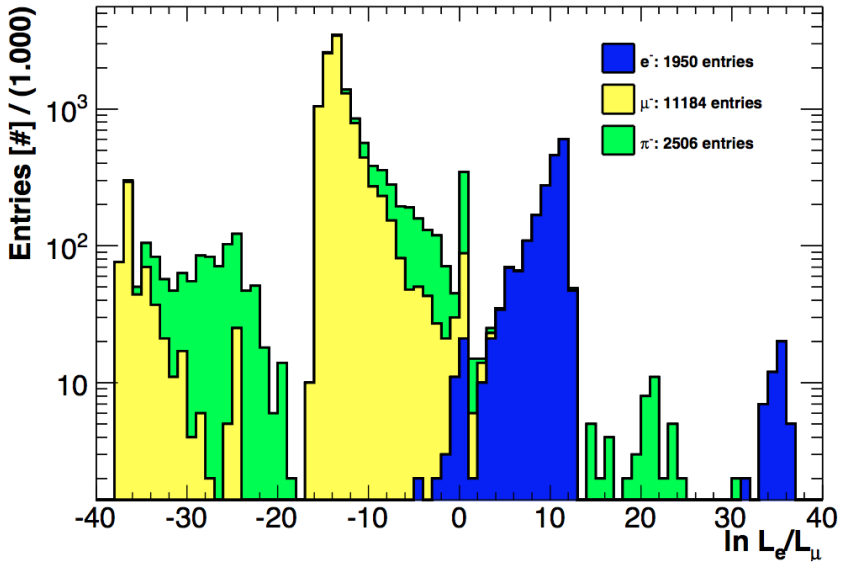

Figure 7.10: Distribution in $\ln L_e/L_\mu$ for e^-, μ^- , and π^- tracks with p ∈ [101, 106] MeV/c.

the cosmic muon rejection ($\ln L_{e/\mu} = 1.5$), and scaling the result to the expected Mu2e luminosity, the total number of events with a pion or muon track in the momentum range [101, 106] MeV/c is $\leq 4 \times 10^{-3}$ (statistical uncertainty below 10^{-7}).

7.2 Mu2e sensitivity estimation

In HEP there is a large variety of experiments that optimize their design for the search of a single, or just few, new phenomena. The figure of merit used for driving the optimization process is the sensitivity, defined as the average upper limit one would get from an ensemble of experiments with the expected background and no true signal. Several approaches for setting confidence levels and upper limits have been widely discussed in the HEP community[62–64]. As $\mu^-\mathrm{N} \rightarrow e^-\mathrm{N}$ search in Mu2e represents is close to a "background-free"case, the CL_s method [64] has been chosen for evaluating the experimental sensitivity.

The CL_s method always deals with two hypothesis: background-only ("b"), i.e., the data can be understood with existing physics explanations, and signal + background ("$s + b$"), i.e., new physics is needed to understand the data. The 90% C.L. upper limit is derived from the probability density function (PDF) of $-2\ln(Q)$, where $Q = L(s+b)/L(b)$ is the ratio of the likelihoods from the two hypothesis of interest. The Likelihood function can be written as:

$$\begin{aligned} L(s,b) &= \exp[-(s+b)]\frac{(s+b)^n}{n!} \cdot \prod P(x_i) \\ P(x_i) &= s\,S(x_i) + b\,B(x_i)\,, \end{aligned}$$

where n is the estimated signal , b the estimated background yield, s the estimated signal yield, and $S(x_i)$ and $B(x_i)$ are the PDFs for the discriminating variables x_i, for signal and the background.

7.2.1 Input for the sensitivity calculation

In Mu2e, the reconstructed track momentum is expected to be the most precise observable. Taking into account only tracks passing the quality cuts, as defined in chapter 6, and the Mu2e PID selection, the track momentum provides the strongest separation between the CE and the background. For that reason, the momentum distributions of simulated CE and background have been used as PDFs. This estimate does not include contributions from several systematic uncertainties like the uncertainty on the momentum scale. We also use the leading order momentum spectra and do not consider effect of the radiative corrections.

The background component has been factorized into two separate PDFs: one for the DIO electrons, and the second one for the other background sources. Simulation studies showed that in the range [102, 106] MeV/c, the non-DIO component of the background can be well modeled with a flat distribution, with an accuracy better than 10%. Figure 7.11 shows all the PDFs used as input for the sensitivity calculation.

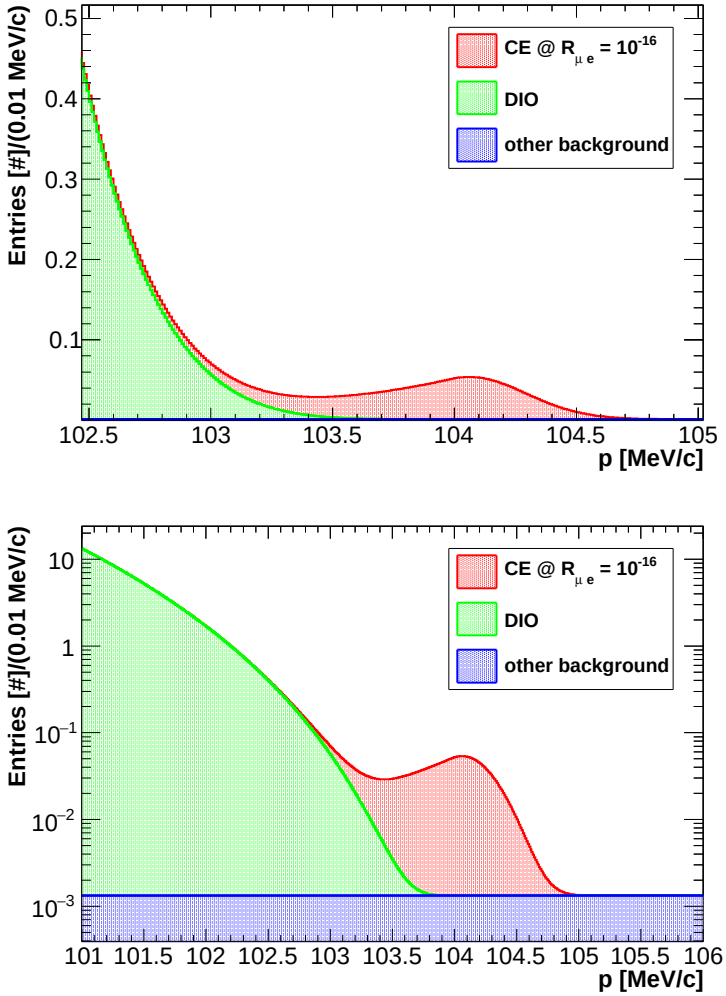

Figure 7.11: Momentum distribution in linear (top) and log (bottom) scale, for background and CE, assuming $R_{\mu e} = 10^{-16}$. Distributions are normalized to the Mu2e expected number of protons on target in 3 years of running, $N = 3.6 \cdot 10^{20}$.

7.2.2 Results for 90% CL upper limit

The sensitivity should not depend on the limits of the PDFs used as input, so to check the stability of the result, calculation has been repeated varying the lower edge p_{min} of the PDFs in the range [102, 103] MeV/c. Figure7.12 shows the result of this scan. The sensitivity does not depend on the PDFs region below 103

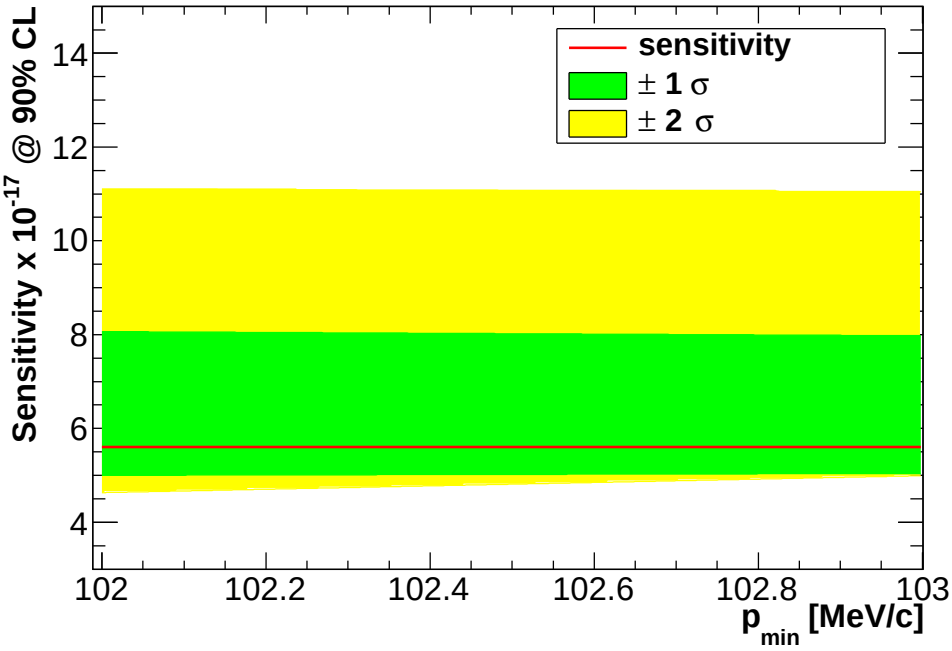

Figure 7.12: Sensitivity scan with sidebands at $\pm 1,\ 2\ \sigma$.

MeV/c. The stability of the result has also been studied as a function the number of the generated pseudo-experiments $N_{pseudo-exp}$. As an example, Figure 7.13 shows how the sensitivity calculated with p_{min} = 102.5 MeV/c varies as a function of $N_{pseudo-exp}$. Above 300 $N_{pseudo-exp}$, the sensitivity variations are within 1%. The result, corresponding to $N_{pseudo-exp}$ = 1000, has been used for quoting the final result:

$$R_{\mu e} \leq 5.6 \cdot 10^{-17} \text{ @ } 90\% \text{ CL} .$$

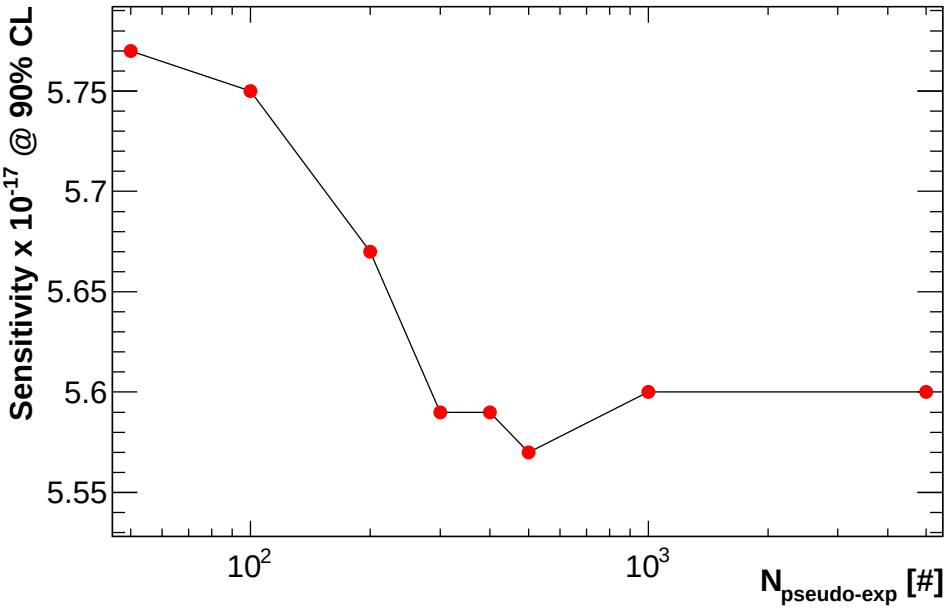

Figure 7.13: Sensitivity scan in number of generated pseudo-experiments.

Chapter 8

Conclusions

The work of this thesis has been focused to the calorimeter R&D, and the role of the calorimeter in the Mu2e experiment.

It has been also demonstrated that the calorimeter information can be used to improve the track reconstruction efficiency, and make it more robust in scenarios with higher occupancy than the expected one.

The calorimeter time and energy measurements are also essential for rejecting the non-electron particles that can dangerously mimic the $\mu^-\mathrm{N} \rightarrow e^-\mathrm{N}$ conversion electron. Simulation studies show that the calorimeter time and energy resolutions $\sigma_t < 500$ ps, and $\sigma_E/E < 10\%$ would provide the muon rejection factor $R > 200$, while keeping the electron identification efficiency above 96%.

The time resolution of the calorimeter has been measured in a test beam in April 2015, where a reduced scale calorimeter prototype was exposed to an electron beam: a time resolution of the order of 130 ps has been obtained for 100 MeV electrons.

Given these results, the following estimate of the Mu2e sensitivity has been obtained: $R_{\mu e} \leq 5.6 \cdot 10^{-17}$@90% CL.

Bibliography

1. Bartoszek, L. *et al.* Mu2e Technical Design Report. arXiv: 1501.05241 [physics.ins-det] (2014).
2. Marciano, W. J., Mori, T. & Roney, J. M. Charged Lepton Flavor Violation Experiments*. *Annual Review of Nuclear and Particle Science* **58,** 315–341 (2008).
3. Kuno, Y. & Okada, Y. Muon decay and physics beyond the standard model. *Rev. Mod. Phys.* **73,** 151–202 (1 2001).
4. Bertl, W. *et al.* A search for $\mu - e$ conversion in muonic gold. English. *The European Physical Journal C - Particles and Fields* **47,** 337–346. ISSN: 1434-6044 (2006).
5. Weinberg, S. *The Quantum Theory of Fields, Volume 1: Foundations* ISBN: 0521670535 (Cambridge University Press).
6. Weinberg, S. *The quantum theory of fields. Vol. 2: Modern applications* Cambridge, UK: Univ. Pr. (1996) 489 p ().
7. Weinberg, S. *The quantum theory of fields. Vol. 3: Supersymmetry* Cambridge, UK: Univ. Pr. (2000) 419 p ().
8. Olive, K. A. *et al.* Review of Particle Physics. *Chin. Phys.* **C38,** 090001 (2014).
9. Bernstein, R. H. & Cooper, P. S. Charged Lepton Flavor Violation: An Experimenter's Guide. *Phys. Rept.* **532,** 27–64 (2013).
10. Barbieri, R. & Hall, L. J. Signals for supersymmetric unification. *Phys. Lett.* **B338,** 212–218 (1994).
11. Barbieri, R., Hall, L. J. & Strumia, A. Violations of lepton flavor and CP in supersymmetric unified theories. *Nucl. Phys.* **B445,** 219–251 (1995).
12. Adam, J. *et al.* New Constraint on the Existence of the $\mu^+ \to e^+\gamma$ Decay. *Phys. Rev. Lett.* **110,** 201801 (20 2013).

13. Bellgardt, U. *et al.* Search for the decay $\pi^+ \to e^+e^+e$. *Nuclear Physics B* **299,** 1 –6. ISSN: 0550-3213 (1988).
14. Van der Schaaf, A. *et al. NOON03 Conference Proceedings* (2003).
15. Aubert, B. *et al.* Searches for Lepton Flavor Violation in the Decays $\tau^{+-} \to e^{+-}\gamma$ and $\tau^{+-} \to \mu^{+-}\gamma$. *Phys. Rev. Lett.* **104,** 021802 (2010).
16. Hayasaka, K. *et al.* Search for lepton-flavor-violating τ decays into three leptons with 719 million produced pairs. *Physics Letters B* **687,** 139 –143. ISSN: 0370-2693 (2010).
17. Krolak, P. *et al.* A limit on the lepton-family number violating process $\pi^0 \to \pi^{\pm}e^{\mp}$. *Physics Letters B* **320,** 407 –410. ISSN: 0370-2693 (1994).
18. Ambrose, D. *et al.* New Limit on Muon and Electron Lepton Number Violation from $K^0_L \to \mu^{\pm}e^{\mp}$ Decay. *Phys. Rev. Lett.* **81,** 5734–5737 (26 1998).
19. Lee, A. M. *et al.* Improved limit on the branching ratio of $K^+ \to \pi^+\mu^+e^-$. *Phys. Rev. Lett.* **64,** 165–168 (2 1990).
20. Bellantoni, L. *Recent results from KTeV* in *36th Rencontres de Moriond on Electroweak Interactions and Unified Theories Les Arcs, France, March 10-17, 2001* (2001). arXiv: hep-ex/0107045 [hep-ex]. <http://lss.fnal.gov/cgi-bin/find_paper.pl?conf-01-220>.
21. Akers, R. *et al.* A search for lepton flavour violating Z0 decays. English. *Zeitschrift fur Physik C Particles and Fields* **67,** 555–563. ISSN: 0170-9739 (1995).
22. Abreu, P. *et al.* Search for lepton flavor number violating Z0 decays. *Z. Phys.* **C73,** 243–251 (1997).
23. De Gouvea, A. & Vogel, P. Lepton Flavor and Number Conservation, and Physics Beyond the Standard Model. *Prog. Part. Nucl. Phys.* **71,** 75–92 (2013).
24. Baldini, A. M. *et al.* MEG Upgrade Proposal. arXiv: 1301.7225 [physics.ins-det] (2013).
25. Berger, N. The Mu3e Experiment. *Nuclear Physics B - Proceedings Supplements* **248-250.** 1st Conference on Charged Lepton Flavor Violation1st Conference on Charged Lepton Flavor Violation, 35 –40. ISSN: 0920-5632 (2014).
26. Kitano, R., Koike, M. & Okada, Y. Detailed calculation of lepton flavor violating muon-electron conversion rate for various nuclei. *Phys. Rev. D* **66,** 096002 (9 2002).
27. Measday, D. The nuclear physics of muon capture. *Physics Reports* **354,** 243 –409. ISSN: 0370-1573 (2001).

28. Czarnecki, A., Garcia i Tormo, X. & Marciano, W. Muon decay in orbit: Spectrum of high-energy electrons. *Phys. Rev. D* **84,** 013006 (1 2011).
29. Kaulard, J. *et al.* Improved limit on the branching ratio of $\mu^- \to e^+$ conversion on titanium. *Physics Letters B* **422,** 334 –338. ISSN: 0370-2693 (1998).
30. Nakatsugawa, Y. Search for muon to electron conversion at J-PARC MLF : Recent status on DeeMe. *PoS* **NUFACT2014,** 093 (2015).
31. Litchfield, R. P. *Muon to electron conversion: The COMET and Mu2e experiments* in *Interplay between Particle and Astroparticle physics London, United Kingdom, August 18-22, 2014* (2014). arXiv: 1412.1406 [physics.ins-det]. <http://inspirehep.net/record/1332516/files/arXiv:1412.1406.pdf>.
32. Kuno, Y. A search for muon-to-electron conversion at J-PARC: The COMET experiment. *PTEP* **2013,** 022C01 (2013).
33. Dzhilkibaev, R. M. & Lobashev, V. M. *The solenoid muon capture system for the MELC experiment* in *Beam Dynamics and Technology Issues for mu+ mu- Colliders* (1995).
34. Popp, J. L. The MECO experiment: A Search for lepton flavor violation in muonic atoms. *NIM* **A472,** 354–358 (2000).
35. Hino, Y. *et al.* A Highly intense DC muon source, MuSIC and muon CLFV search. *Nuclear Physics B - Proceedings Supplements* **253-255.** The Twelfth International Workshop on Tau-Lepton Physics (TAU2012), 206–207. ISSN: 0920-5632 (2014).
36. Litchfield, R. P. Status of the AlCap experiment. *PoS* **NUFACT2014,** 095 (2015).
37. Bartoszek, L. *et al.* Mu2e Conceptual Design Report. arXiv: 1211.7019 [physics.ins-det] (2012).
38. Cordelli, M. *et al.* Test of a LYSO matrix with an electron beam between 100 and 500 MeV for KLOE-2. *NIM A* **617.** 11th Pisa Meeting on Advanced DetectorsProceedings of the 11th Pisa Meeting on Advanced Detectors, 109 –112. ISSN: 0168-9002 (2010).
39. Atanov, N. *et al.* Measurement of time resolution of the Mu2e LYSO calorimeter prototype. *NIM A* **812,** 104 –111. ISSN: 0168-9002 (2016).
40. *SAINT GOBAIN Saint Gobain web page* http://www.crystals.saint-gobain.com/. Accessed: 2015-08-30.
41. Hamada, M., Nunoya, Y, Kubota, S & Sakuragi, S. Suppression of the slow emission component in pure CsI by heat treatment. *NIM A* **365,** 98 –103. ISSN: 0168-9002 (1995).

42. *PMT R2059 Hamamatsu PMT R2059 datasheet* http://www.hamamatsu.com/resources/pdf/etd/R1828-01_R2059_TPMH1259E.pdf. Accessed: 2015.
43. *TSV MPPC TSV MPPC datasheet* http://www.nuclear.gla.ac.uk/~jrma/A2/Tagger/NewFPD/SiPMT/KSX-I50014-E_S12642f. Accessed: 2015-08-30.
44. Yahlali, N. *et al.* Imaging with SiPMs in noble-gas detectors. arXiv: 1501.05241 [physics.ins-det] (2012).
45. Leroy, C. & Rancoita, P.-G. Particle interaction and displacement damage in silicon devices operated in radiation environments. *Reports on Progress in Physics* **70,** 493 (2007).
46. Qiang, Y., Zorn, C., Barbosa, F. & Smith, E. Radiation hardness tests of SiPMs for the {JLab} Hall D Barrel calorimeter. *NIM A* **698,** 234 –241. ISSN: 0168-9002 (2013).
47. Zhu, R.-Y. The Next Generation of Crystal Detectors. *Journal of Physics: Conference Series* **587,** 012055 (2015).
48. Pezzullo, G. *et al.* Progress status for the Mu2e calorimeter system. *Journal of Physics: Conference Series* **587,** 012047 (2015).
49. De Fatis, T. T. Calibration of the electromagnetic calorimeter of the CMS experiment. *Journal of Physics: Conference Series* **160,** 012051 (2009).
50. Agostinelli, S. *et al.* Geant4–a simulation toolkit. *NIM A* **506,** 250 –303. ISSN: 0168-9002 (2003).
51. Mazzitelli, G, Ghigo, A, Sannibale, F, Valente, P & Vignola, G. Commissioning of the DAϕNE beam test facility. *NIM A* **515,** 524 –542. ISSN: 0168-9002 (2003).
52. K. Abe, e. a. Undoped CsI calorimeter for the $K_L^0 \to \pi^0\nu\nu$ experiment at KEK-PS. *NIM* **A545,** 278–295 (2005).
53. E. Iwai, e. a. Performance study of a prototype pure CsI calorimeter for the KOTO experiment. *NIM* **A786,** 135 (2015).
54. *Filar optoMaterials Filar optoMaterials s.r.l.* http://www.filaroptomaterials.com. Accessed: 2015.
55. *ISMA Institute for Scintillating Materials* http://isma.kharkov.ua/eng. Accessed: 2015.
56. *Rhodorsil silicon paste 7 Rhodorsil silicon paste 7 datasheet* http://www.siliconipadova.com/public/schede/174/PATE7-ING.pdf. Accessed: 2015.

57. *V1720 digitizer board CAEN V1720 digitizer board datasheet* `http://www.caen.it/csite/CaenProd.jsp?idmod=570&parent=11`. Accessed: 2015.
58. Grupen, C. *Particle detectors* 239–240 (1996).
59. Brown, D. Mu2e: a Muon to Electron Conversion Experiment at Fermilab. *Nuclear Physics B - Proceedings Supplements* **248-250.** 1st Conference on Charged Lepton Flavor Violation1st Conference on Charged Lepton Flavor Violation, 41–46. ISSN: 0920-5632 (2014).
60. Pezzullo, G. & Murat, P. The calorimeter-seeded track reconstruction for the Mu2e experiment at Fermilab. *IEEE Trans. Nuclear Sci.* (to be published).
61. N. I. Chernov, G. O. Effective algorithms for circle fitting. *NIM* **A33,** 399–333 (4 1984).
62. Kempthorne, O. *Journal of the American Statistical Association* **65,** 455–456. ISSN: 01621459 (1970).
63. Feldman, G. J. & Cousins, R. D. Unified approach to the classical statistical analysis of small signals. *Phys. Rev. D* **57,** 3873–3889 (7 1998).
64. Confidence level computation for combining searches with small statistics. *NIM A* **434,** 435 –443. ISSN: 0168-9002 (1999).

Acknowledgements

Working on my Ph.D. thesis took a huge fraction of my time during my last three years. I have to thank lot of people who helped me, and lot of friends I had close during the road.

First of all, I would like to thank the Mu2e group, where I learned the meaning of working in a group and not only with the single group members: Franco Cervelli whose knowledge and experience guided me through those years, and for the patience he showed leading the role of being my advisor; Franco Spinella and Simone Donati for the help and suggestions they constantly gave to me; Stefano di Falco for the support during the last few months; Stefano Miscetti, Stefano Roberto Soleti and the rest of the Frascati group for the good time spent together and for all the milestones we achieved; Ivano Sarra for the help and the support we give constantly to each other. Pavel Murat is named for last only because he deserves a special thank: he taught me how much physics one can make, and enjoy it! We spent so much time together working on our projects, and I think that the amount of work we have made it is just impressive. I do consider Pasha like a second father, and I am proud to be his apprentice.

It was amazing to work with all the physicists of the Mu2e collaboration, but a particularly warm thank goes to Robert Kutschke, Dave Brown, Andrei Gaponenko and Doug Glenzinski. They helped me in many ways and I really hope that they can enjoy my results.

My being away from home during these years would have been much more difficult without the love of my parents and of my twin-sister.

In the these years of preparation I think that a huge number of people crossed my life; all they changed my mind and made me grow up. I am lucky for having special friends in my native town; Giacomo Citti, Gabriele Pelusio, Sonny Terranova, Luca Santangeli, Tommaso Franchi, Andrea di Giovanni, Sofia Martini, Maria Dilbert, Francesca de Ranieri and Clarissa Barsanti. I consider my self really close to each of them, and wherever I go, every time I look an open sky (or a basketball field, or a soccer field too!) I have a lovely thought to each of them.

Another thank goes to my friends living in Pisa who kept in contact with me during these long three years; First I would like to thank Leonardo Gigli and Lars Eric for the long time spent together not only running! I did appreciate it, and I

after theses years, I consider them as my brothers! I am sure that without them it would have been much harder. I also would like to thank Marco Mariti and Francesco Colangelo, my wonderful housemates! I really enjoyed the time spent together in “via Cagliari”; than I thank also all the other friends I met around the INFN of Pisa: Veronica Colonna, Gina Greco, Veronica Colonna, Sofia Sarperi, for the time they spent with me.

I also would like to thank two special “Johns”, Francesco Muia, Federico Fabiano and Mauro Pieroni, that, even if are far from Pisa, did not forget our friendship, and sometimes also found the strength to answer my call in the very early morning!

One special thank goes to “John the Carrarin”. We spent together lots of our time, and we shared lots of experiences.

But above all, it would not have been the same without Giusj: I do not really know how to thank her for the love, support and patience she showed to me. Since I met her, she has lighted my life with her smile.